

AD A 038878

FD
NW

EXPERIMENTAL AND ANALYTICAL STUDY OF
A STEAM VANE EXPANDER

Gerald F. Robertson

Technical Memorandum
File No. TM 77-65
February 1, 1977
Contract No. N00017-73-C-1418

Copy No. 11

DDC
RECEIVED
MAY 3 1977
C

The Pennsylvania State University
Institute for Science and Engineering
APPLIED RESEARCH LABORATORY
Post Office Box 30
State College, PA 16801

APPROVED FOR PUBLIC RELEASE
DISTRIBUTION UNLIMITED

NAVY DEPARTMENT

NAVAL SEA SYSTEMS COMMAND

AD No. []
DDC FILE COPY

REPORT DOCUMENTATION PAGE		READ INSTRUCTIONS BEFORE COMPLETING FORM
1. REPORT NUMBER TM 77-65 ✓	2. GOVT ACCESSION NO.	3. RECIPIENT'S CATALOG NUMBER
4. TITLE (and Subtitle) EXPERIMENTAL AND ANALYTICAL STUDY OF A STEAM VANE EXPANDER.	5. TYPE OF REPORT & PERIOD COVERED PhD Thesis, Mech. Eng. ✓ May 1977	6. PERFORMING ORG. REPORT NUMBER TM-77-65 ✓
7. AUTHOR(s) Gerald F. Robertson	8. CONTRACT OR GRANT NUMBER(s) N00017-73-C-1418	10. PROGRAM ELEMENT, PROJECT, TASK AREA & WORK UNIT NUMBERS 12139 P.
9. PERFORMING ORGANIZATION NAME AND ADDRESS The Pennsylvania State University Applied Research Laboratory P. O. Box 30, State College, PA 16801	11. CONTROLLING OFFICE NAME AND ADDRESS Naval Sea Systems Command Department of the Navy Washington, D. C. 20362	12. REPORT DATE February 1977
14. MONITORING AGENCY NAME & ADDRESS (if different from Controlling Office) DoD	13. NUMBER OF PAGES 138 pages & figures	15. SECURITY CLASS. (of this report) Unclassified, Unlimited
16. DISTRIBUTION STATEMENT (of this Report) Approved for public release, distribution unlimited, per NSSC (Naval Sea Systems Command) 4/4/77		
17. DISTRIBUTION STATEMENT (of the abstract entered in Block 20, if different from Report) DDIC MAY 3 1977 UNCLASSIFIED		
18. SUPPLEMENTARY NOTES		
19. KEY WORDS (Continue on reverse side if necessary and identify by block number) Rotary Vanes Heat Transfer Steam Expander Leakage Friction		
20. ABSTRACT (Continue on reverse side if necessary and identify by block number) An experimental and analytical study of a rotary vane steam expander was conducted to determine the effect of leakage, friction and heat transfer on the expander performance. A commercially available rotary vane air motor was modified to operate on steam utilizing little or no liquid lubricant. The indicated power output, shaft power output and frictional power loss of the vane expander were experimentally determined as a function of speed, inlet timing and supply steam conditions. The steam mass flow rate and		

391.001

UNCLASSIFIED

SECURITY CLASSIFICATION OF THIS PAGE(When Data Entered)

20. ABSTRACT (continued)

component temperatures were also measured. The data show that severe internal leakage and frictional energy dissipation were major causes of efficiency reductions.

An analytical model of the expander thermodynamics, friction, leakage and heat transfer was developed from fundamental principles. The model predicts the expander leakage flow rate, frictional power loss heat transfer rate and the effect of these losses on the power output and efficiency. The analytically and experimentally determined frictional power losses were in agreement. The component temperature profiles were predicted with maximum errors of 10% - 15%. The predicted leakage flow was approximately 16% below the experimentally determined value. Errors in the leakage flow predictions resulted in the predicted indicated power outputs being 20% - 40% below the experimental values. This was condiered reasonably good in light of the difficulty in identifying the steam leakage paths and component clearances.

ABSTRACT for

NTIS Write Section
GPO Encl. Section

UNANNOUNCED

JUSTIFICATION

BY

DISTRIBUTION/AVAILABILITY CODES

Dist. AVAIL. and/or SPECIAL

A

UNCLASSIFIED

SECURITY CLASSIFICATION OF THIS PAGE(When Data Entered)

ACKNOWLEDGMENTS

The author wishes to thank Professor Carl H. Wolgemuth for his encouragement and guidance throughout this program.

The assistance of Messrs. Stanley Gulbernat, Rex Jacobs, William Loessh and Doyle Walker in constructing the apparatus is also appreciated.

The author wishes to acknowledge the support of this investigation by the Applied Research Laboratory of The Pennsylvania State University under contract with the Naval Sea Systems Command.

TABLE OF CONTENTS

	<u>Page</u>
ACKNOWLEDGMENTS	ii
LIST OF TABLES	v
LIST OF FIGURES	vi
NOMENCLATURE	ix
I. INTRODUCTION	1
1.1 General Statement of the Problem	1
1.2 Previous Related Studies	2
1.3 Purpose	4
II. EXPERIMENTAL APPARATUS AND PROCEDURE	7
2.1 Description of Expander	7
2.2 Experimental Apparatus	14
2.3 Experimental Procedure	19
2.4 Error Analysis	21
2.4.1 Power Measurement	21
2.4.2 Mass Flow Rate Measurement	23
2.4.3 Control Volume Pressure Measurement	23
2.4.4 Steam Enthalpy Measurement	23
2.4.5 Temperature Measurement	24
III. ANALYTICAL CONSIDERATIONS	25
3.1 Thermodynamic Model	25
3.2 Friction Model	26
3.3 Leakage Model	32
3.4 Heat Transfer Model	35
3.4.1 One-Dimensional Model	35
3.4.2 Rotor, Three-Dimensional Model	36
3.4.3 Stator, Three-Dimensional Model	39
3.4.4 End Plate, Three-Dimensional Model	43
3.5 Numerical Procedure	45
3.5.1 Transient Analysis	46
3.5.2 Steady State Analysis	46

TABLE OF CONTENTS (CONTINUED)

	<u>Page</u>
IV. EXPERIMENTAL AND THEORETICAL RESULTS	47
4.1 Experimental Conditions	47
4.2 Experimental Results	47
4.2.1 Power	47
4.2.2 Mass Flow Rate	55
4.2.3 Adiabatic Expansion Efficiency	61
4.2.4 Temperature Measurement Results	64
4.2.5 Expander Heat Loss	70
4.3 Comparisons with Theoretical Results	77
4.3.1 Mass Flow Rate	77
4.3.2 Power Output	80
4.3.3 Temperature Profiles and Heat Transfer Coefficient	83
V. SUMMARY AND CONCLUSIONS	91
5.1 Summary	91
5.2 Conclusions	92
BIBLIOGRAPHY	95
APPENDIX A: EQUATIONS USED IN THERMODYNAMIC MODEL	97
APPENDIX B: DERIVATION OF EXPRESSIONS FOR TANGENTIAL AND NORMAL ACCELERATIONS	108
APPENDIX C: DERIVATION OF FINITE DIFFERENCE EXPRESSIONS	111
APPENDIX D: DERIVATION OF FRICTIONAL HEAT FLUX EQUATIONS	118

LIST OF TABLES

<u>Table</u>	<u>Page</u>
1. Estimated Errors in the Power Measurements	22
2. Expander Heat Loss Data	76
3. Definitions of Non-Dimensional Variables	99

LIST OF FIGURES

<u>Figure</u>	<u>Page</u>
1. Schematic of Test Expander	8
2. Photograph of Test Expander	9
3. Dimensionless Pressure Versus Dimensionless Volume, Ideal Expander (No Leakage, Heat Transfer, or Friction). .	11
4. Spring Force Variation	13
5. Schematic of Experimental Apparatus	15
6. Bendersky Thermocouple Mounting	20
7. Schematic Diagram of Vane Expander Model	27
8. Vane Free Body Diagram	29
9. Leakage Paths for a Single Control Volume	33
10. Stator Model	40
11. End Plate Model	44
12. Pressure Versus Volume for 150 psia Supply Pressure 22.5° Arc of Admission	48
13. Pressure Versus Volume for 150 psia Supply Pressure 45° Arc of Admission	49
14. Power Versus Speed for 150 psia Supply Pressure	51
15. Power Versus Speed for 115 psia Supply Pressure	52
16. Mechanical Efficiency Data 150 psia Supply Pressure . . .	54
17. Mechanical Efficiency Data 115 psia Supply Pressure . . .	56
18. Mass Flow Rate Data for 150 psia Supply Pressure 22.5° Arc of Admission	57

LIST OF FIGURES (CONTINUED)

<u>Figure</u>	<u>Page</u>
19. Mass Flow Rate Data for 150 psia Supply Pressure 45° Arc of Admission	58
20. Mass Flow Rate Data for 115 psia Supply Pressure 22.5° Arc of Admission	59
21. Mass Flow Rate Data for 115 psia Supply Pressure 45° Arc of Admission	60
22. Adiabatic Expansion Efficiency Data for 150 psia Supply Pressure	62
23. Adiabatic Expansion Efficiency Data for 115 psia Supply Pressure	65
24. Stator Temperature Profile Data for 150 psia Supply Pressure 22.5° Arc of Admission	66
25. Stator Temperature Profile Data for 150 psia Supply Pressure 45° Arc of Admission	67
26. Stator Temperature Profile Data for 115 psia Supply Pressure 22.5° Arc of Admission	68
27. Stator Temperature Profile Data for 115 psia Supply Pressure 45° Arc of Admission	69
28. End Plate Temperature Profile Data for 150 psia Supply Pressure 22.5° Arc of Admission	71
29. End Plate Temperature Profile Data for 150 psia Supply Pressure 45° Arc of Admission	72
30. End Plate Temperature Profile Data for 115 psia Supply Pressure 22.5° Arc of Admission	73
31. End Plate Temperature Profile Data for 115 psia Supply Pressure 45° Arc of Admission	74
32. Rotor Surface Temperature Data	75
33a. Leakage Flow Rate Versus Speed	79
33b. Horsepower Versus Speed	79
34. Frictional Power Loss Versus Speed	82

LIST OF FIGURES (CONTINUED)

<u>Figure</u>	<u>Page</u>
35. Experimental and Analytical Stator Temperature Profiles 22.5° Arc of Admission	84
36. Experimental and Analytical End Plate Temperature Profiles	85
37. Ratio of Rotor Surface Temperature to Steam Saturation Temperature Data	88
38. Schematic Diagram Showing Control Volume	98
39. Variation of Exhaust and Intake Area for Arc of Admission and Arc of Exhaust Greater than Arc	101
40. Variation of Intake Area for Arc of Admission Less than Arc	102
41. Schematic of Vane Slot and Pressure Balancing or Pressurization Port	104
42. Interior Finite Difference Node	112
43. Boundary Finite Difference Node	115

NOMENCLATURE

<u>Symbol</u>	<u>Definition</u>
A	Exposed area of a vane
$A_{CG/pn}$	Normal acceleration of a vane relative to the rotor
A_{CGt}	Tangential acceleration of a vane center of gravity
$A_{CORIOLIS}$	Coriolis acceleration of a vane
AEVN	Area of vane tip
A_{max}	Maximum area for inlet or exhaust flow
A_N	Normal acceleration of a vane
AP	Area of vane tip exposed to the inlet or exhaust port
A_{pn}	Normal acceleration of a point on a frame moving with the rotor at a radius corresponding with the vane center of gravity
A_{pt}	Tangential acceleration of a point on a frame moving with the rotor at a radius corresponding with the vane center of gravity
A_{rs}	Rotor surface area between adjacent vanes
ARC	Angle between adjacent vanes
ARCAD	Arc of admission
ARCEX	Arc of exhaust
A_t	Tangential acceleration of a vane
B	Breathing number
b	One-half the clearance between expander components
b'	Parameter in Keenan and Keyes equation of state for steam
c	Specific heat of tank wall

NOMENCLATURE (CONTINUED)

<u>Symbol</u>	<u>Definition</u>
C_D	Discharge coefficient
e	Eccentricity
F_E	End force on a vane
F_n	Normal force on a vane
F_{RB}	Rotor force on bottom side of a vane
F_{RT}	Rotor force on a vane at outside radius of rotor
F_t	Tangential force on a vane
F_3	Stator force on a vane
H	Height of tank
h	Specific enthalpy
\bar{h}	Mean convective heat transfer coefficient
Δh_t	Specific enthalpy change in nozzle
HR	Length of vane extension above rotor
k	Thermal conductivity
k_1	Thermal conductivity of body 1 of two bodies in sliding contact
k_2	Thermal conductivity of body 2 of two bodies in sliding contact
L	Characteristic length for determining convective heat transfer coefficients
L_E	Characteristic length for determining the end plate heat transfer coefficient
L_S	Characteristic length for determining the stator heat transfer coefficient
LV	Vane height
\dot{M}	Rate of change of mass in the control volume

NOMENCLATURE (CONTINUED)

<u>Symbol</u>	<u>Definition</u>
M_A	Moment about vane base
\dot{m}	Mass flow rate
\dot{m}_{IDEAL}	Expander ideal mass flow rate
\dot{m}_L	Expander leakage mass flow rate
\dot{m}_T	Expander total mass flow rate
m_{TB}	Mass of tank bottom
m_v	Vane mass
m_{wf}	Mass of water in tank at end of test
m_{wi}	Mass of water in tank at start of test
Δm	Increase in mass of water in tank during test
Δm_c	Mass of condensed steam
N	Rotor speed (revolutions per minute)
Nu_x	Local Nusselt Number
OP	Width of groove at base of vane slot
OPD	Depth of groove at base of vane slot
P	Pressure
P_A AEVN	Pressure force on vane base
P_f	Pressure force on side of a vane
P_{LAG}	Pressure in control volume lagging a vane
P_{LEAD}	Pressure in a control volume leading a vane
Pr	Prandtl number
P_s AP	Supply pressure force on a vane tip (=0 when vane not exposed to inlet)
ΔP	Pressure drop along a leakage path

NOMENCLATURE (CONTINUED)

<u>Symbol</u>	<u>Definition</u>
\dot{q}_1''	Frictional heat transfer rate per unit area into body 1 of two bodies in sliding contact
\dot{q}_2''	Frictional heat transfer rate per unit area into body 2 of two bodies in sliding contact
\dot{q}_{gen}''	Instantaneous heat generation rate per unit area
\bar{q}_{gen}''	Time averaged heat generation rate per unit area
\dot{q}_{TOTAL}''	Total frictional heat generation rate
\dot{Q}	Heat transfer rate
r	Radial coordinate
Δr	Incremental change in the radial coordinate
R	Resistance of a leakage path
R'	Ratio of rotor radius to stator radius
R_i	Rotor radius
R_{1-j}	Resistance of leakage path i-j
Re_x	Local Reynolds Number
Re_L	Reynolds Number at L
R_o	Stator radius
R_t	Tank radius
s	Laplace transform operator
SD	Depth of vane slot
SPF	Spring force on vane base
SW	Width of vane slot
T	Temperature
T_f	Temperature of tank bottom at end of test
T_1	Temperature of tank bottom at start of test

NOMENCLATURE (CONTINUED)

<u>Symbol</u>	<u>Definition</u>
\bar{T}	Laplace transform of temperature
T_{ROTOR}	Rotor surface temperature
T_{SAT}	Saturation temperature
T_V	Vane thickness
T_w	Expander component wall temperature
T_{WALL}	Tank wall temperature
$T_{\infty}(t)$	Instantaneous steam temperature
\bar{T}_{∞}	Time averaged steam temperature
t	Time
t'	Tank wall thickness
Δt	Incremental change in time
U_{CV}	Internal energy of the control volume
u_{wf}	Specific internal energy of the water in the tank at the end of a test
u_{wi}	Specific internal energy of the water in the tank at the start of a test
$V_{\text{CG/P}}$	Velocity of a vane center of gravity relative to a vane slot
V	Volume
v	Specific volume
V_H	Volume of pressurization ports
$V_{\text{MEAN/S}}$	Fluid velocity over the stator surface
$V_{\text{MEAN/E}}$	Fluid velocity over the end plate surface
V_{OP}	Volume of groove at base of vane
V_{SL}	Volume of vane slot, pressurization port, and groove at base of vane slot

NOMENCLATURE (CONTINUED)

<u>Symbol</u>	<u>Definition</u>
w	Width of a leakage path
W	Work
\dot{W}	Power
$\dot{W}_{\text{VISCIOUS}}$	Viscous power dissipation
W_n	Normal component of vane weight
W_t	Tangential component of vane weight
X	Coordinate along leakage path
x	Quality
x'	Length along tank wall
XAD	Angle inlet opens
XEX	Angle exhaust opens
XV	(LV-HR)
ΔX	Distance along a leakage path
z	Axial coordinate
Z'	Rotor length
Z_{PORT}	Width inlet and exhaust port
α	Thermal diffusivity
α_1	Thermal diffusivity of body 1 of two bodies in sliding contact
α_2	Thermal diffusivity of body 2 of two bodies in sliding contact
α'_{ROTOR}	Angular acceleration of the rotor
δ	Condensation liquid film thickness
ϵ	Clearance between rotor and end plate
$\eta_{\text{ADIABATIC EXPANSION}}$	Adiabatic expansion efficiency

NOMENCLATURE (CONTINUED)

<u>Symbol</u>	<u>Definition</u>
θ	Angular coordinate
$\Delta\theta$	Incremental change in the angular coordinate
μ	Viscosity
μ_1	Coefficient of friction between vane and end plate
μ_2	Coefficient of friction between vane and rotor
μ_3	Coefficient of friction between vane and stator
μ_1^{FE}	Frictional force between vane and end plate
μ_2^{FRB}	Frictional force between vane and rotor
μ_2^{FRT}	Frictional force between vane and rotor
$\mu_3^{F_3}$	Frictional force between vane and stator
ρ	Density
ρ_w	Liquid water density
ω	Angular velocity (Radians per unit time)
$\vec{\Omega}$	Angular velocity vector

Subscripts

f	Saturated liquid
g	Saturated vapor
fg	The change from saturated liquid to saturated vapor
o	Inlet condition
i-j	Leakage path from source i to sink j
k	Leakage source or sink

NOMENCLATURE (CONTINUED)

SuperscriptsDefinition

* Dimensionless variable

NOTE: A dot over a variable (\dot{P}) indicates either differentiation with respect to time, or a rate as in the case of \dot{m} (mass flow rate).

ABSTRACT

An experimental and analytical study of a rotary vane steam expander was conducted to determine the effect of leakage, friction and heat transfer on the expander performance. A commercially available rotary vane air motor was modified to operate on steam utilizing little or no liquid lubricant. The indicated power output, shaft power output and frictional power loss of the vane expander were experimentally determined as a function of speed, inlet timing and supply steam conditions. The steam mass flow rate and component temperatures were also measured. The data show that severe internal leakage and frictional energy dissipation were major causes of efficiency reductions.

An analytical model of the expander thermodynamics, friction, leakage and heat transfer was developed from fundamental principles. The model predicts the expander leakage flow rate, frictional power loss heat transfer rate and the effect of these losses on the power output and efficiency. The analytically and experimentally determined frictional power losses were in agreement. The component temperature profiles were predicted with maximum errors of 10% - 15%. The predicted leakage flow was approximately 16% below the experimentally determined value. Errors in the leakage flow predictions resulted in the predicted indicated power outputs being 20% - 40% below the experimental values. This was considered reasonably good in light of the difficulty in identifying the steam leakage paths and component clearances.

CHAPTER I

INTRODUCTION

1.1 General Statement of the Problem

Interest in Rankine cycle power systems for applications requiring power outputs in the 10-50 horsepower range, has led to the consideration of many devices for the system prime mover. Several positive displacement expanders such as the reciprocating, Wankel and rotary vane type have been suggested. Turbines also have been used extensively in Rankine cycle systems. However, the efficiency of turbines is diminished at the low power levels, particularly at part load, giving the positive displacement expanders a potential advantage in size and efficiency.

Rotary vane expanders do not vibrate as much as reciprocating expanders and due to their simplicity, they have possible weight advantages. Ideally, the rotary vane expander operates with a high efficiency. This has been analytically demonstrated for the idealized expander by Wolgemuch and Olson [1]. However, there exist in the vane expander losses due to leakage, friction and heat transfer which must be considered to realistically assess the suitability of the vane expander for use in low power dynamic thermal power systems.

Although vane expanders have been used extensively in industrial applications as low expansion air motors in the 1/4 to 10 horsepower range, the investigation and development of vane expanders for use in

high temperature vapor cycles has been limited. To determine the applicability of vane expanders in Rankine cycle applications and to improve their performance, it is necessary to understand the various losses which occur. Consequently, it is the object of this research to determine the effects of friction, leakage, and heat transfer on the performance of a rotary vane expander through a combined analytical and experimental program.

1.2 Previous Related Studies

Wolgemuth and Olson [1] developed a thermodynamic model of the rotary vane steam expander to study its general operating characteristics. The analysis included the transient charging and discharging processes of the expander to permit the breathing of these devices to be studied. Although the model contained provisions for the inclusion of heat transfer, and was adaptable to include the effects of leakage and friction, a detailed analysis of these phenomena and their effect on the expander performance was not performed. Their study shows that easy breathing in vane expanders is readily achieved and that a vane expander operating in the absence of heat transfer, leakage and friction can obtain a high expansion efficiency.

The frictional forces existing between the vanes and the stator of a rotary vane air cycle refrigeration machine (ROVAC) were analyzed by Edwards and McDonald [2]. The model utilized mean values of the geometric variables involved in the computation of the frictional forces. In order to determine the pressure forces on the vanes, the analysis used a thermodynamic model which did not have the capability to predict transient pressure effects.

Peterson and McGahan [3] developed a thermodynamic model of an oil flooded sliding vane air compressor. The model analyzed the frictional forces existing in the compressor and used a dynamic analysis of the working fluid to compute the pressure forces on the vanes. The model included the leakage occurring between the primary control volume (volume between adjacent vanes) and the control volumes leading it and lagging it as well as between the primary control volume and those regions at inlet pressure. In computing the leakage flow, an empirically determined discharge coefficient was employed to account for the blockage of the flow area by oil. The heat transfer was modeled by assuming the air transferred heat only with the oil in the chamber. Good agreement was obtained between the experimental and computed power input requirements and air flow rates.

Eckard [4] graphically presented experimental data taken from a high temperature vane expander being developed by General Electric. Eckard pointed out that leakage and friction are two major problem areas encountered in the development of a multi-vane vapor expander, with practical solutions to leakage problems the most difficult to obtain. In order to reduce leakage without large increases in friction, the General Electric expander depends on the maintenance of small clearances. Eckard noted, however, that considerable care must be taken to achieve and maintain small clearances under the changing temperature conditions encountered. Additional observations made by Eckard, based on the data collected are:

- 1) Moderate shift in expander speed does not severely reduce expander efficiency.
- 2) Breathing losses in a vane expander can essentially be eliminated since dynamic valves are not required.
- 3) Low speed operation (1200-1800 RPM) is currently essential for low frictional power losses.

Eckard concluded that additional material and design innovations are necessary to further improve the expander performance and to increase its applicability.

1.3 Purpose

The preceding discussion indicates that vane expanders have a potential for high efficiency in vapor cycle applications provided degradation of expander performance due to friction, heat transfer and leakage can be controlled.

Some experimental work has been done to develop an efficient rotary vane expander. Additionally, friction and to a lesser extent leakage, have been modeled in vane air compressors and in the Rovac machine utilizing techniques applicable to a vane expander. However, a physical description of the combined phenomena of heat transfer, leakage and friction that occur within a multi-vane vapor expander has not been formulated.

Since the amounts of leakage, heat transfer and a friction are not independent of one another, and since it is difficult, at times, to determine which of these phenomenon is associated with an observed degradation of power or efficiency, an understanding and description of

the physical processes occurring in the expander is required to identify the mechanisms of the various losses. Furthermore, the development of a working model of the vane expander would permit a degree of optimization of the expander design to be achieved prior to the construction of hardware.

In view of the high efficiency potential of vane expanders, and in view of the necessity to obtain a better understanding of the phenomena occurring within them, the following are the specific objectives of this thesis.

1. Analytical

The objective of the analytical study is to develop a working model of multi-vane expanders to permit the computation of the following, for various fluid conditions and expander geometry:

- a. Frictional power loss.
- b. Leakage flow rates and the associated effects on power output and efficiency.
- c. Heat transfer rates and their effects on power output and efficiency.
- d. Expander power and mass flow rate characteristics in the ideal case and under the influence of leakage, heat transfer and friction.

2. Experimental

The objectives of the experimental work are as follows:

- a. Measure the mass flow rate, and power characteristics of a multi-vane expander as a function of speed, and arc of admission to compare with the predicted values.

- b. Determine the frictional power loss as a function of speed, and arc of admission to obtain a better understanding of the friction in vane expanders and to test the validity of the friction analysis.
- c. Determine the overall leakage flow rate in order to verify the leakage analysis.
- d. Measure the rotor and stator temperatures for developing and verifying the heat transfer analysis and to determine the approximate amount of rotor and stator thermal expansion.

CHAPTER II

EXPERIMENTAL APPARATUS AND PROCEDURE

2.1 Description of Expander

The vane expander used to obtain the experimental data is schematically illustrated in Figure 1. The configuration of the expander was the result of extensive modification to a commercially available Gast Corporation model 8AM air motor. The expander primarily consisted of a cylindrical rotor, containing eight sliding vanes, eccentrically mounted in a cylindrical housing. Figure 2 is a photograph showing an exploded view of the expander. To permit the expander to operate with little or no liquid lubricant which might contaminate the working fluid, the vanes and end plates, shown in Figure 2, were constructed of Pure Carbon P5N and P9 carbon, respectively. To provide a hard rubbing surface for the vanes, the expander housing contained a heat treated 416 stainless-steel liner, located in the housing by two keys. The inlet and exhaust port timing was controlled by the location of the ports in the liner. The exhaust port was positioned so that exhaust began when the volume between adjacent vanes (the control volume) was a maximum. A 135° arc of exhaust was employed so that the control volume exhausted from its maximum volume to its minimum volume position. Ideally, this eliminated recompression losses.

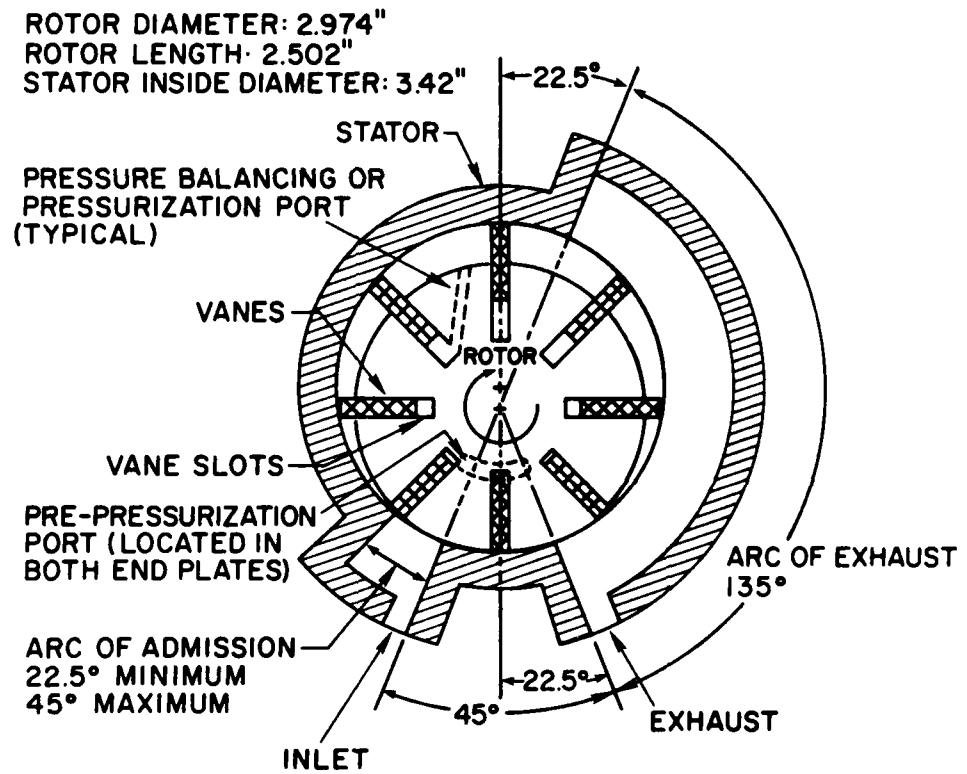


Figure 1. Schematic of Test Expander

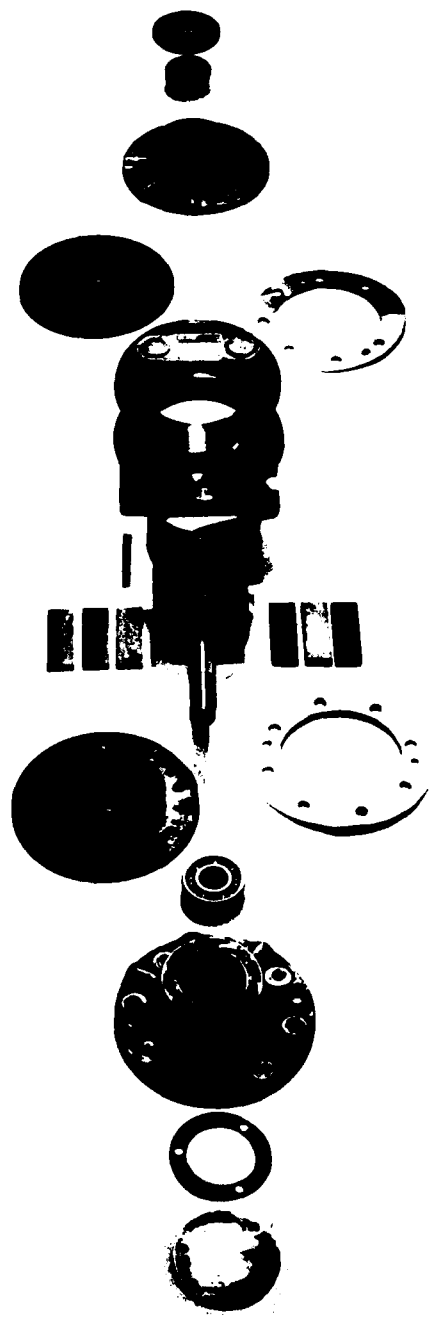


Figure 2. Photograph of Test Expander

Admission of the steam was initiated when the volume between adjacent vanes was a minimum (immediately after the exhaust port was closed). Two arcs of admission, 22.5° and 45° , were utilized in the test program. Initially, a 22.5° arc of admission was employed since it permitted a higher expansion ratio to be obtained than the 45° arc of admission. The expansion ratio is defined as the ratio of the volume at exhaust port opening to the volume at intake port closing. For a 22.5° arc of admission, Figure 3 shows that in the absence of friction, leakage, and heat transfer, the expansion of the working fluid from the supply pressure, of 150 psia, to the exhaust manifold pressure (atmospheric pressure) is practically complete prior to the exhaust port opening. Ideally, this results in a high adiabatic expansion efficiency. The adiabatic expansion efficiency is defined as the ratio of the work per pound of fluid to the isentropic enthalpy change from the inlet manifold conditions to the exhaust manifold pressure. In the ideal case, the 45° arc of admission results in an increase in the expander power output, as indicated by the increase in area under the P^* vs. V^* diagram shown in Figure 3. However, the increased arc of admission also results in a decrease in the expansion ratio and hence a decrease in adiabatic expansion efficiency.

To control leakage between the ends of the rotor and the end plates, shims were installed between the carbon end plates and the housing. The shims permitted the cold clearance between the rotor and end plate to be adjusted to obtain a balance between leakage and end plate-rotor friction.

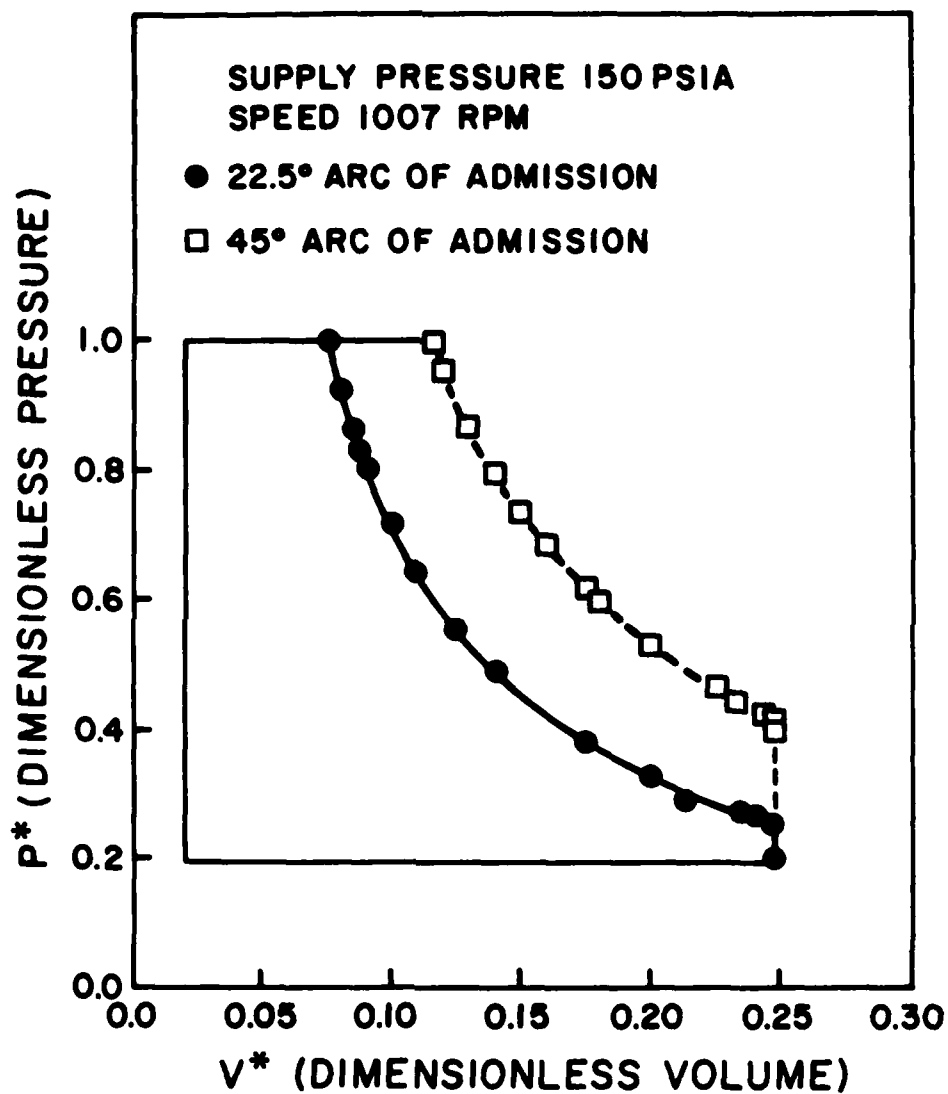


Figure 3. Dimensionless Pressure Versus Dimensionless Volume, Ideal Expander (No Leakage, Heat Transfer, or Friction)

Contact between the vanes and the stator was maintained by a combination of springs and steam pressure acting at the base of the vanes. Steam was ported to the base of the vanes by two 1/8 inch and one 3/16 inch diameter holes (pressure balancing ports or pressurization ports) which extended from the control volume leading a vane to the vane base, as shown schematically in Figure 1. The spring force on the vane base was maintained by a combination of push pins and leaf springs. The springs had a spring constant of approximately 729 lb_f/in. The variation in the force exerted by the spring on the vane is shown in Figure 4. A high spring force was maintained on the vane when the vane was near the inlet port. This was necessary to help prevent the high pressure steam from pushing the vane into the vane slot. Lower spring forces were exerted on the vane during portions of the closed expansion and the exhaust processes (where the steam pressures were lower) to reduce frictional energy dissipation. To develop a large pressure force on the vane base as it moved from the exhaust side to the inlet side of the expander, prepressurization ports were located in the end plates as shown in Figure 1. The ports permitted the flow of high pressure steam to the vane base while the vane tip was exposed to the low exhaust pressure. This method of obtaining a vane-stator seal resulted from testing the following sealing configurations:

- 1) Spring force only acting on the vane base (Spring constant of 17.1 lb_f/in. and 729 lb_f/in.). In both cases, the vane did not seal against the outer stator.
- 2) Steam pressure only, acting on the vane base utilizing pressure balancing ports. Pressurization of the vane base

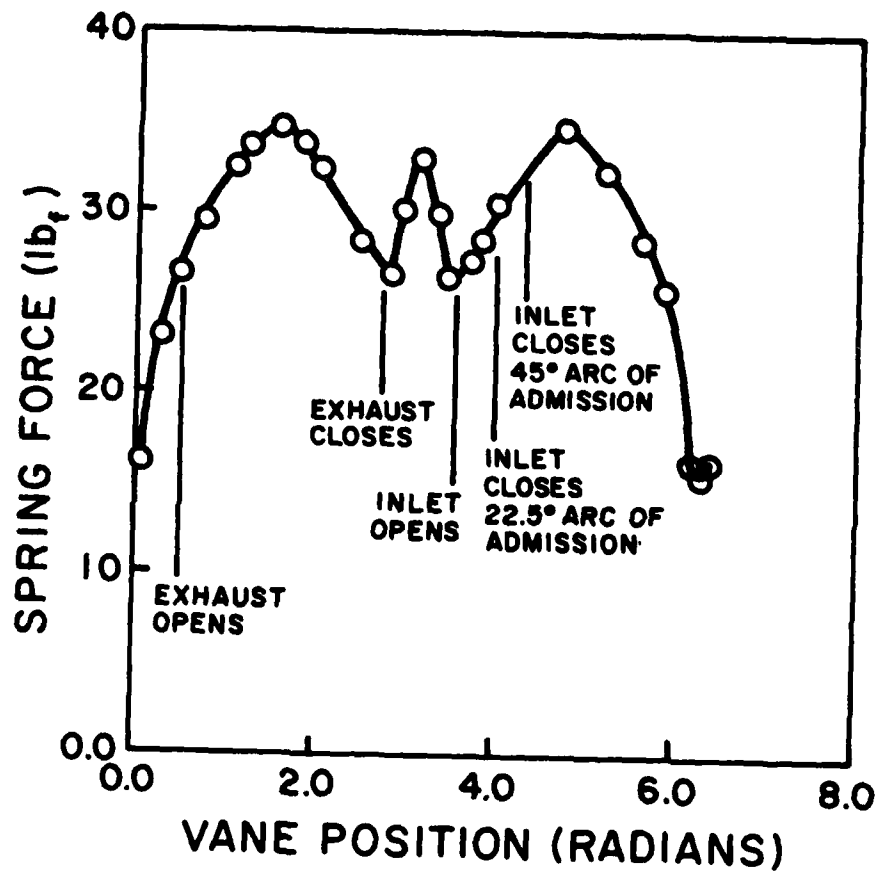


Figure 4. Spring Force Variation

- at the time of inlet opening was not rapid enough to prevent the vane from being pushed into the slot by high pressure supply steam. This resulted in severe leakage.
- 3) Steam pressure only acting on the vane base utilizing pressure balancing and prepressurization ports. The prepressurization ports were not effective in rapidly pressurizing the base of the vane. This also resulted in severe leakage since the vane was pushed into the slot by the high pressure steam.
 - 4) Combined spring force, with a spring constant of $729 \text{ lb}_f/\text{in.}$, and steam pressure utilizing pressure balancing and prepressurization ports acting on the vane base.

2.2 Experimental Apparatus

A schematic diagram of the apparatus used to test the expander is shown in Figure 5. The expander was coupled to a General-Electric D-C cradled dynamometer model number 5B284B1010, to obtain torque and power measurements. The dynamometer force-measuring device was a Toledo balance with a $0\text{-}30 \text{ lb}_m$ range in 0.01 lb_m subdivisions. The motor speed was measured with a General-Electric model An5531-1 tachometer generator coupled to a Standard Electric Time Company type-SG6 RPM counter and a clock.

A throttling valve in the steam supply line permitted the supply steam to be throttled from 250 psia to 150 psia or less before entering the expander. To ensure superheating of the supply steam, three Cole-Palmer flexible heating tapes, capable of delivering 2.88 kW at 230 volts were wrapped around the steam supply line. Control of the energy input into the heating tapes was obtained by use of a Variac.

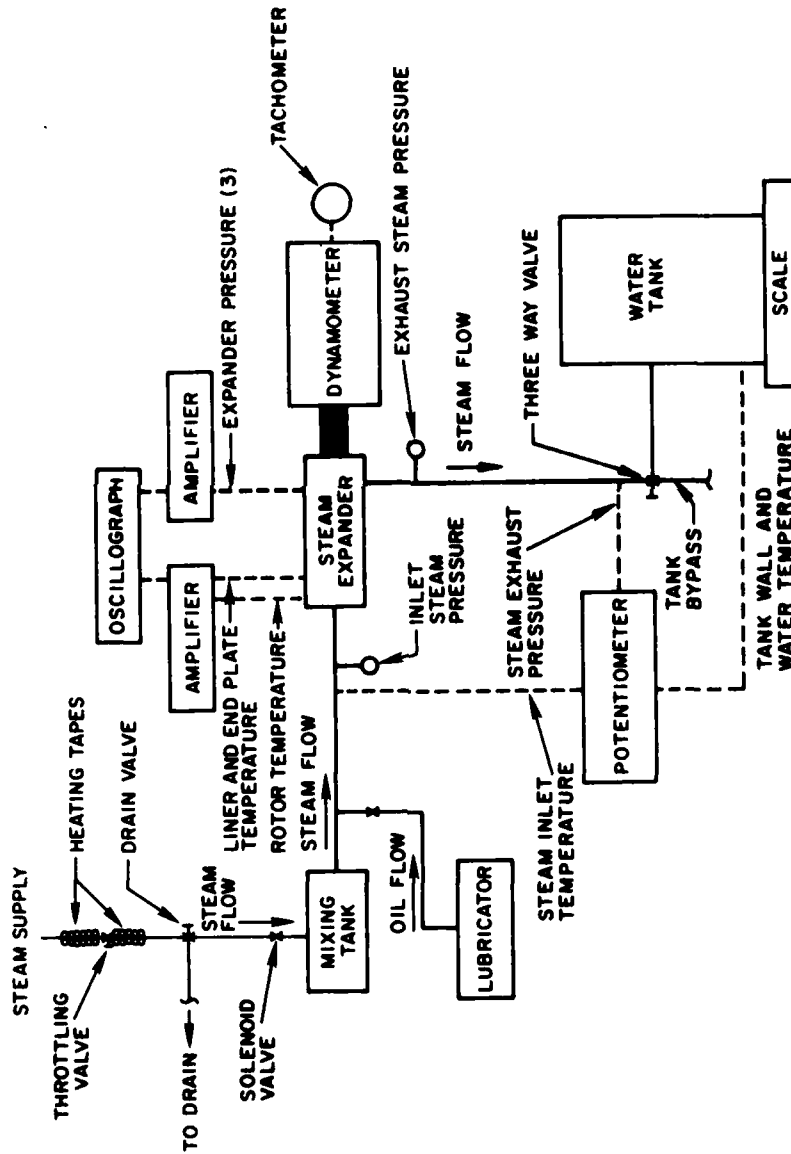


Figure 5. Schematic of Experimental Apparatus

Omega Engineering Company chromel-alumel thermocouples were mounted in the steam lines to measure the inlet and exhaust temperatures. A mixing tank was installed in the inlet line to eliminate radial temperature gradients in the flow prior to making the inlet temperature measurements. This permitted a better determination of the inlet mixing cup temperature. The inlet and exhaust temperatures were continuously recorded on a Leeds and Northrup Type H potentiometric recorder.

The expander inlet and exhaust pressures were measured by Ashcroft-Bourdon tube pressure gages, 0-200 psig and 0-100 psig, respectively.

The steam mass flow rate was measured by condensing the steam in a tank of water and measuring the increase in tank weight over a known time interval. The combined weight of the tank and the water was measured with a 0-1500 lb_m Toledo scale having 0.5 lb_m subdivisions. (The tare weight of the tank was measured with the tank empty so that the weight of the water could be obtained). A three way valve was installed between the expander outlet and the tank inlet so that the tank could be bypassed until the mass flow rate measurements were made.

Since the inlet steam was superheated, its state was determined from the pressure and temperature measurements. However, since the exhaust steam could be a two phase mixture, provisions were made for determining the enthalpy of the exhausting steam by making an energy balance on the condensing tank used to measure the mass flow rate. To do this, the tank was heavily insulated. The tank water temperature was measured using a thermistor (Yellow Springs Instrument Company No. 701) with a digital readout (United Systems Corporation Model 581C). The

system accuracy was $\pm 0.55^\circ\text{C}$. Additionally, chromel-alumel thermocouples were submerged in the water at different depths to provide a check on temperature gradients in the water. The tank wall temperature was measured with five (5) chromel-alumel thermocouples mounted at various vertical positions on the tank wall. The output of the thermocouples was measured with a Leeds and Northrup model 8686 potentiometer. Measurement of the steam flow into the tank, water temperature rise, and tank wall temperature rise permitted an energy balance to be performed on the tank. The enthalpy of the two phase exhausting steam could then be computed from the following expression:

$$h = \left[m_{TB} c(T_f - T_i) + 2\pi R_t \cdot t_w \cdot \rho c \left[\int_{x'=0}^{x'=H} T_{WALL}(x) dx \right]_{t+\Delta t} - \int_{x'=0}^{x'=H} T_{WALL}(x) dx \right]_{t} + m_{wf} u_f - m_{wi} u_i \Big/ \Delta m . \quad (2.1)$$

It was discovered during expander tests that leakage in the expander was sufficiently high so that the exhausting steam was superheated. Therefore, its state was determined by the exhaust temperature and pressure measurements.

Oil was pumped to the expander by a Mandel class XN force feed lubricator. The lubricator was driven by a variable speed motor. The oil flow rate was controlled by the speed of the motor and the stroke length of the pump metering plunger. The pump was capable of delivering oil flows of from $0 \text{ lb}_m/\text{min}$. to $0.13 \text{ lb}_m/\text{min}$. The oil employed was mixed using the raw materials and quantities given in Reference 5.

Measurement of the control volume pressure was accomplished with three piezoelectric pressure transducers mounted in one end plate. The positions of the transducers permitted measurement of the control volume pressure during filling of the volume, during expansion and during the initial phase of control volume blowdown. Two Kistler model 603 pressure transducers coupled to Kistler model 504 charge amplifiers were used. The third transducer was a Metrix model 5016 connected to a Metrix model 5080-3 charge amplifier. Provisions were made for simultaneously monitoring the charge amplifier outputs with a Tektronix model 5103N oscilloscope and a CEC (Consolidated Electrodynamics Corporation) model 5-124A oscillograph.

Since the pressure transducers were not designed to withstand the high temperature steam environment and since their output was temperature sensitive, the transducers were connected to water cooling adapters. The adapters permitted the output of the transducers to remain stable.

Seven (7) chromel-alumel thermocouples (0.005 inches in diameter) were mounted around the periphery of the stainless steel liner. The thermocouples were positioned 0.050 inches from the inside surface of the liner. The thermocouple leads were taken out of the expander housing through conax glands.

Chromel-alumel thermocouples were also installed at eleven circumferential positions in the carbon end plate. The thermocouples were mounted 0.065 inches from the inner face of the end plate. The liner and end plate thermocouples were connected through a switch and a CEC Type 1-165 amplifier to the oscillograph.

The surface temperature of the rotor was measured by an iron-Constantan, Bendersky [6] type thermocouple having a response time of 1 microsecond. The thermocouple is shown mounted in Figure 6. The signal from the thermocouple was transferred from the rotor through a mercury slip ring (Meridian Laboratory Incorporated, Mercotac I). The signal was amplified by a CEC Type 1-165 high-gain amplifier and recorded on the oscillograph. The Mercury slip ring was capable of operating at a maximum temperature of 150°F. To ensure that the slip ring temperature did not exceed this value, a cooling adapter cooled an extension of the rotor shaft, ahead of the slip ring. This permitted the slip ring to operate at room temperature.

2.3 Experimental Procedure

Prior to operating the expander, the steam line was heated by the heating tapes. The steam flow was diverted, ahead of the expander, to a drain line to remove any liquid condensate in the steam line (see Figure 5). Once the condensate was removed, the solenoid valve upstream of the expander was opened, causing the expander to rotate, and the drain valve was closed. The force feed lubricator was started, and cooling water flow to the pressure transducer and slip ring cooling adapters was initiated. The supply pressure was adjusted to the desired value, utilizing the throttling valve. The dynamometer load was adjusted until the expander was rotating at the desired speed. The steam exhausting from the expander bypassed the condensing tank via a three way valve.

The expander was operated in this manner until the inlet steam temperature and the expander component temperatures reached steady state

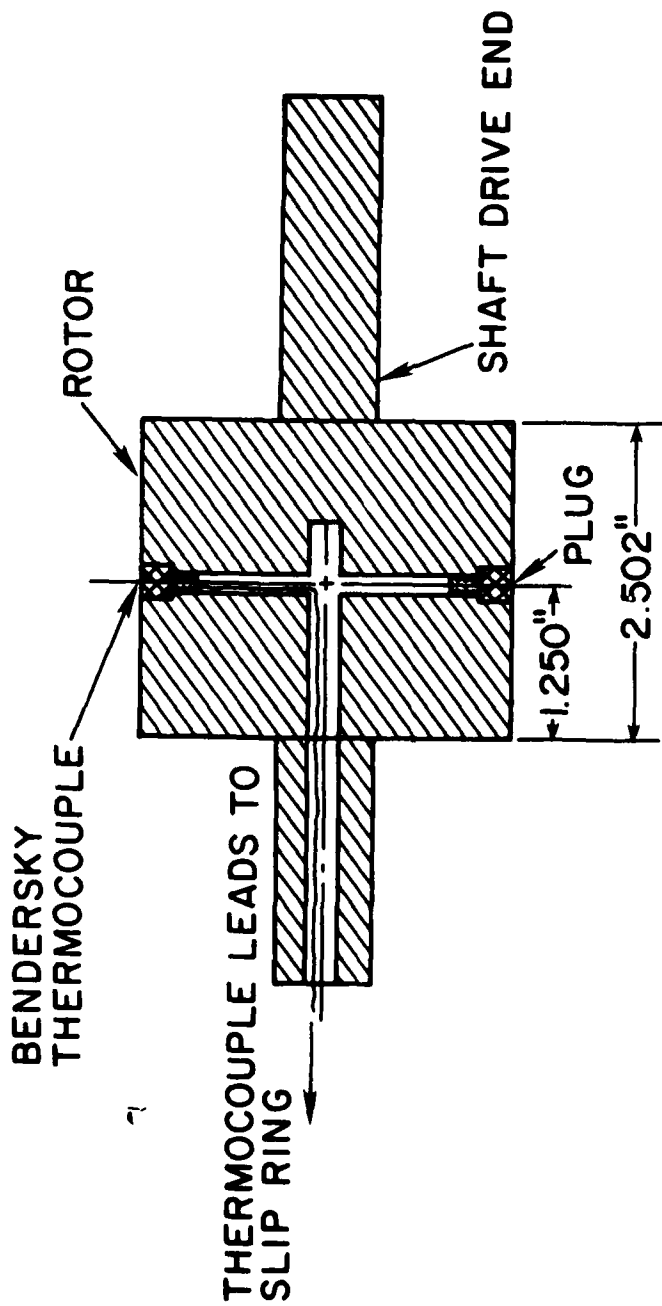


Figure 6. Bendersky Thermocouple Mounting

values. The expander was then shut down by closing the solenoid and the throttling valves. The force feed lubricator was also stopped. The initial mass of water in the condensing tank was recorded and the pressure transducer outputs grounded. The solenoid valve was opened and the throttling valve adjusted to provide the correct supply pressure. The force feed lubricator was started and the revolution counter and clock were activated. The expander exhaust steam was collected in the condensing tank. The thermocouple and pressure transducer outputs were recorded along with the supply and exhaust pressures. The dynamometer load was also recorded. After approximately three to five minutes of operation, the revolution counter and clock were stopped, the condensing tank was bypassed, the force feed lubricator was stopped and the solenoid and throttling valves were closed. The final mass of water in the condensing tank was recorded along with the number of revolutions and the operating time. Water flow to the cooling adapters was continued until the next test or until the expander components had cooled to room temperature.

2.4 Error Analysis

The errors associated with the various measurements have been estimated by considering the parameters which affect the absolute accuracy of the measurements.

2.4.1 Power Measurement. Errors in the power measurements resulted from an uncertainty in the length of the torque arm, the motor speed and the torque arm loading. The estimated errors associated with the power measurements are tabulated in Table 1.

TABLE 1

Estimated Errors in the Power Measurements

PARAMETER	ESTIMATED ERROR IN THE PARAMETER	RESULTING ERROR IN THE POWER (hp)
Dynamometer Torque Arm Length	± 0.062 inches	3.40×10^{-3}
Motor Speed	± 5 RPM	5.08×10^{-3}
Torque Arm Loading	± 0.1 lb _m	2.82×10^{-3}

An overall estimate of the error in the power measurement was made by taking the square root of the sum of the squares of the errors given in Table 1. The resulting estimated error is approximately ± 0.01 hp.

2.4.2 Mass Flow Rate Measurement. Calibration of the Toledo scale showed it to be accurate to within 0.5 lb_m . An error of 0.5 lb_m in measuring the mass of water in the tank resulted in an error in the mass flow rate measurement of approximately $\pm 0.1 \text{ lb}_m/\text{min}$.

2.4.3 Control Volume Pressure Measurement. An estimate of the error in the control volume pressure measurement is quite difficult. The output of the piezoelectric transducers is affected by transducer temperature and decay of the output signal. The control volume pressure, measured by the pressure transducers during the portion of the cycle when the inlet was open, was compared to the supply pressure gage measurements. General agreement was within ± 4 psia. Similarly, agreement between overlapping pressure transducers which simultaneously measured the same control volume pressures during certain portions of the cycle was within approximately ± 4 psia. Hence, a rough estimate of the error associated with the pressure measurement is ± 4 psia.

2.4.4 Steam Enthalpy Measurement. The errors associated with the measurement of the expander inlet and exhaust steam enthalpy result from errors in the steam temperature and pressure measurements. Errors also result from stratification of the flow. A mixing tank was installed in the inlet steam line to minimize flow stratification. The superheated exhaust steam was mixed during the control volume blowdown process. The exhaust temperature and pressure measurements were made adjacent to the

expander exhaust port so that stratification of the flow in the steam line would have a very short time to occur.

Errors in the pressure measurement of ± 2 psia and in the temperature measurement of $\pm 4^\circ\text{F}$ result in errors in the steam enthalpy of ± 3.19 BTU/lb_m. This is approximately a $\pm 0.3\%$ error. Therefore, in view of the precautions taken to eliminate flow stratification, an error of $\pm 1\%$ in the enthalpy measurement can be expected with reasonable confidence.

2.4.5 Temperature Measurement. The manufacturer specified deviation of the chromel-alumel thermocouples, output-vs-temperature characteristics from the standard table values is $\pm 4^\circ\text{F}$. This was verified through experimental tests.

Calibration tests of the iron-Constantan, Bendersky thermocouple showed the deviation of its output-vs-temperature characteristics, from the standard table values to be $\pm 4^\circ\text{F}$.

Precautions were taken to reduce thermocouple installation errors. Particular care was taken to minimize the change in the rotor heat transfer characteristics caused by the installation of the Bendersky surface thermocouple. An iron-Constantan thermocouple was employed. The thermocouple had an iron body so that it had thermal properties similar to those of the iron rotor. Thin thermocouple wires were used to minimize lead losses. The thermocouple was mounted so that the pattern of the steam flow over the surface was disturbed as little as possible by the thermocouple.

It is believed that the precautions taken in mounting the Bendersky thermocouple reduced the thermocouple installation errors.

CHAPTER III

ANALYTICAL CONSIDERATIONS

3.1 Thermodynamic Model

The foundation of the vane expander analysis is the thermodynamic model described by Wolgemuth and Olson [1]. The thermodynamic analysis utilized the principles of conservation of energy and mass, as applied to the volume between adjacent vanes (the control volume), in combination with the geometric expressions for the volume, and the equation of state in the form of steam tables. These relationships were used to obtain differential equations for pressure, mass, volume and in the superheated region, temperature of the working fluid as a function of rotor position. The differential equations, in conjunction with the expression for the indicated power output of the control volume, $\dot{\omega} = \dot{P}\dot{V}$, were solved numerically using Hamming's Predictor Corrector method [7].

In formulating the thermodynamic model, the first law of thermodynamics was employed in the form

$$\dot{Q} - \dot{W} + (\dot{m}h)_{in} - (\dot{m}h)_{out} = \dot{U}_{cv} \quad (3.1)$$

Therefore, the model is capable of predicting the power output of the expander in the ideal case, where mass transfer occurs only through the inlet and the exhaust ports, and the control volume is adiabatic. However, the thermodynamic model can also determine the effects of heat

transfer on the expander performance by computing the heat transfer rates in separate heat transfer models and inputting the rates into the thermodynamic model as \dot{Q} . Similarly, the effect of leakage can be determined by computing the leakage flow in a separate leakage model and inputting the leakage flow rates into the thermodynamic model as \dot{m}_{in} or \dot{m}_{out} . Hence, in the case of leakage, \dot{m}_{in} or \dot{m}_{out} includes flow through the inlet and exhaust ports as well as leakage.

The work term in Equation (3.1) is the indicated work of the expander or the PdV work done by the working fluid. The effect of friction on the shaft power can be determined by computing the frictional work loss by a separate friction model and subtracting it from the indicated work.

To analytically determine the characteristics of the expander in the presence of leakage, friction, and heat transfer, separate models for these phenomena were developed which interact with the thermodynamic model as described earlier and as schematically illustrated in Figure 7.

3.2 Friction Model

The analysis of the expander power loss due to friction assumes that there is contact and hence, friction between the vanes and the following components:

- a. Stator
- b. Rotor
- c. End Plates.

There may also be friction between the rotor and the end plates when rotor-end plate contact occurs. It was assumed that there was no rotor-end plate contact in the experimental expander. This assumption

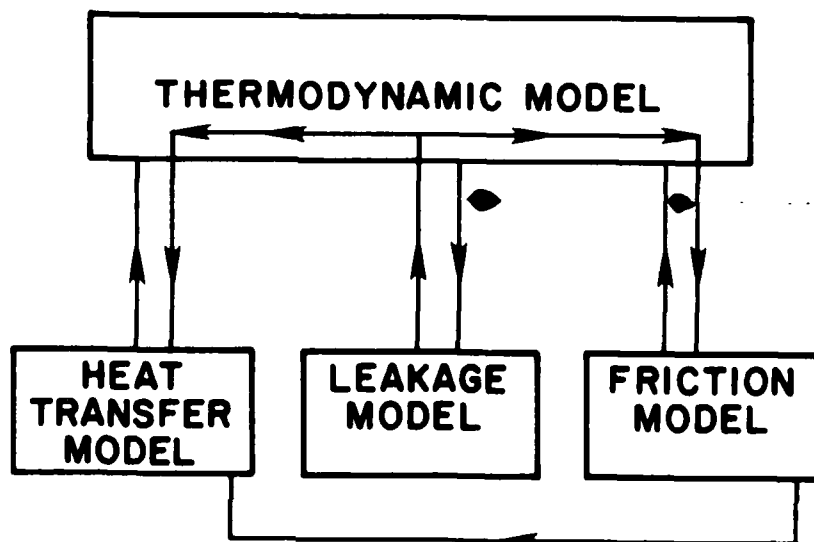


Figure 7. Schematic Diagram of Vane Expander Model

was based on the observed freedom of rotor motion while the expander was both hot and cold. Thus, it was not included in the analysis. However, since a small amount of liquid lubricant was employed, an analysis similar to that described in Reference 8 was used to determine the power loss resulting from the viscous forces acting on the ends of the rotor. By neglecting centrifugal effects and assuming the flow to be steady, laminar and incompressible, the following expression for the power loss due to these viscous forces was obtained:

$$W_{\text{VISCIOUS}} = \frac{\mu \omega^2 \pi R_1^4}{\epsilon} + \frac{2\omega \epsilon R_1^3}{3} \frac{dP}{dX} \quad (3.2)$$

Reference 9 states that the pressure drop term in Equation (3.2) is usually negligible since the leakage is often normal to the velocity in the regions where viscous dissipation occurs. Therefore, that term was neglected.

In order to determine the frictional forces on a vane, free body diagrams like that shown in Figure 8 were employed.

The forces that are the source of the frictional energy dissipation are F_{RB} , F_{RT} , F_3 , and F_E . Prior to determining the magnitude of these forces, it was necessary to determine the pressure forces and the normal and tangential accelerations.

The normal and tangential accelerations of the vanes may be computed from the expander geometry under the assumption that the vane tip is in contact with the stator at all times. The expressions used in computing the accelerations are given in Appendix B.

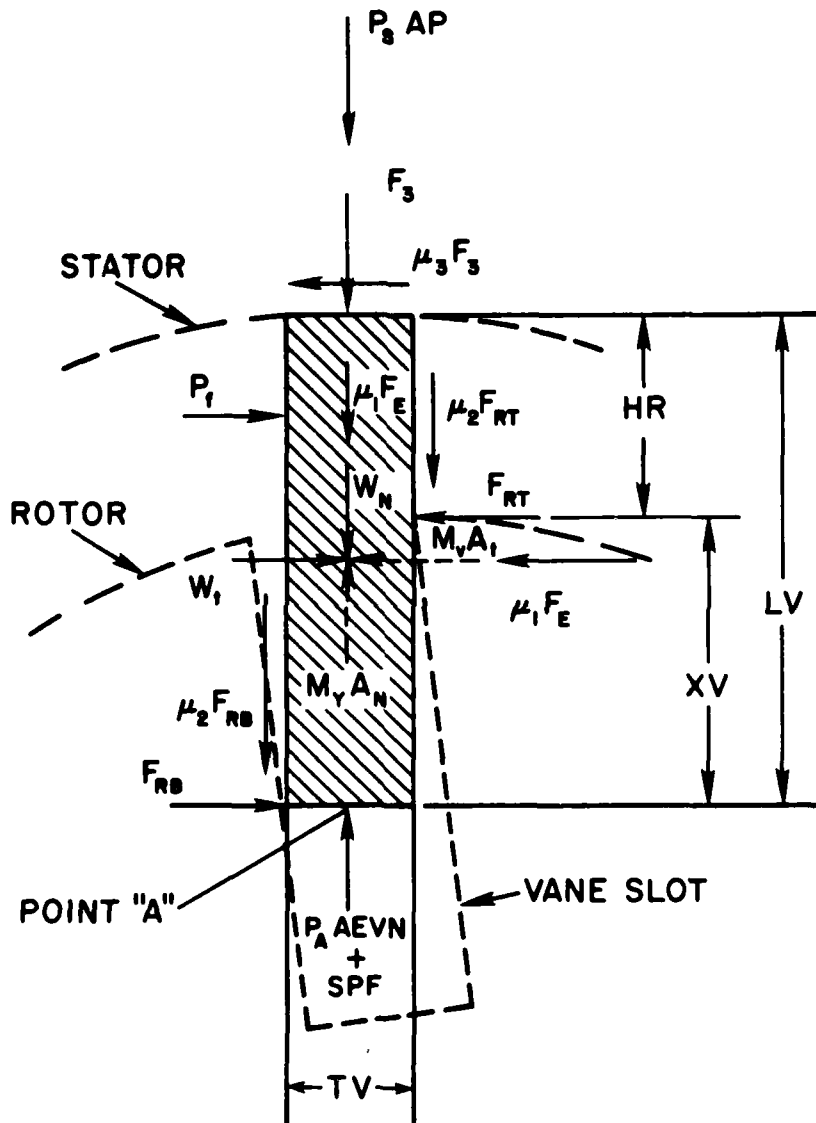


Figure 8. Vane Free Body Diagram

The net pressure force on the side of the vane, P_f , is computed as follows:

$$P_f = (P_{LAG} - P_{LEAD}) A \quad (3.3)$$

where P_{LAG} and P_{LEAD} are the pressures in the control volumes lagging and leading the vane and A is the exposed area of the vane. The pressures used are those predicted by the thermodynamic model in the presence of leakage but in the absence of friction. Due to the small vane-rotor clearance in a cold expander, it was assumed that P_f acts only on the vane in the space between the rotor and the stator and no other pressure forces act on the side of the vane. In computing the force at the base of the vane, it was assumed that the pressure under the vane was the same as that in the leading control volume due to the existence of the pressure balancing ports. The spring force exerted on the vane is equal to the product of the spring constant and the spring deflection.

Due to its larger coefficient of thermal expansion, the rotor was assumed to be longer than the vanes. Therefore, the force exerted on the vanes by the end plates was computed by assuming that the vane was pushed against one end plate by the pressure in the control volume. The end force on the vane was then equal to the product of the control volume pressure and the area of the vane end.

Since the mass of the vanes is known, and since the friction coefficient may be estimated, the only unknowns are F_{RT} , F_{RB} and F_3 . These are found by applying the three equations of dynamic equilibrium

$$\Sigma F_{\text{NORMAL}} = M \frac{A}{V N} , \quad (3.4)$$

$$\Sigma F_{\text{TANGENTIAL}} = M \frac{A}{V t} , \quad \text{and} \quad (3.5)$$

$$\Sigma M_A = 0 , \quad (3.6)$$

to the free body diagrams of the vane.

During one-half of the rotor revolution, the vane is pushed inward (toward the center of the rotor) by the stator. During the other half, the vane is pushed outward by the pressure and spring forces at its base. Hence, at the end of one-half revolution, there is a reversal of the direction of the friction forces between the vane and rotor. Additionally, the net pressure force on the side of the vane may not always act in the direction of rotation as shown in Figure 8. Therefore, four free body diagrams have been used, resulting in four sets of equations. As an example, the equations for Figure 8 in matrix form are

$$\begin{vmatrix} -1 & -\mu_2 & -\mu_2 \\ -\mu_3 & 1 & -1 \\ -LV\mu_3 & -\frac{TV}{2}\mu_2 & \frac{TV}{2}\mu_2 - XV \end{vmatrix} X \begin{vmatrix} F_3 \\ F_{RB} \\ F_{RT} \end{vmatrix} = \begin{vmatrix} -P_A A E V N - S P F + \mu_1 F_E - M \frac{A}{V N} + W_N + P_s A P \\ -P_f + \mu_1 F_E - W_t + M \frac{A}{V t} \\ -W_t \left(\frac{LV}{2}\right) + \mu_1 F_E \left(\frac{LV}{2}\right) - P_f \left(LV - \frac{HR}{2}\right) + M \frac{A}{V t} \left(\frac{LV}{2}\right) \end{vmatrix} . \quad (3.7)$$

The remaining equations are similar and will not be presented.

The solution of the equations for F_3 , F_{RB} and F_{RT} is accomplished by using the method of Gaussian elimination.

The values of F_3 , F_{RB} , F_{RT} , and F_E and hence, the corresponding friction forces were determined as a function of θ as the rotor rotated in small increments $\Delta\theta$. The incremental frictional work loss was computed as the product of the frictional force times the radial or tangential distance the vane traveled during the increment of rotation. The sum of the incremental work losses over 360° is the total frictional work loss per revolution due to vane friction. The instantaneous frictional power loss was computed at each vane position as the product of the frictional force at the position and the velocity.

The power loss due to friction between the vanes and rotor, stator, and end plate is equal to the product of the number of vanes, the frictional work loss per revolution per vane and the speed. The net frictional power loss is the sum of the power loss due to the vane friction and the power loss due to viscous drag on the rotor ends.

It was assumed that all the energy dissipated by friction is converted to heat which is transferred into either the rotor, lubricating oil, stator, vane or end plate. A further discussion of the frictional heat generation will be given in the description of the heat transfer model.

3.3 Leakage Model

The leakage flow paths, assumed for this analysis, are shown for a single control volume in Figure 9.

It was assumed that the leakage flow would be quasi-steady and, due to the small clearances maintained in a vane expander, laminar. Considerable simplification was made by treating the steam as an incompressible fluid. The relationship for parallel flow between flat

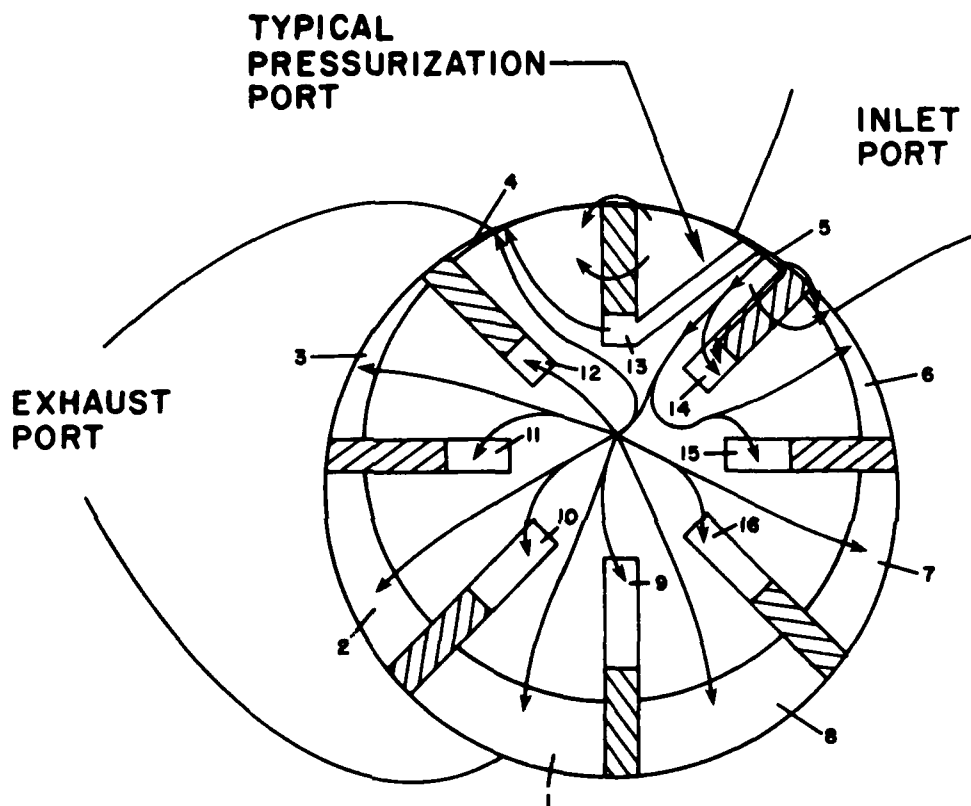


Figure 9. Leakage Paths for a Single Control Volume

plates was employed to obtain the following expression for the leakage flow along each path:

$$\begin{aligned} \dot{m}_L &= \frac{\rho}{\mu} \frac{2(P_1 - P_2)b^3w}{3\Delta X} \\ &= \frac{\rho\Delta P}{R} \quad \text{where } R = \frac{3\Delta X\mu}{2b^3w} \end{aligned} \quad (3.8)$$

The lengths of the leakage paths, ΔX in Equation (3.8) were taken as the straight line distance from the source to the sink along the leakage path. The widths of the leakage paths (w) were determined by apportioning the total width of a leakage path at the source over the total number of sinks the source leaked to along the leakage path. It should be noted that Equation (3.8) neglects relative motion between the moving and stationary parts.

Equation (3.8) was applied to all the leakage paths originating from each control volume. As an example, for control volume 5 (see Figure 9), the expression for the net leakage flow out is

$$\begin{aligned} \dot{m}_{L5} &= P_5 \left[(P_5 - P_4) \left(\sum \frac{1}{R_{5-4}} \right) + (P_5 - P_{14}) \left(\sum \frac{1}{R_{5-14}} \right) + (P_5 - P_3) \frac{1}{R_{5-3}} \right. \\ &+ (P_5 - P_2) \frac{1}{R_{5-2}} + (P_5 - P_1) \frac{1}{R_{5-1}} + (P_5 - P_8) \frac{1}{R_{5-8}} + (P_5 - P_7) \frac{1}{R_{5-7}} \\ &+ (P_5 - P_6) \left(\sum \frac{1}{R_{5-6}} \right) + (P_5 - P_{12}) \frac{1}{R_{5-12}} + (P_5 - P_{11}) \frac{1}{R_{5-11}} \\ &+ (P_5 - P_{10}) \frac{1}{R_{5-10}} + (P_5 - P_9) \frac{1}{R_{5-9}} + (P_5 - P_{16}) \frac{1}{R_{5-16}} + (P_5 - P_{15}) \\ &\left. \frac{1}{R_{5-15}} \right], \end{aligned} \quad (3.9)$$

where R_{i-j} denotes the resistance of each leakage path and P_k denotes the pressure of the leakage source or sink. The leakage flow is computed for discrete rotor positions. A curve is then fit to the computed flow rates to obtain the leakage as a continuous function of rotor position.

The pressures in Equation (3.9) were obtained as a function of rotor position from the thermodynamic model. However, the pressure of a control volume is dependent on the leakage flow rate. Hence, it was necessary to iterate to obtain an accurate measure of the flow. This was accomplished by initially inserting the control volume pressures, computed in the absence of leakage, into the leakage expressions. The leakage flow rate was computed and then input into the thermodynamic model to recompute the control volume pressures. Based on these new pressures, the leakage flow was recomputed. This process was repeated until the control volume pressures varied only slightly from iteration to iteration.

3.4 Heat Transfer Model

3.4.1 One-Dimensional Model. A one-dimensional analysis of the heat transfer between the working fluid and the stator as well as between the working fluid and the end plates was performed to obtain an estimation of the effect of heat transfer on the expander performance. The fluid motion over the stator and end plates was modeled as flow over a flat plate, and standard flat plate relationships were used to compute the convective heat transfer coefficients. The electrical analogy to heat transfer was employed and the heat transfer rate was obtained as a function of the various thermal resistances (component material, boundary layer, etc.) and the temperature difference between the working fluid and

the surroundings. The working fluid temperature was obtained directly from the thermodynamic model.

The simplified heat transfer analysis, while permitting a gross determination of the heat transfer rates and their effect on the expander performance relative to leakage and friction, does not permit an accurate determination of the temperature profiles in the stator, rotor or end plates (necessary for computations of thermal expansion). Furthermore, the assumption of one-dimensional heat transfer allows only approximate values of the heat transfer rates to be obtained.

To obtain a better representation of the heat transfer in the expander, more sophisticated models of the rotor, stator and end plates were required. The approach taken in modeling these components will be discussed separately.

3.4.2 Rotor, Three-Dimensional Model. A finite difference approach was used to approximate the heat conduction equation

$$\frac{1}{\alpha} \frac{\partial T}{\partial t} = \frac{\partial^2 T}{\partial r^2} + \frac{1}{r} \frac{\partial T}{\partial r} + \frac{1}{r^2} \frac{\partial^2 T}{\partial \theta^2} + \frac{\partial^2 T}{\partial z^2} \quad (3.10)$$

in the expander rotor. Appendix C illustrates the method used in forming the finite difference equations.

Since the flow pattern in the control volume is not known, it is difficult to determine the heat transfer coefficient between the steam and the rotor. Therefore, an experimentally measured surface temperature was specified as the boundary condition on the rotor surface. It was assumed that for a given control volume, the rotor surface temperature did not vary in the axial or tangential direction. This was an

approximation since frictional heat generation between the vane and rotor would cause a higher surface temperature to be observed near the vane slots.

Due to friction, heat is generated at the vane rotor interface. Therefore, the boundary condition along the slot walls at points in contact with a vane was a specified heat flux. The total amount of heat generated was determined by the friction model described earlier. A fraction of the heat generated is transferred into the rotor and the remainder is transferred into the vane. To obtain an approximation of the fractions of the heat generated going into the vane and rotor, an exact solution to the temperature profiles in two semi-infinite solids in frictional contact was obtained. The temperatures, at the surface of contact, for the solids were equated resulting in the following expressions for the amount of heat transferred into each solid (see Appendix D):

$$\dot{q}_1'' = \left[\frac{\dot{q}_{\text{TOTAL}}''}{1 + \frac{k_1}{k_2} \sqrt{\frac{\alpha_2}{\alpha_1}}} \right] \frac{k_1}{k_2} \sqrt{\frac{\alpha_2}{\alpha_1}} \quad \text{and}$$

$$\dot{q}_2'' = \frac{\dot{q}_{\text{TOTAL}}''}{1 + \frac{k_1}{k_2} \sqrt{\frac{\alpha_2}{\alpha_1}}} \quad (3.11)$$

An adiabatic boundary condition was assumed for that portion of the vane slot not in contact with a vane.

The rotor is symmetric in the axial direction. Therefore, only one-half of the axial length of the rotor was used in the analysis. The rotor had an adiabatic boundary condition at the plane of symmetry.

The rotor model included provisions for using a specified heat flux, resulting from friction, as the boundary condition for the rotor end facing the end plate. However, based on the freedom of rotor motion in the experimental expander, it was assumed that there was no rotor-end plate contact and hence, no resulting frictional energy dissipation. It was also assumed that the viscous energy dissipation between the oil and rotor only resulted in the increase in the temperature of the oil.

Lack of end plate-rotor contact eliminated a major source of heat generation. With this source of heat generation eliminated, the rotor end effects were neglected and the heat conduction equation solved for two dimensions. Analysis of the computed rotor temperature profile revealed that due to the rapid small amplitude fluctuations of the rotor surface temperature, the changing surface conditions did not greatly effect the rotor temperature at points well below the surface. Therefore, to permit the use of several nodes near the surface without excessively increasing the computation time, modifications to the analysis were made.

The mean rotor surface temperature was computed and that temperature used as a boundary condition at a depth of 0.050 inches below the surface. Utilizing this boundary condition permitted considering only that portion of the rotor contained between two vane slots. The boundary condition at the vane slot and the rotor ends were not changed. The heat transfer to the rotor was computed using the temperature gradient near the surface. Since the rotor surface temperature did not vary greatly, the mean rotor surface temperature was sufficiently good for use in computing the rotor thermal expansion.

3.4.3 Stator, Three-Dimensional Model. To obtain the temperature profiles and heat transfer rates, a three-dimensional analysis of the stator was required due to the location of the inlet and exhaust ports at the axial center of the stator. The ports act as heat sources or sinks causing temperature gradients to exist between the ports and the ends of the stator. The three-dimensional steady state heat conduction equation

$$\frac{\partial^2 T}{\partial r^2} + \frac{1}{r} \frac{\partial T}{\partial r} + \frac{1}{r^2} \frac{\partial^2 T}{\partial \theta^2} + \frac{\partial^2 T}{\partial z^2} = 0 \quad (3.12)$$

was transformed into finite difference form for the stator geometry, as shown in Figures 10. The method of forming the finite difference expressions is illustrated in Appendix C.

At the inside surface, heat is transferred to the stator by convection. Additionally, heat is generated at the inside surface due to friction between the vanes and the stator. Therefore, the inside surface boundary condition was

$$-k \frac{\partial T}{\partial r} = \bar{h}(\Gamma_{\infty} - T_w) + \dot{q}_{\text{gen}}'' \quad (3.13)$$

The fluid temperature, T_{∞} and heat generation rate seen by a particular position on the stator surface are actually functions of time. However, to permit a steady state analysis, the time averaged wall temperature and heat generation rates were employed. For a given position on the stator surface, the surface temperature was computed as:

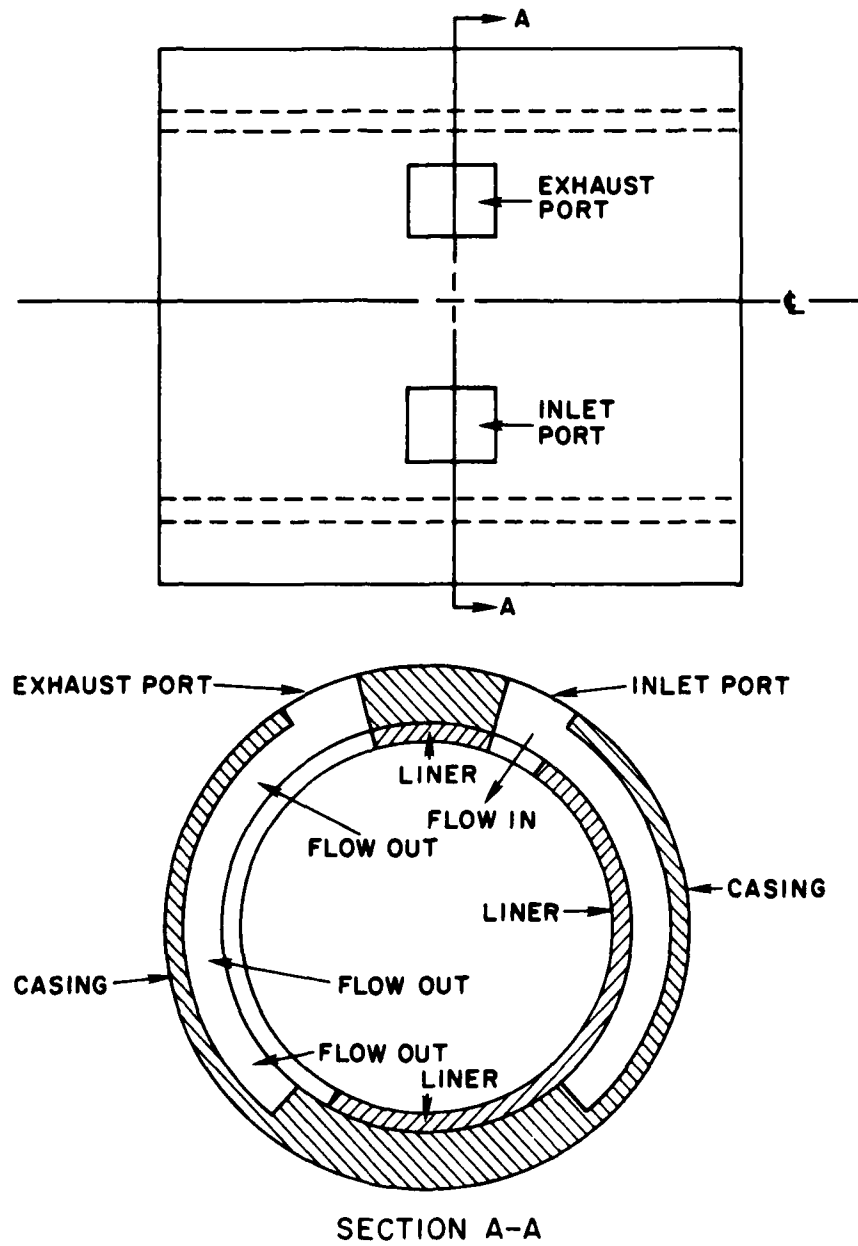


Figure 10. Stator Model

$$\bar{T}_\infty = \frac{\int T_\infty(t) dt}{\int dt}, \quad (3.14)$$

and the heat generation rate was computed as:

$$\bar{\dot{q}}_{\text{gen}}'' = \frac{\int \dot{q}_{\text{gen}}'' dt}{\int dt}. \quad (3.15)$$

The time dependent fluid temperatures and frictional heat generation rates, used in Equations (3.14) and (3.15) were obtained from the thermodynamic and friction models, respectively.

No iteration between the steam temperatures and heat transfer rates was done as in the case of the steam pressures and the leakage flow rates since the heat transfer did not appear to affect the component temperature profiles, as a result of changing the steam temperature, to the same degree as leakage affected the control volume pressure. The amount of frictional heat entering the stator and the vane was computed using Equation (3.11).

An estimate of the convective heat transfer coefficient was obtained by modeling the flow over the stator as flow over a constant temperature semi-infinite flat plate. The mean heat transfer coefficients from Reference 10 were for

LAMINAR FLOW:

$$Nu_x = 0.332 (Pr)^{1/3} (Re_x)^{1/2}$$

or

$$\bar{h} = \frac{2k}{L} 0.332 (Pr)^{1/3} (Re_L)^{1/2} \quad \text{and for} \quad (3.16)$$

MIXED LAMINAR - TURBULENT FLOW:

$$\bar{h} = \frac{k}{L} Pr^{1/3} (0.036 Re_L^{0.8} - 836) \quad . \quad (3.17)$$

Transition from laminar to turbulent flow was based on a critical Reynolds Number of 5×10^5 . The characteristic length used in computing the Reynolds Number and heat transfer coefficients was chosen as

$$L_S = (R_i + HR) ARC \quad . \quad (3.18)$$

The velocity used in computing the Reynolds Number was computed as

$$V_{MEAN/S} = (R_i + HR) \omega \quad . \quad (3.19)$$

Since the outside surface of the stator was insulated, an adiabatic boundary condition was employed there.

It was assumed that the surfaces of the inlet and exhaust ports in contact with the working fluid were at the inlet and exhaust temperature, respectively.

The stator was symmetric in the axial direction about a plane cutting through the center of the inlet and exhaust ports. Therefore, only one half of the axial length of the stator was used in computing the temperature profiles and heat transfer rates. An adiabatic boundary condition was employed at the axis of symmetry.

In order to avoid a computer storage problem which would have resulted when considering the stator and end plates together, they were analyzed separately. To permit separate analysis, it was assumed that the boundary between the stator and end plate was adiabatic.

3.4.4 End Plate, Three-Dimensional Model. To obtain the temperature profiles and heat transfer rates for the end plate, Equation (3.12) was transformed into finite difference form. The transformation is illustrated in Appendix C. The end plate was modeled as shown in Figures 11.

A combined convection and heat generation boundary condition was employed at the end plate surfaces that contact the working fluid

$$\left(-k \frac{\partial T}{\partial Z} = \bar{h}(T_{\infty} - T_w) + \dot{q}_{\text{gen}}''\right) .$$

Since the fluid temperature and heat generation rate varied with time, Equations (3.14) and (3.15) were used to compute the time averaged fluid temperature and heat generation rates for a particular point on the end plate. The time dependent fluid temperatures and frictional heat generation rates used in Equations (3.14) and (3.15) were obtained from the thermodynamic and friction models, respectively. Like the stator, no iteration between the steam temperature and heat transfer rates was done. The fraction of the total frictional heat generated between the vane and end plate that entered the end plate was computed using Equation (3.11). The heat transfer coefficients for the end plate were computed using Equations (3.16) and (3.17). The characteristic length used in computation of the Reynolds Numbers and heat transfer coefficients was chosen as:

$$L_E = \frac{\int_{R_1}^{R_1+HR} \int_0^{\text{ARC}} r \, dr \, d\theta}{\int_{R_1}^{R_1+HR} dr} = \left(R_1 + \frac{HR}{2}\right) \text{ARC} . \quad (3.20)$$

The velocity used in computing the Reynolds Number was computed as:

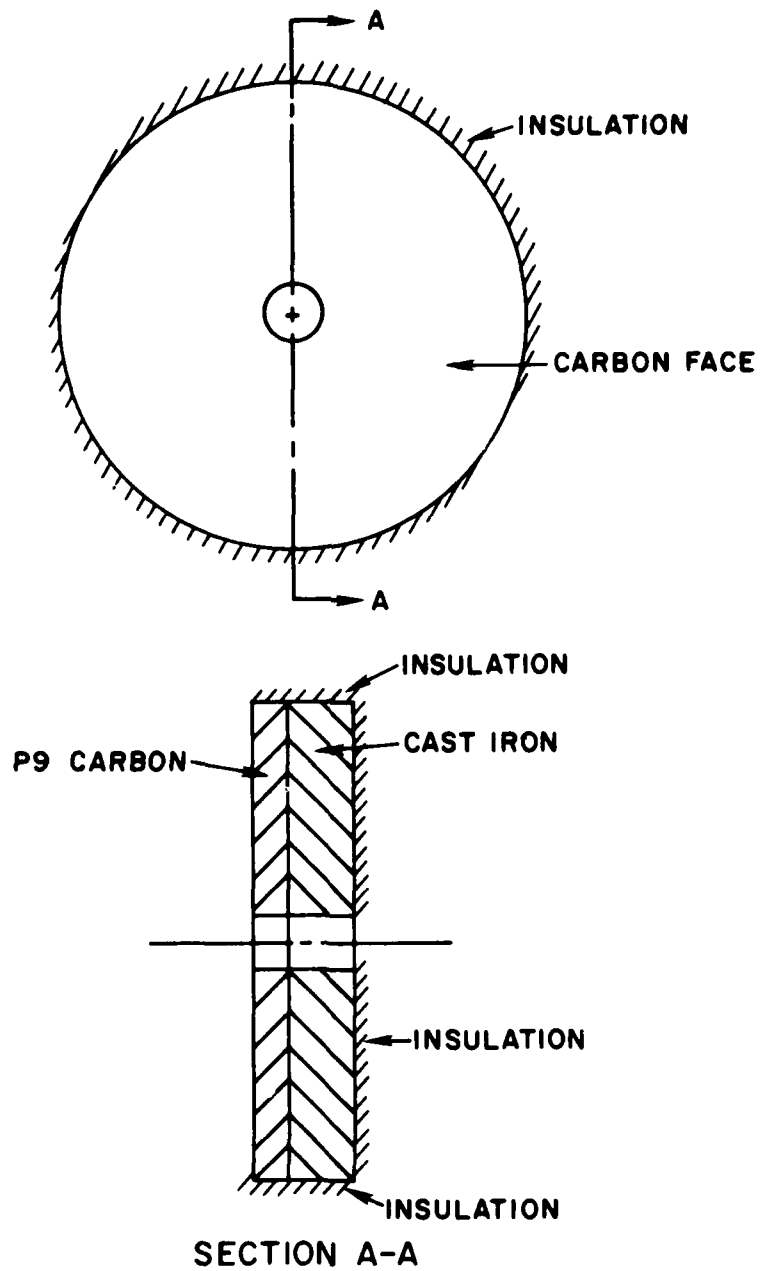


Figure 11. End Plate Model

$$V_{\text{MEAN}/E} = \frac{\omega \int_{R_1}^{R_1+HR} r \, dr}{\int_{R_1}^{R_1+HR} dr} = \left(R_1 + \frac{HR}{2}\right) \omega \quad (3.21)$$

Consistent with the stator analysis, the surface of the end plate which contacted the stator was assumed to be adiabatic ($\frac{\partial T}{\partial z} = 0$).

Since there was no contact between the rotor and end plate, there was no heat generated on the end plate surface by rotor friction. However, there was leakage between the rotor and end plate. To model this condition, a convective boundary condition was employed on those surfaces of the end plate which were covered by the rotor but did not contact a vane $\left[-\frac{\partial T}{\partial z} = \frac{\bar{h}}{k} (T_\infty - T_w)\right]$.

The periphery of the hole in the end plate through which the rotor shaft extended was also assumed to be an adiabatic surface ($\frac{\partial T}{\partial r} = 0$). The shaft did not contact the end plates at this point, so no frictional heat was generated. Furthermore, since the rotor shaft was sealed at both ends, it was assumed that steam leakage between the end plate hole and rotor shaft would be small. It was possible that natural convection might have existed, but it would have been small in comparison to the other modes of heat transfer to the end plate.

Since the end plates were insulated, the outside surfaces of the end plates were assumed adiabatic.

3.5 Numerical Procedure

A finite difference method was used to obtain solutions to the expander heat transfer analysis.

3.5.1 Transient Analysis. The rapidly fluctuating surface temperature, used as a rotor boundary condition, required the use of small time steps to analytically synthesize the temperature fluctuations. The stability requirements for the explicit method were determined using the technique of Karplus [11,12]. It was found that the time steps required for stability were not prohibitive in view of the rapidly changing rotor surface temperature. Therefore, the explicit method was utilized in the rotor heat transfer analysis.

When employing the explicit method, the Laplacian ($\nabla^2 T$) was put into finite difference form using the method of Taylor's Series expansion [11,13]. A forward difference approximation was used to approximate the transient term ($\frac{\partial T}{\partial t}$). This is illustrated in Appendix C.

3.5.2 Steady State Analysis. The method of Taylor's Series expansion was used to obtain the finite difference approximation to the Laplacian ($\nabla^2 T$). The set of algebraic equations that resulted from the finite difference analysis were solved using the iterative method of Gauss-Seidel with the incorporation of Young's over relaxation factor parameter [7].

CHAPTER IV

EXPERIMENTAL AND THEORETICAL RESULTS

4.1 Experimental Conditions

The expander, described in Chapter 2, was tested with a 22.5° and a 45° arc of admission. For each arc of admission, supply pressures of 150 psia and 115 psia were employed. The supply temperatures for the 150 psia and 115 psia supply pressures were $370^{\circ}\text{F} \pm 10^{\circ}\text{F}$ and $360^{\circ}\text{F} \pm 10^{\circ}\text{F}$, respectively. The speed was varied from 840 to 1913 RPM.

Initial testing of the expander was conducted using no internal lubrication. However, in an attempt to reduce component wear and to decrease leakage by partially blocking the leakage paths with oil, all the data included herein was collected using an oil flow rate of 0.05 lb_m/min. This compared with a steam flow rate on the order of 5 lb_m/min.

4.2 Experimental Results

4.2.1 Power. Figures 12 and 13 are representative pressure versus volume diagrams constructed from the measured internal expander pressures. The experimentally determined data points are indicated on the curves. However, portions of the diagram were constructed by assuming the pressures in the control volume at the inlet and the exhaust ports were the supply and exhaust pressures, respectively. This is a good assumption since the vane expander is an easy breathing device. This has been verified analytically in Reference 1, and by the

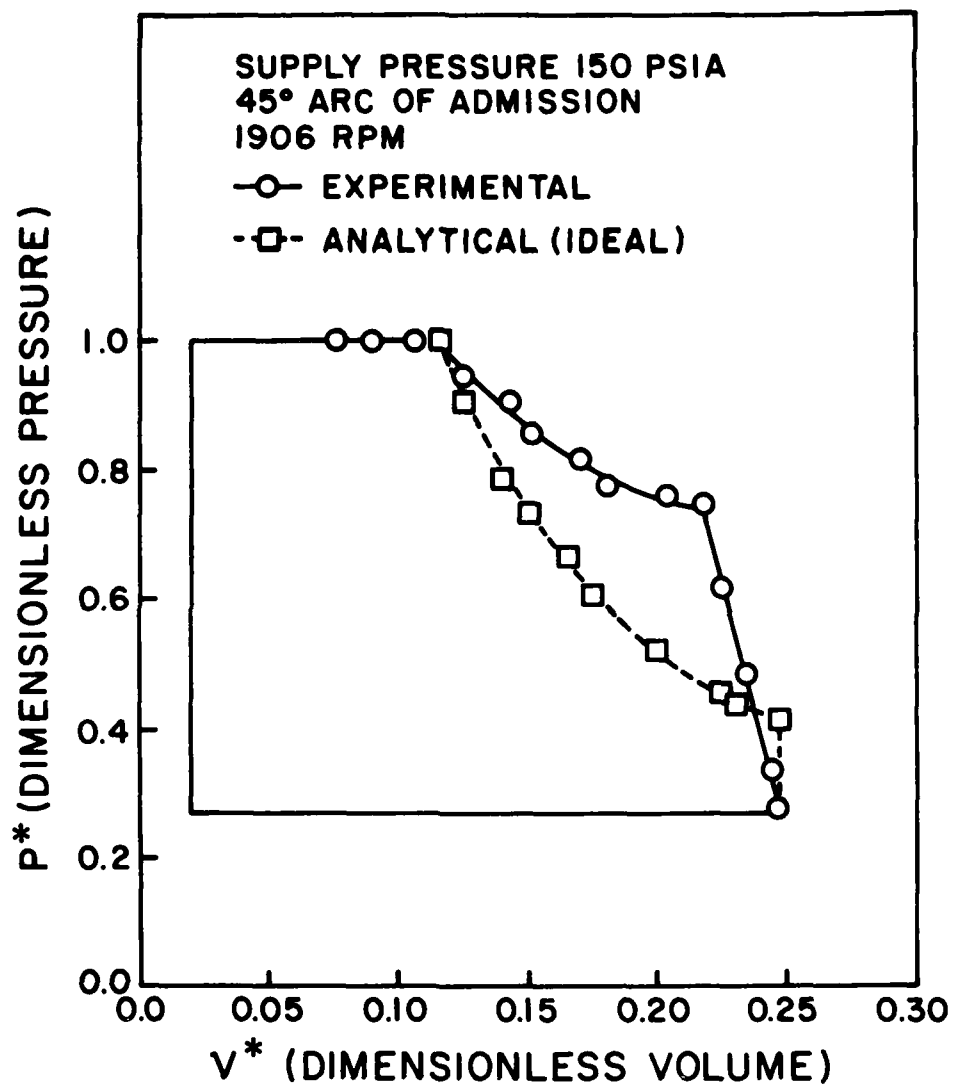


Figure 12. Pressure Versus Volume for 150 psia Supply Pressure 22.5° Arc of Admission

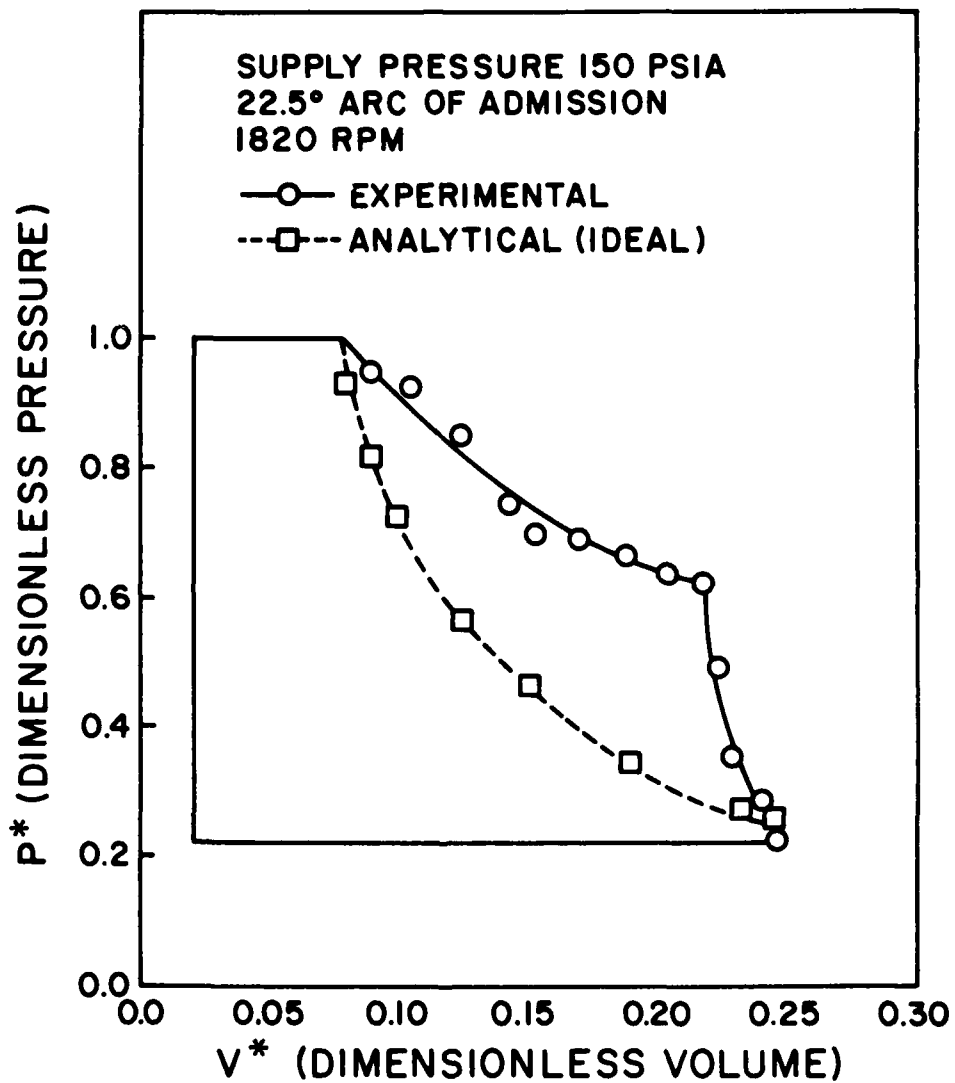


Figure 13. Pressure Versus Volume for 150 psia Supply Pressure 45° Arc of Admission

experimental work discussed in Reference 4. Included in Figures 12 and 13 are the ideal $P^* - V^*$ curves for the expander. The ideal curve is based on the analysis of an expander with no friction, leakage or heat transfer. During the expansion portion of the cycle, the measured control volume pressures are higher than the ideal values. This is primarily due to leakage from the region exposed to the inlet port into the lower pressure control volumes. The rapid decrease in control volume pressure prior to opening the exhaust port is due to leakage out of the expanding control volume to the low pressure region exposed to the exhaust port.

The increased area of the actual $P^* - V^*$ diagram, compared to the ideal diagram, illustrates that leakage increased the expander power output.

The indicated work per revolution done by the expander was numerically computed as

$$W = \int_{\text{rev}} PdV \quad (4.1)$$

using the measured pressures and the known volume variation. Figures 14 and 15 show the indicated power as a function of speed for the 22.5° and 45° arcs of admission and supply pressures of 150 psia and 115 psia. Due to the larger arc of admission, higher indicated power outputs were obtained for the 45° arc of admission. The difference in indicated power, for the two arcs of admission, would have been greater had the back pressure on the expander not increased, due to increased mass flow, at the larger arc of admission. The shaft power, as measured by the dynamometer, and the frictional power loss are also shown in Figures 14

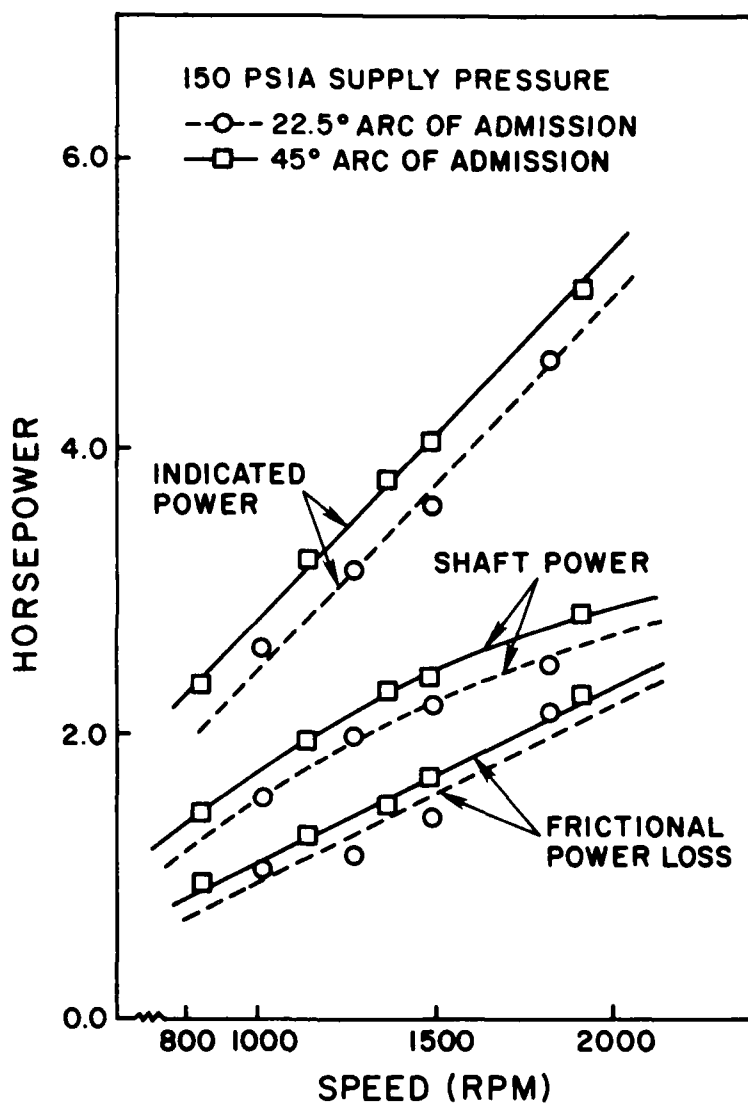


Figure 14. Power Versus Speed for 150 psia Supply Pressure

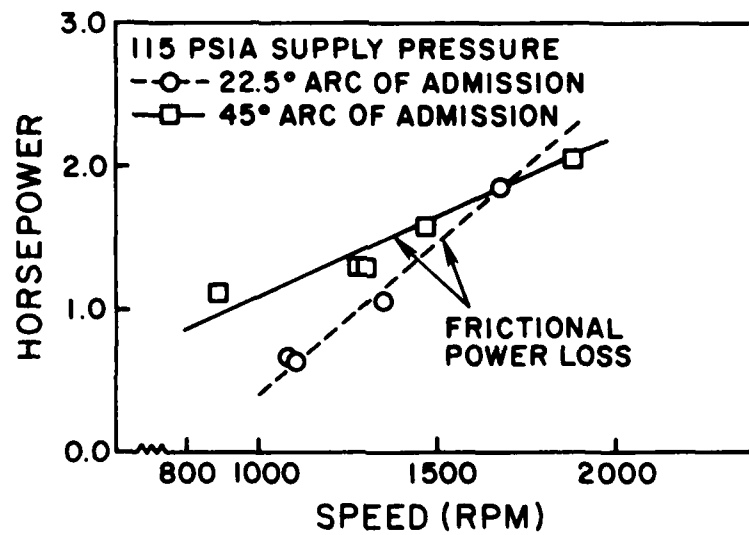
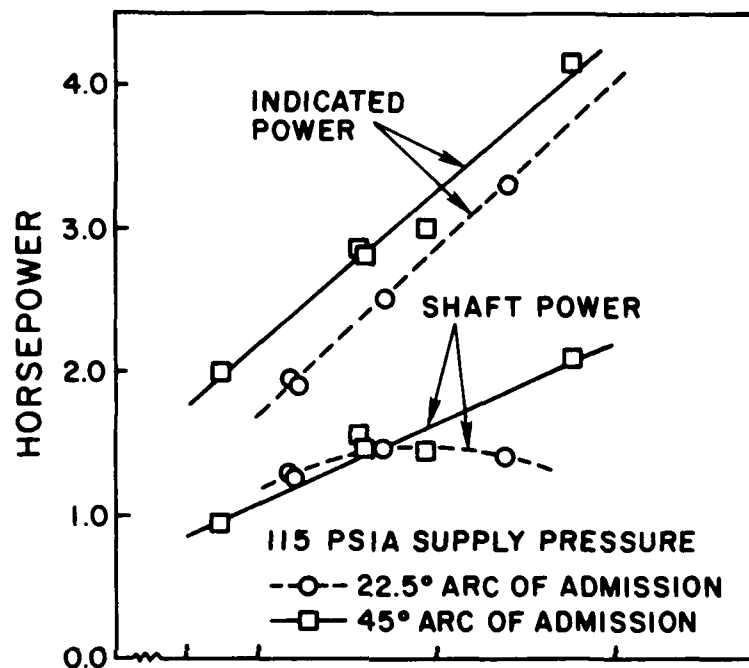


Figure 15. Power Versus Speed for 115 psia Supply Pressure

and 15. The frictional power loss was determined as the difference between the indicated power and the measured shaft power. Over the entire speed range for 150 psia supply pressure and over the majority of the speed range for 115 psia supply pressure, the 45° arc of admission data shows a greater frictional power loss. This was due to higher pressure forces being applied to the vane over a greater portion of the cycle for the larger arc of admission. The larger pressure forces produce an increase in vane friction. Figure 15 shows that for a supply pressure of 115 psia, the frictional power loss for the 22.5° arc of admission exceeded the frictional power loss for the 45° arc of admission at speeds above 1650 RPM. This was probably due to a variation in the coefficient of sliding friction. However, since the coefficient of friction is dependent on many factors such as load, and the amount and location of lubricating oil and liquid water, it is difficult to explain why the variation may have occurred.

Figure 14 shows that although the indicated and frictional power increased linearly with speed, the shaft power curve begins to bend near 1500 RPM, for a supply pressure of 150 psia. This is due to a decrease in the mechanical efficiency (mechanical efficiency = $\frac{\text{shaft horsepower}}{\text{indicated horsepower}}$) at the higher speed. The decrease in mechanical efficiency is a result of the frictional power loss becoming a larger percentage of the indicated power. The variation of mechanical efficiency with speed for a supply pressure of 150 psia is shown in Figure 16.

For a supply pressure of 115 psia, and a 22.5° arc of admission, the shaft power curve begins to bend at approximately 1300 RPM. For this supply pressure, the 45° arc of admission data show a continuous increase

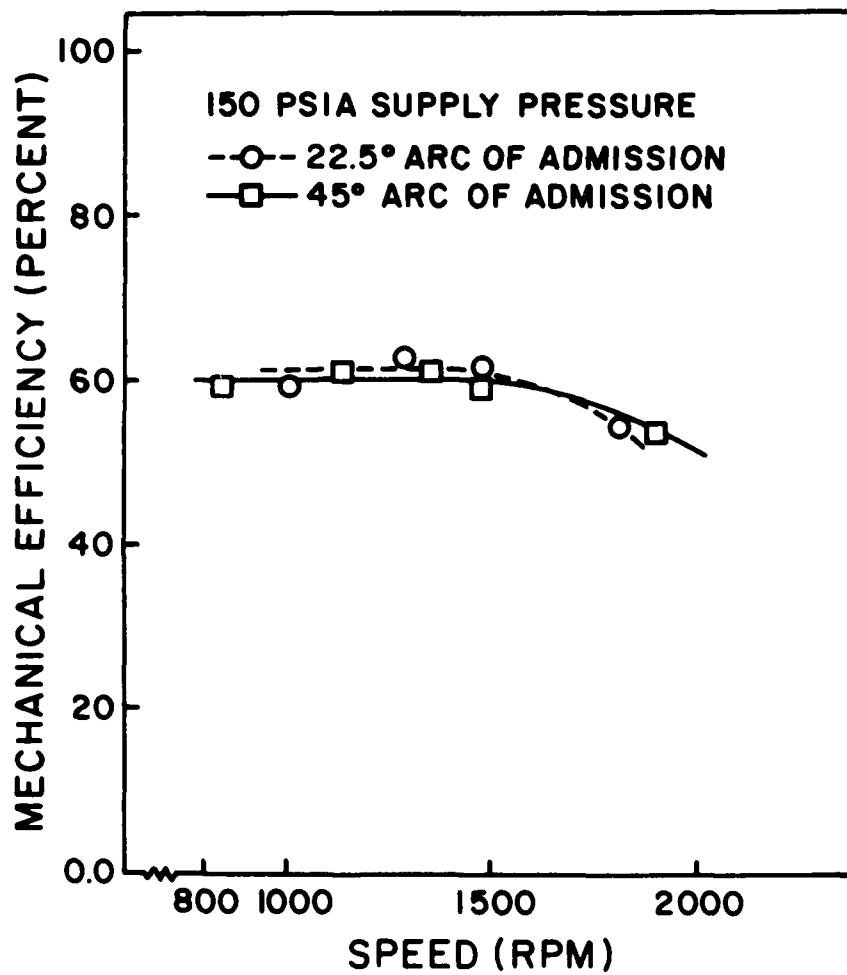


Figure 16. Mechanical Efficiency Data 150 psia Supply Pressure

in shaft power with speed. Figure 17 shows that the mechanical efficiency, for a 22.5° arc of admission and 115 psia supply pressure, drops off quite rapidly. This decrease in mechanical efficiency, caused by friction, results in the bending of the 22.5° arc of admission shaft-power curve. The mechanical efficiency for the 45° arc of admission and 115 psia supply data, while varying with speed, shows no definite trend downward at the higher speeds.

4.2.2 Mass Flow Rate. Figures 18, 19, 20 and 21 show the measured mass flow rate, the ideal flow rate and the leakage flow rate as a function of speed for 45° and 22.5° arcs of admission and 115 psia and 150 psia supply pressures. In all cases, the flow rate of steam increased with speed. Ideally, for an easy breathing expander, the control volume contains the same mass of steam per revolution, independent of speed. Therefore, as the speed increases the mass flow rate increases. The ideal mass flow rate was computed as the product of the number of control volumes, the volume of a control volume at intake closing, the density of the supply steam, and the speed in revolutions per minute. The leakage flow was computed as the difference between the measured flow rate and the ideal flow rate.

In all cases studied, the leakage flow remained approximately constant with speed. The clearances in the expander do not change with speed and for an easy breathing expander, the pressures in the control volume do not vary greatly with speed. Since the leakage driving potential and flow resistance do not vary with speed, it is consistent that the leakage flow rate would not change greatly with speed.

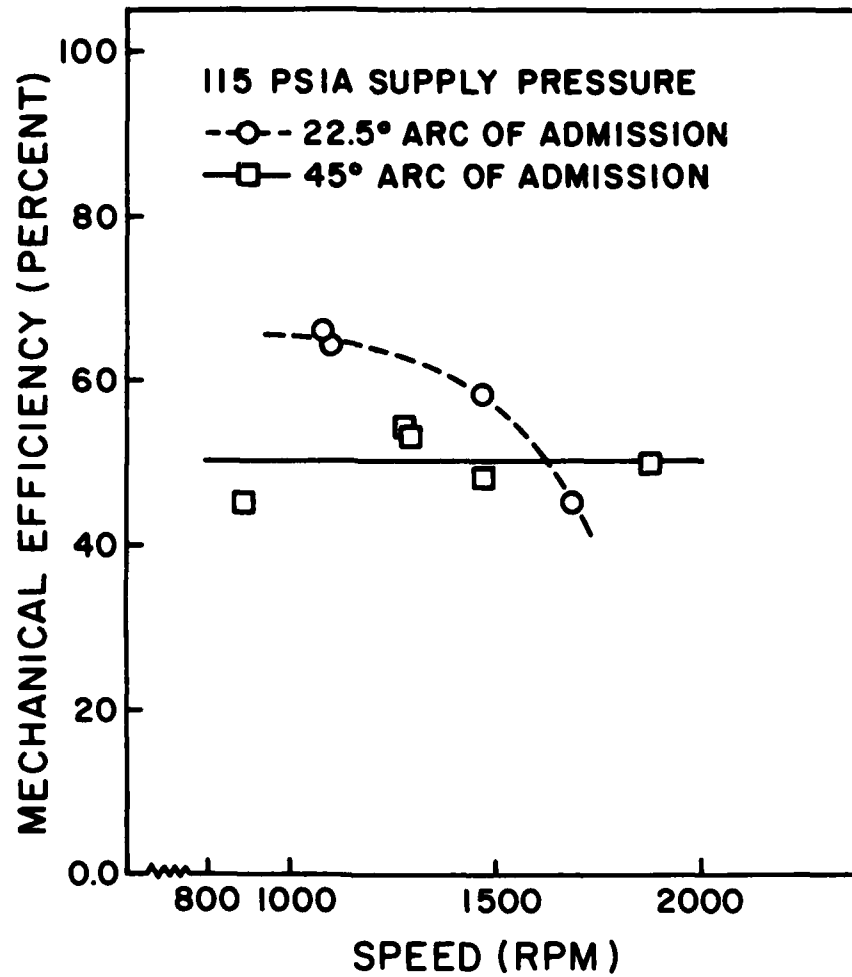


Figure 17. Mechanical Efficiency Data 115 psia Supply Pressure

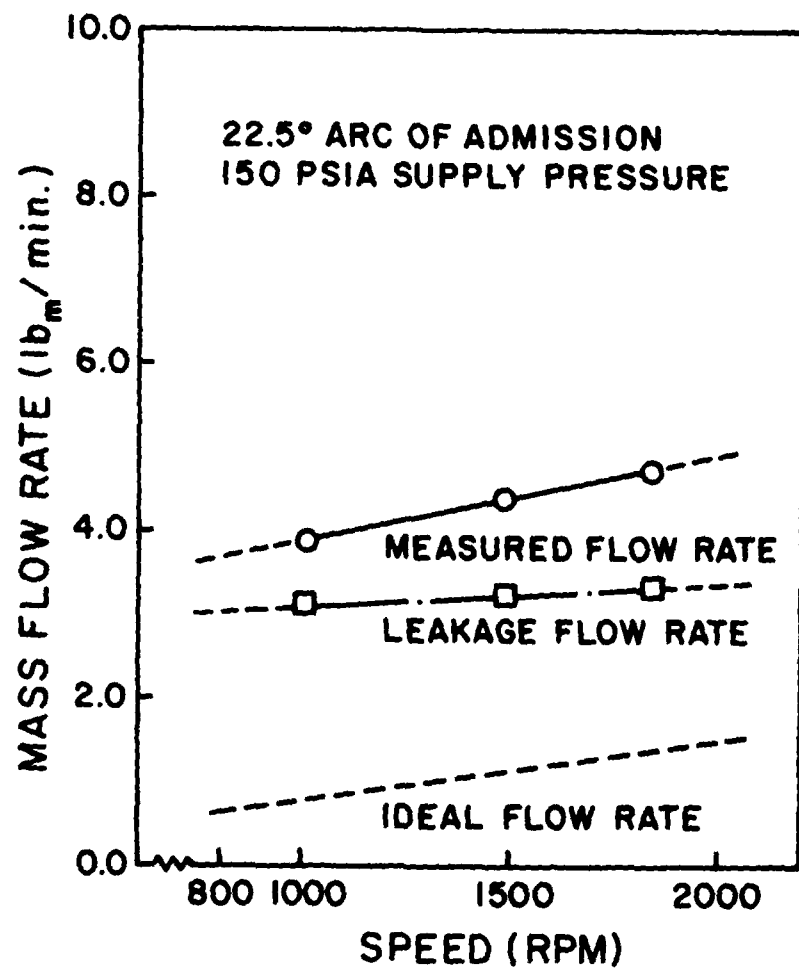


Figure 18. Mass Flow Rate Data for 150 psia Supply Pressure
22.5° Arc of Admission

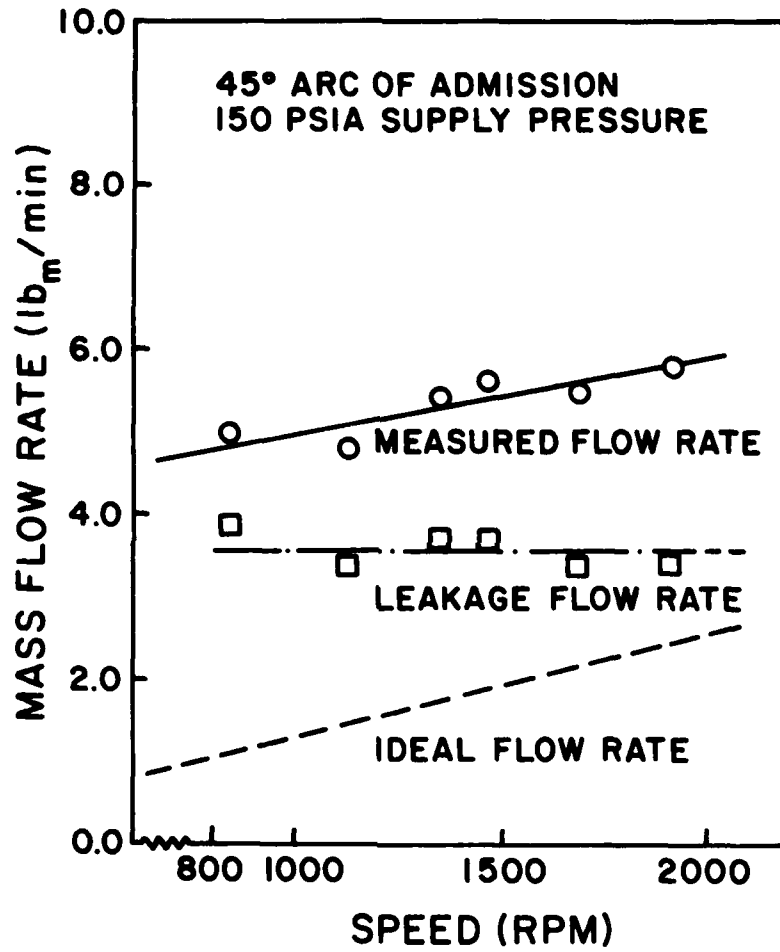


Figure 19. Mass Flow Rate Data for 150 psia Supply Pressure
45° Arc of Admission

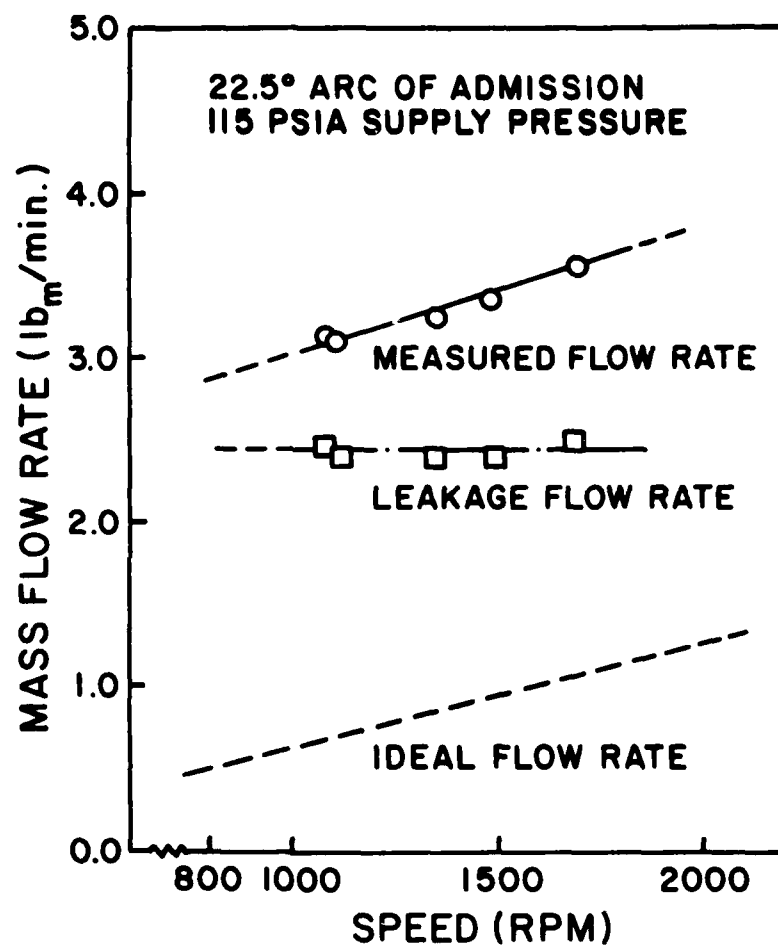


Figure 20. Mass Flow Rate Data for 115 psia Supply Pressure
22.5° Arc of Admission

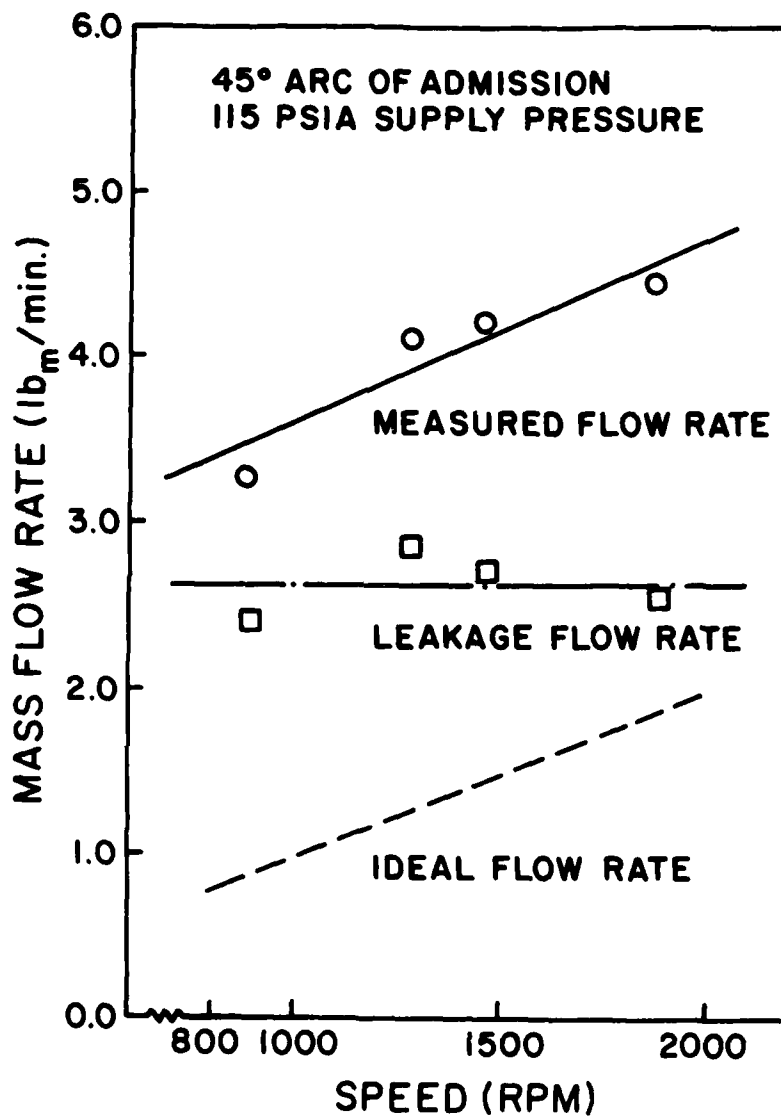


Figure 21. Mass Flow Rate Data for 115 psia Supply Pressure
45° Arc of Admission

Comparison of Figures 18 and 19 indicates that for the same supply pressure, the leakage flow increases with arc of admission. The same trend is observed by comparison of Figures 20 and 21. The resistance to leakage flow, for a control volume at any specified position, does not change with arc of admission; but the pressures in the control volumes are maintained at higher values over a greater portion of the cycle with the larger arc of admission. This greater driving potential is apparently the cause for higher leakage at the larger arc of admission.

Comparisons of Figures 18 and 20, and Figures 19 and 21, show that for the same arc of admission, the leakage flow increases with supply pressure. This would also appear to be due to the increased driving potential.

4.2.3 Adiabatic Expansion Efficiency. Figure 22 shows the adiabatic expansion efficiency for both arcs of admission at a supply pressure of 150 psia. The adiabatic expansion efficiency is defined as the ratio of the work per pound of steam, to the isentropic enthalpy change from the supply conditions to the exhaust manifold pressure. The low values of efficiency, shown in Figure 22, are primarily the result of leakage and friction.

Leakage has its greatest effect at low speeds. If all losses but leakage are neglected, and it is assumed that leakage does not increase the power output, the adiabatic expansion efficiency can be written as

$$\eta_{\text{ADIABATIC EXPANSION}} = 1 - \frac{\dot{m}_L}{\dot{m}_T} \quad (4.2)$$

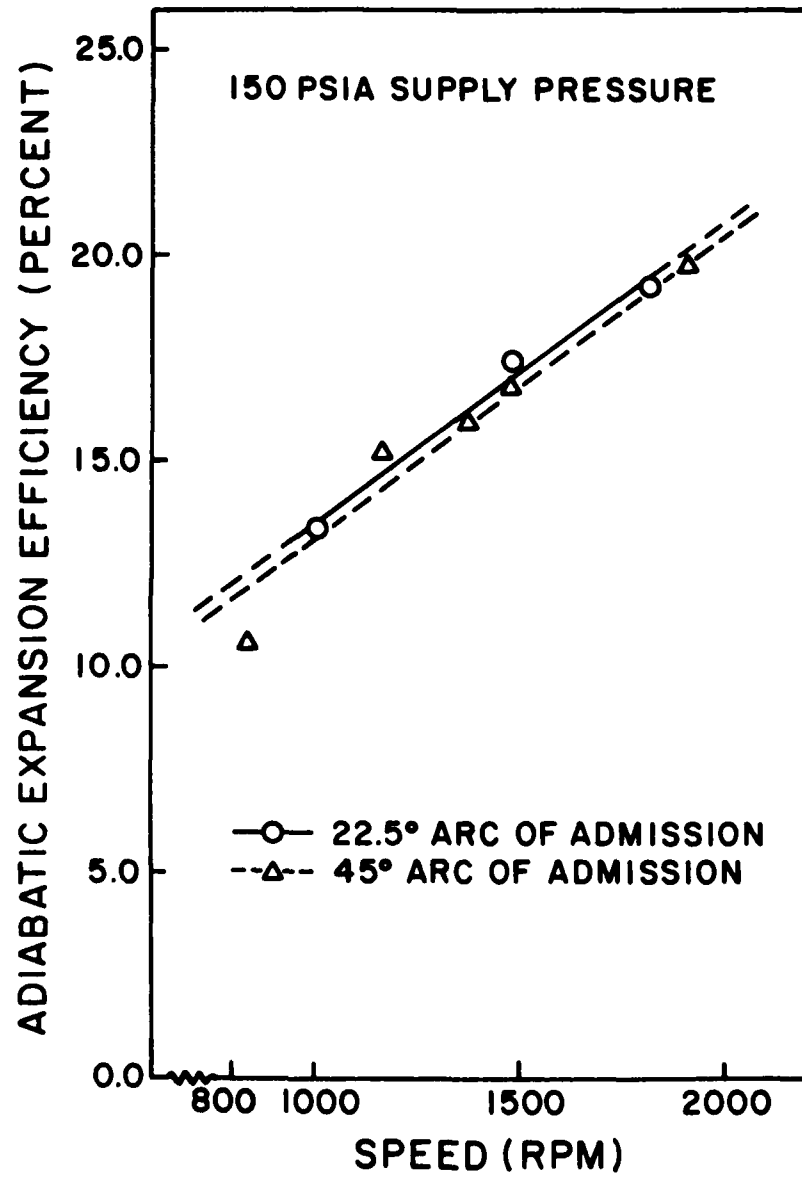


Figure 22. Adiabatic Expansion Efficiency Data for 150 psia Supply Pressure

where \dot{m}_L is the leakage flow rate and \dot{m}_T is the total flow rate ($\dot{m}_T = \dot{m}_{IDEAL} + \dot{m}_L$). Therefore, for a given ideal flow rate, as the leakage flow increases, the efficiency decreases. The effect of leakage on the adiabatic expansion efficiency is reduced somewhat since leakage does increase the expander power output. Figures 18 through 21 showed that the experimentally computed leakage flow rates did not vary greatly with speed. However, the ideal flow rate is directly proportional to speed. This implies that as the speed increases, the ratio of leakage flow to total flow decreases resulting in a smaller adiabatic expansion efficiency reduction due to leakage.

The effect of friction on the adiabatic expansion efficiency increases with increased speed. For an easy breathing expander, the frictional forces increase slightly with speed due to larger vane accelerations. The distance per unit time over which the frictional forces act also increases directly with speed. Therefore, as shown in Figures 14 and 15, the frictional power loss increases with speed.

Under the influence of friction and leakage, a peak in the adiabatic expansion efficiency versus speed will occur. Low efficiencies at speeds less than the peak efficiency speed would be primarily due to leakage. The low efficiencies at speeds greater than peak efficiency speed would be primarily due to friction.

Figure 22 shows that at 150 psia supply pressure and arcs of admission of 22.5° and 45°, the experimentally determined efficiency continuously increased with speed. This was due to a decrease in the ratio of leakage flow rate to total mass flow rate. For the conditions shown in Figure 22, the peak adiabatic expansion efficiency was not reached.

Figure 23 shows the same trend for the 45° arc of admission and 115 psia supply pressure. However, for the 22.5° arc of admission and 115 psia supply pressure, a peak in the experimental adiabatic expansion efficiency was observed at approximately 1450 RPM. The decrease in efficiency with speed above 1450 RPM was due to frictional power losses. The severe effect of friction for a supply pressure of 115 psia and an arc of admission of 22.5° was previously illustrated by the rapid drop in mechanical efficiency shown in Figure 17.

4.2.4 Temperature Measurement Results. The liner and end plate temperatures were measured for determining thermal expansions and for comparison with the temperatures predicted by the heat transfer analysis. The rotor surface temperature was measured so that it could be used as a boundary condition in the heat transfer analysis. It also permitted computation of the approximate rotor thermal expansion.

Figures 24 through 27 show the measured stator temperature profiles (the points indicate the experimental data) for the 22.5° and 45° arcs of admission and supply pressures of 150 psia and 115 psia. The temperatures were measured 0.0625 inches from the expander end plate and 0.050 inches from the inside surface of the stator. The temperatures have been normalized by the supply temperature. Although the stator temperature is higher on the inlet side of the expander, the temperature profile is not severely distorted. Temperature differences between the inlet and exhaust side of the expander can result in distortion of the expander stator. Distortion of the stator would make it more difficult to maintain small clearances between the rotor and end plates without producing large frictional losses.

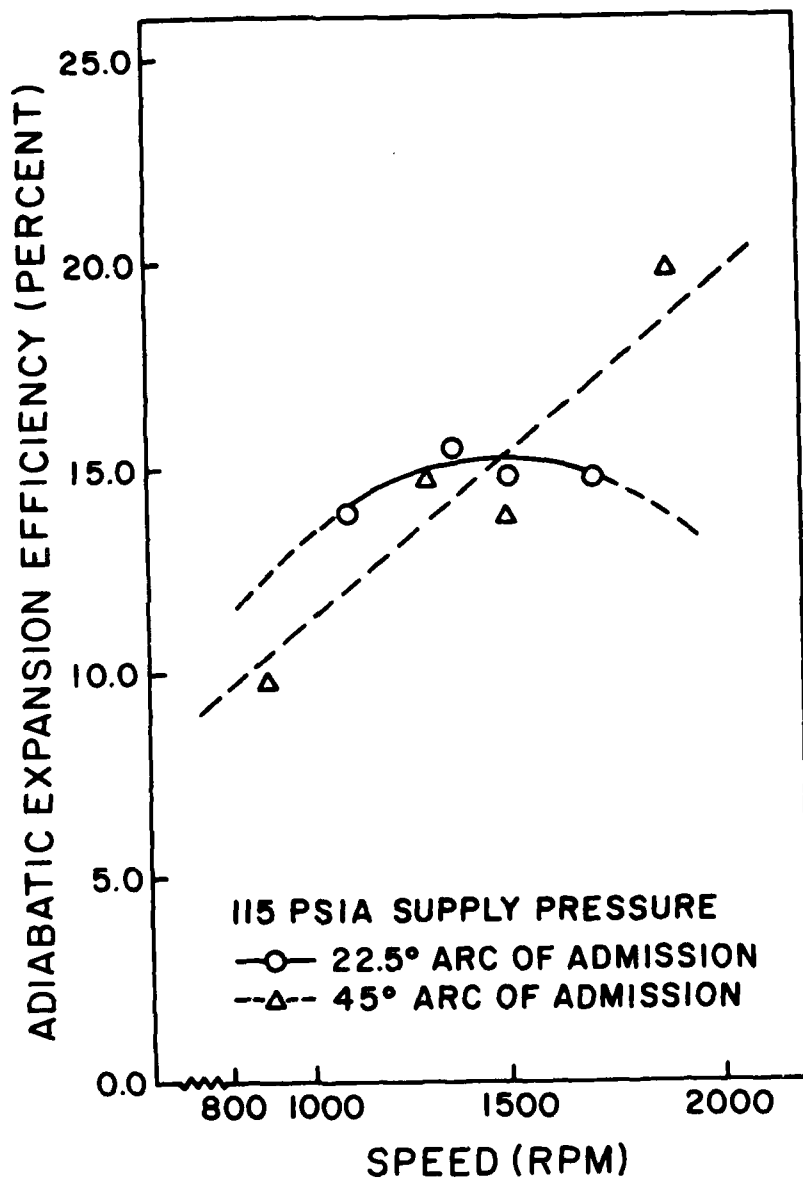


Figure 23. Adiabatic Expansion Efficiency Data for 115 psia Supply Pressure

22.5° ARC OF ADMISSION
150 PSIA SUPPLY PRESSURE

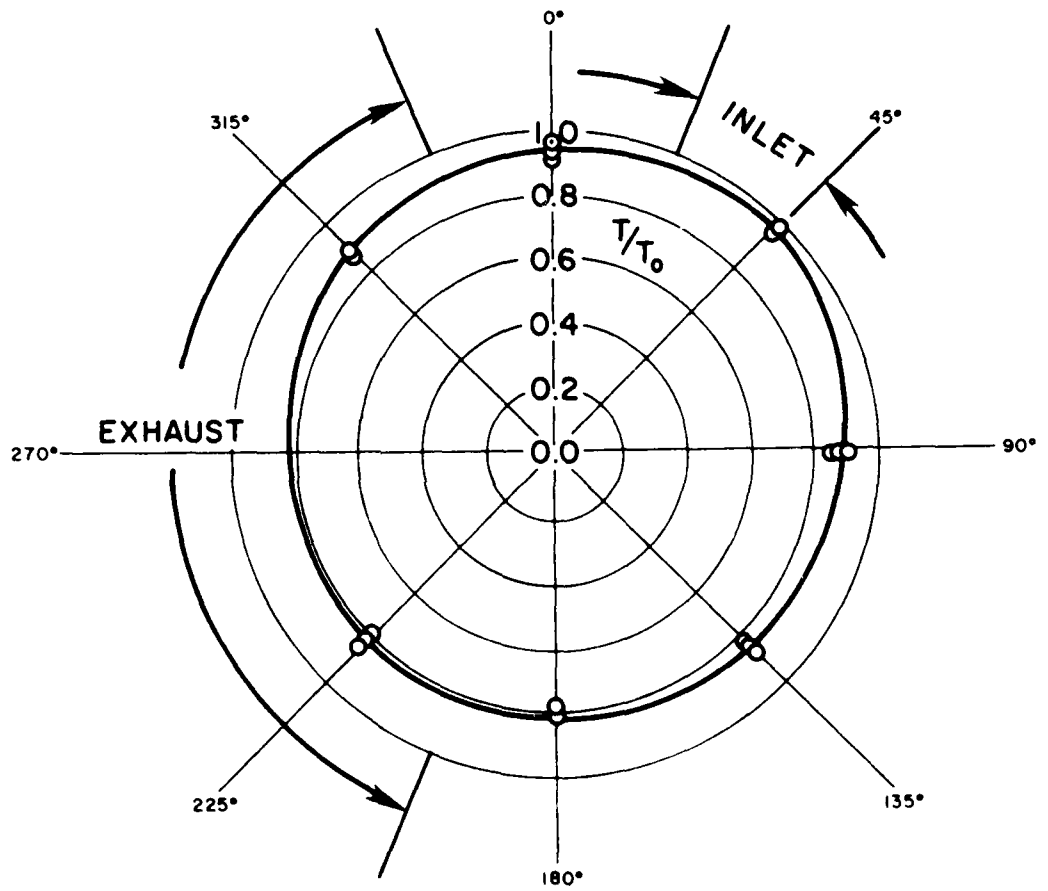


Figure 24. Stator Temperature Profile Data for 150 psia Supply Pressure 22.5° Arc of Admission

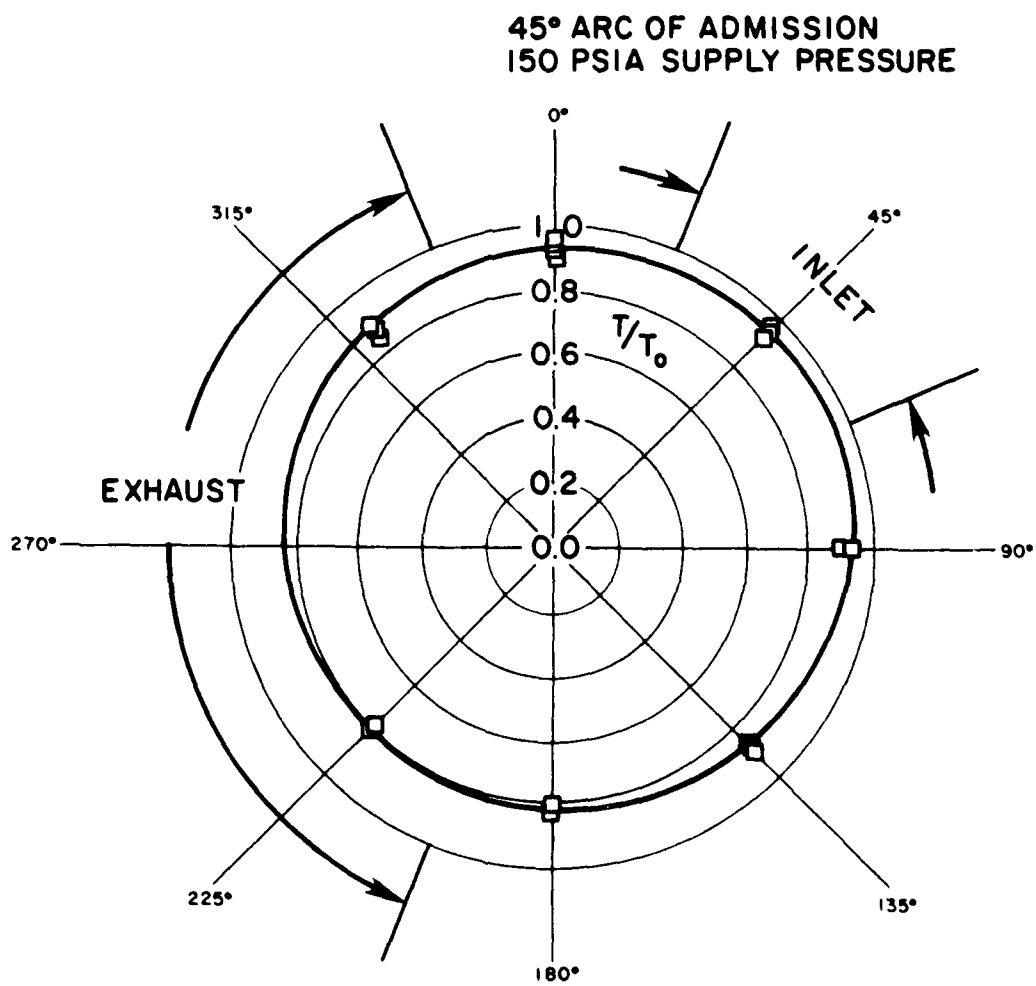


Figure 25. Stator Temperature Profile Data for 150 psia Supply Pressure 45° Arc of Admission

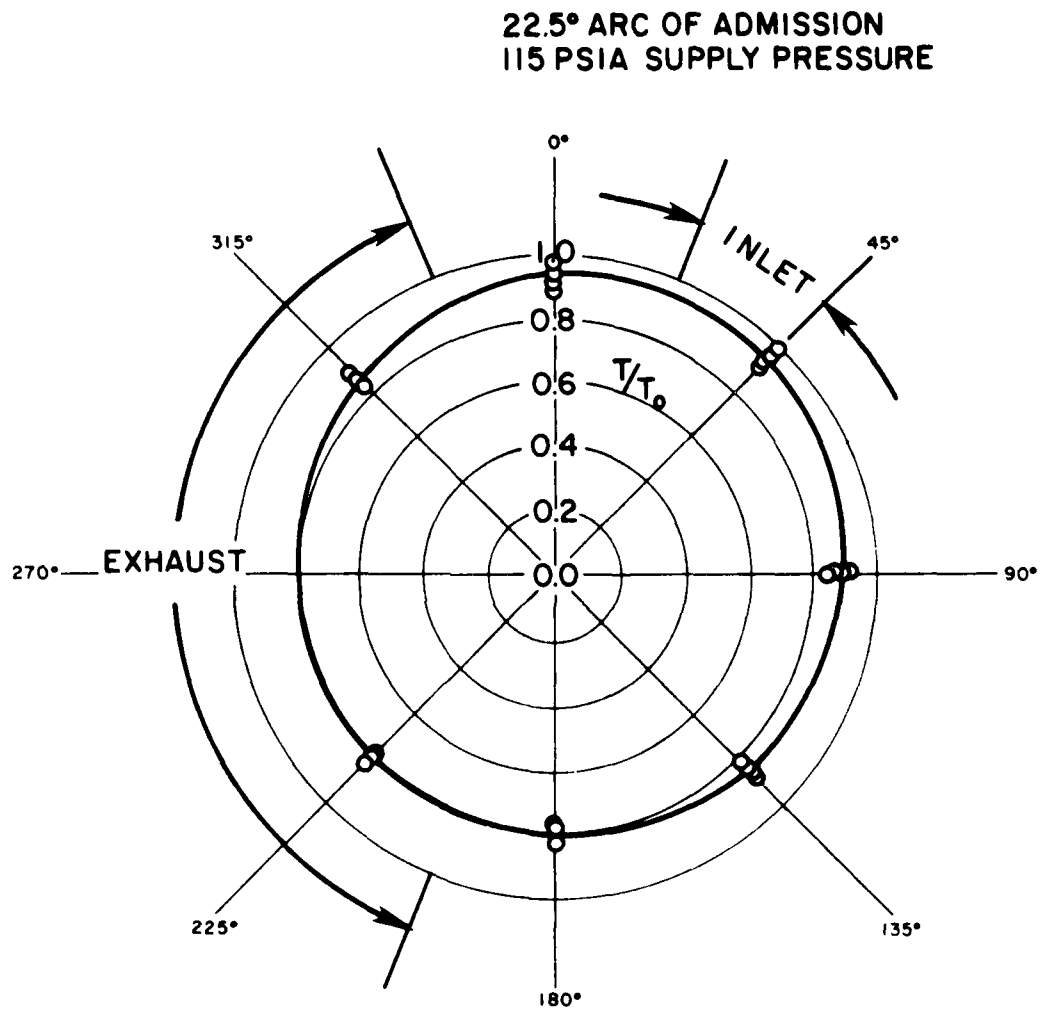


Figure 26. Stator Temperature Profile Data for 115 psia Supply Pressure 22.5° Arc of Admission

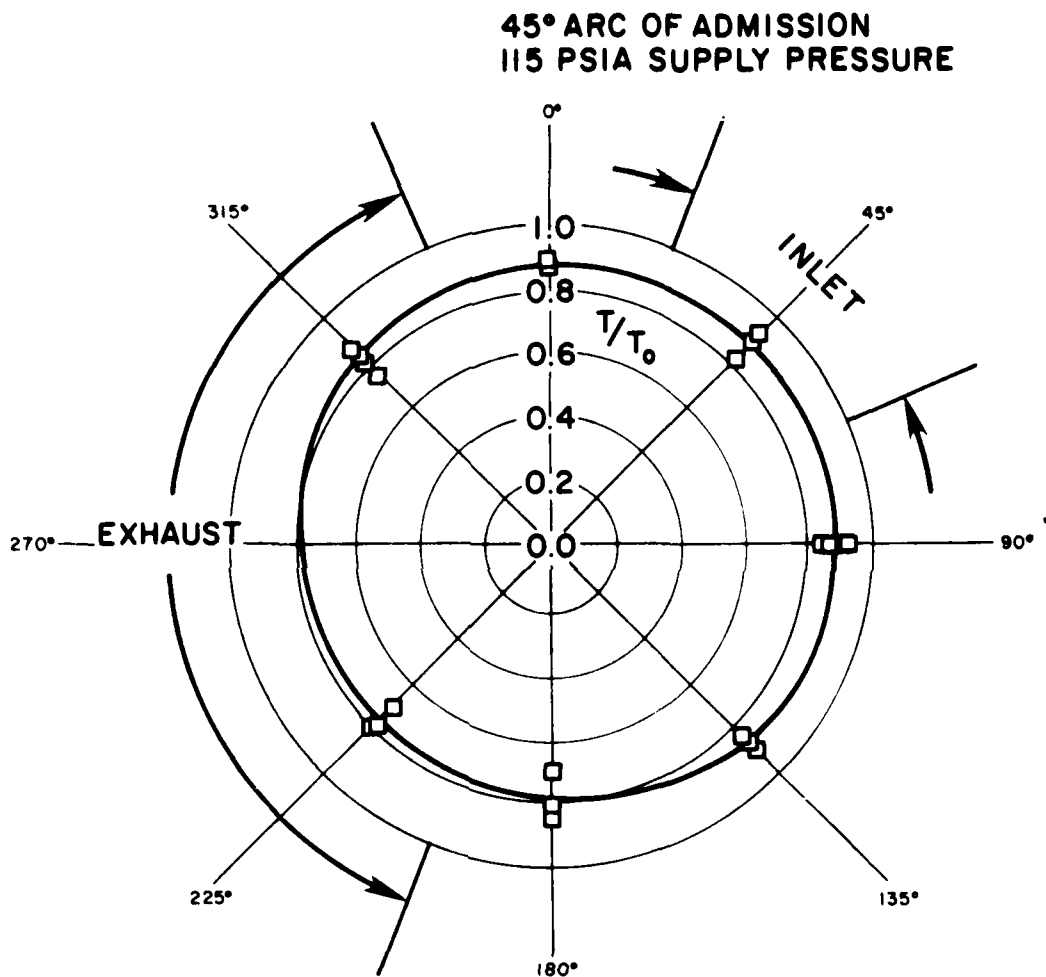


Figure 27. Stator Temperature Profile Data for 115 psia Supply Pressure 45° Arc of Admission

Comparison of Figures 24 through 27 shows that there is no significant difference between the stator temperature profiles for the 22.5° and the 45° arc of admission cases. Also, the supply pressure does not significantly affect the normalized temperature profile.

Figures 28 through 31 illustrate that there is no severe distortion of the end plate temperature profile. The arc of admission and supply pressure also does not greatly affect the end plate normalized temperature profile.

Figure 32 shows representative curves of the normalized rotor surface temperature as a function of rotor position. The data indicates that the rotor surface temperature increases when the surface is exposed to the high temperature supply steam. The surface temperature begins to decrease when the inlet port is closed and continues to decrease until the inlet reopens.

The variation of the rotor surface temperature with rotor position is not large. This is due to the small time during each revolution for the transfer of heat between the rotor and the working fluid.

The rotor surface temperature at the point of the inlet opening was below the saturation temperature of the supply steam. This would indicate that some condensation of the steam occurred. Condensation will be discussed in a later section.

4.2.5 Expander Heat Loss. The net heat loss from the expander was determined by applying the first law of thermodynamics to the expander. Table 2 summarizes the computed heat losses for the tests conducted. The values predominantly range from 3000 to 7500 BTU/hr

22.5° ARC OF ADMISSION
150 PSIA SUPPLY PRESSURE

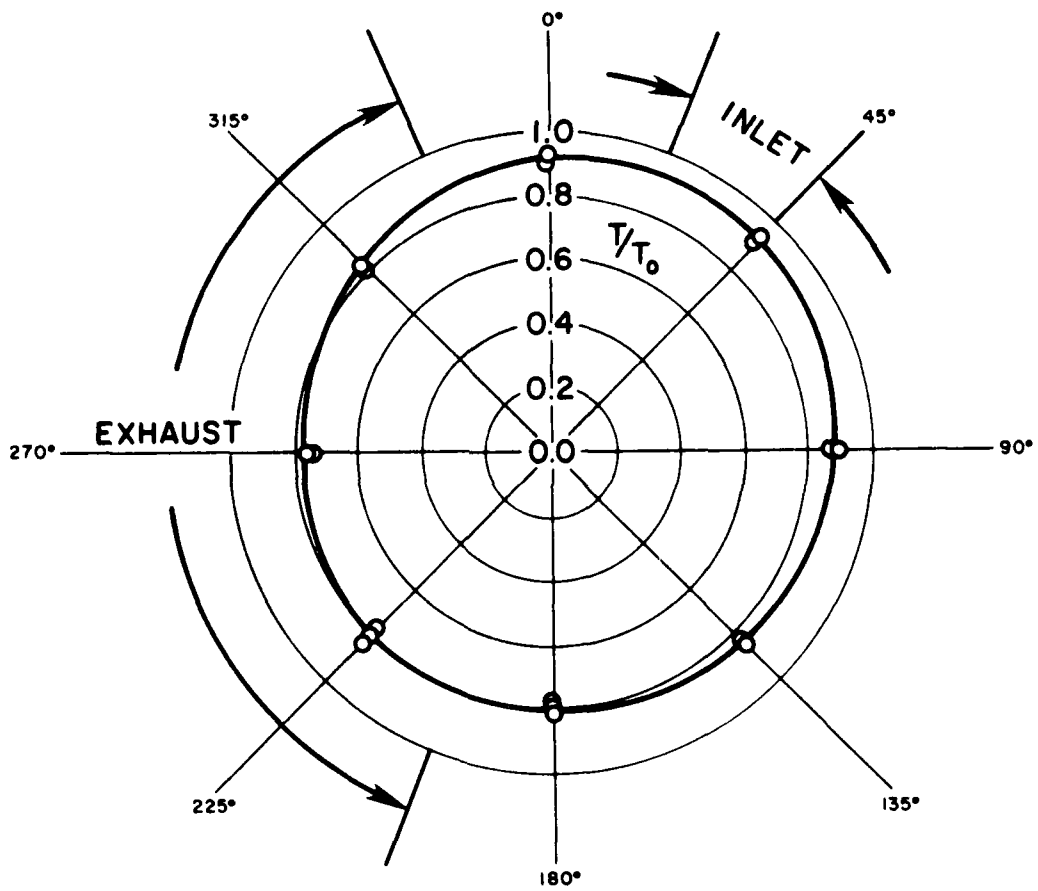


Figure 28. End Plate Temperature Profile Data for 150 psia Supply Pressure 22.5° Arc of Admission

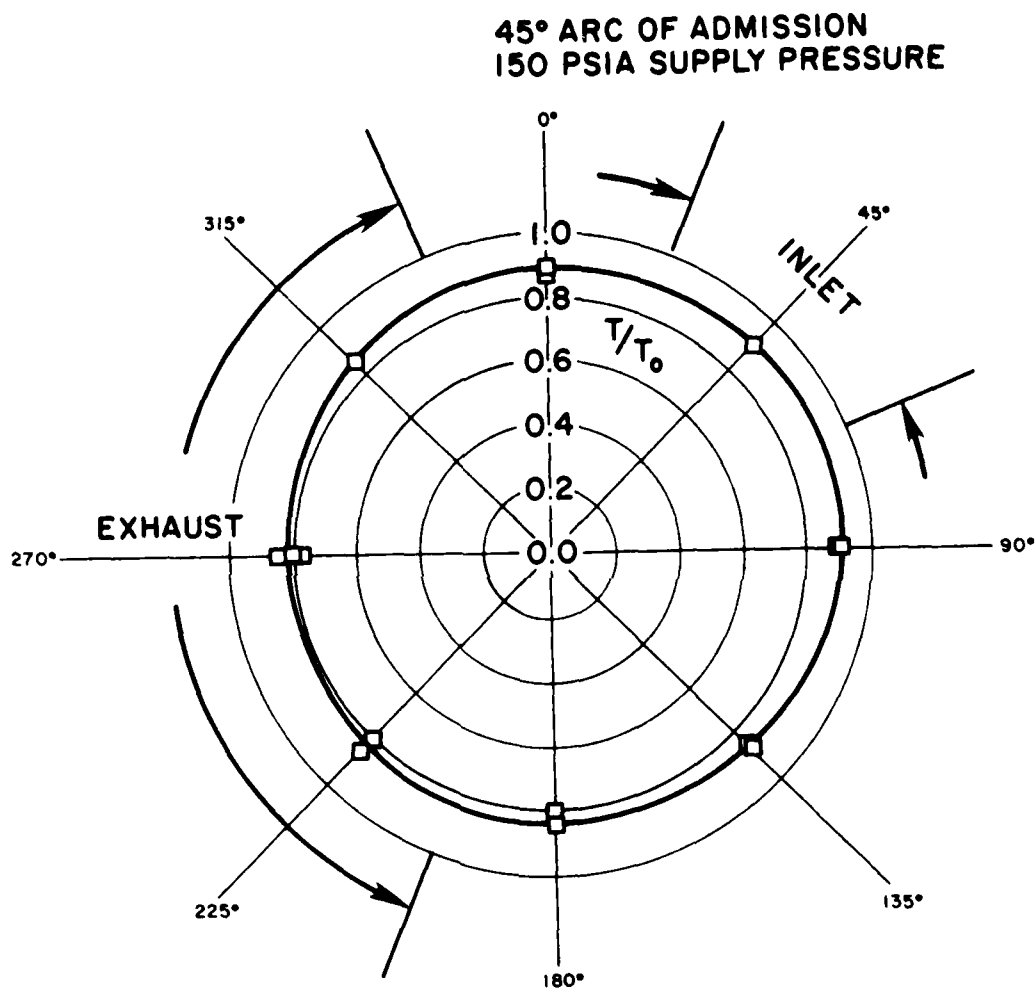


Figure 29. End Plate Temperature Profile Data for 150 psia Supply Pressure 45° Arc of Admission

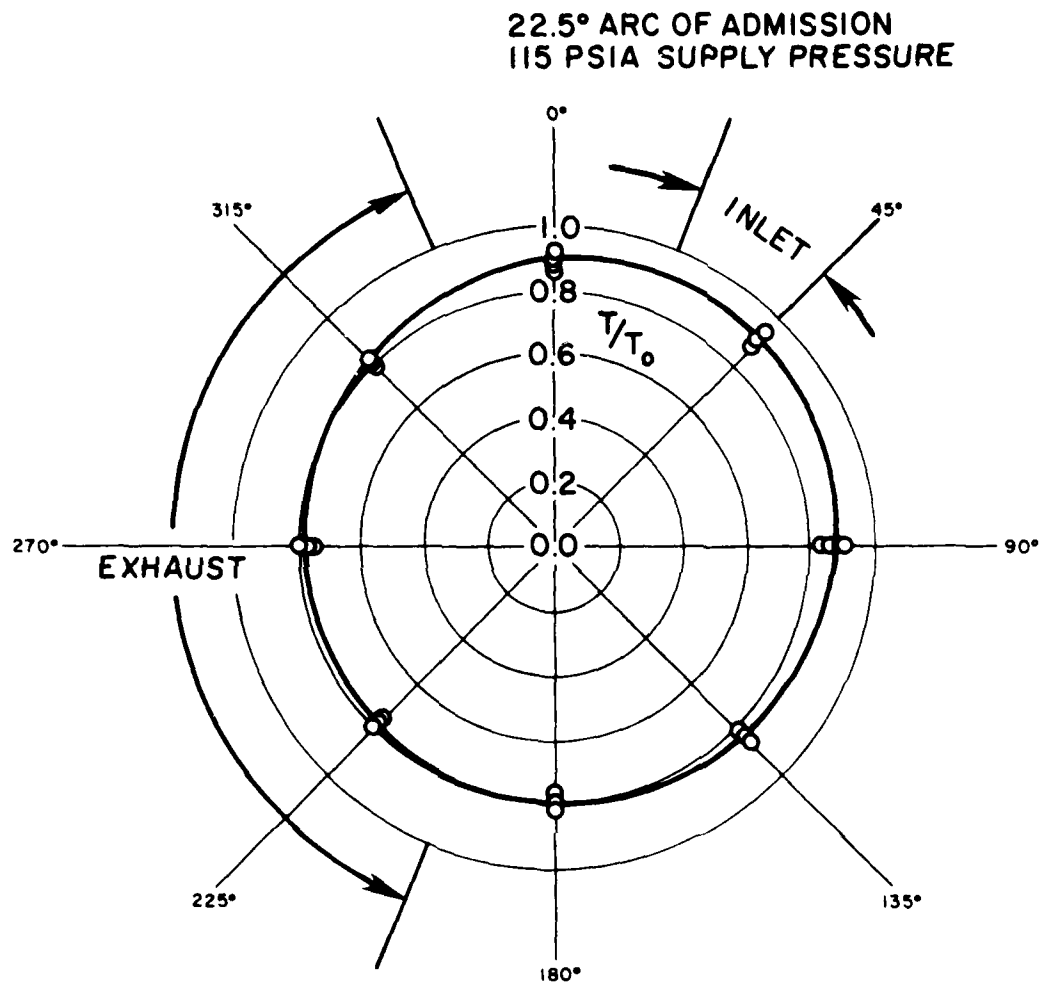


Figure 30. End Plate Temperature Profile Data for 115 psia Supply Pressure 22.5° Arc of Admission

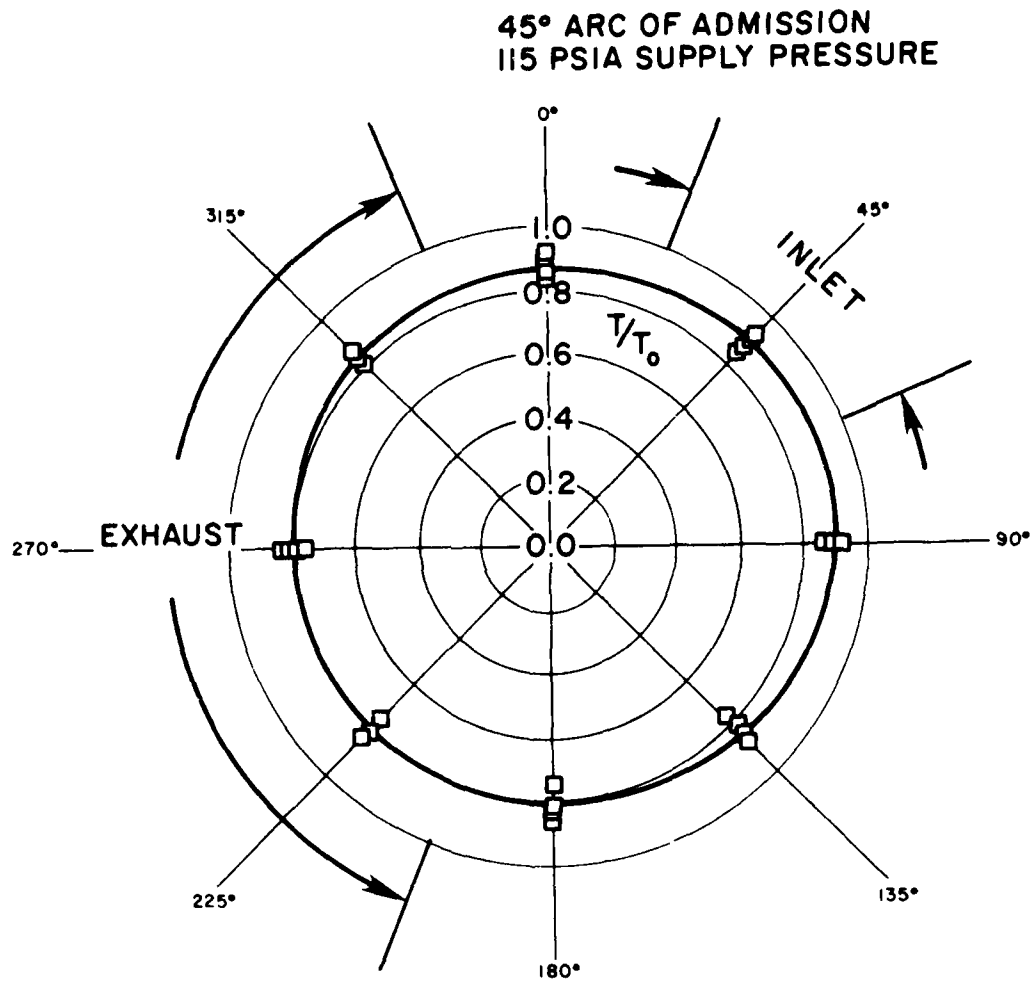


Figure 31. End Plate Temperature Profile Data for 115 psia Supply Pressure 45° Arc of Admission

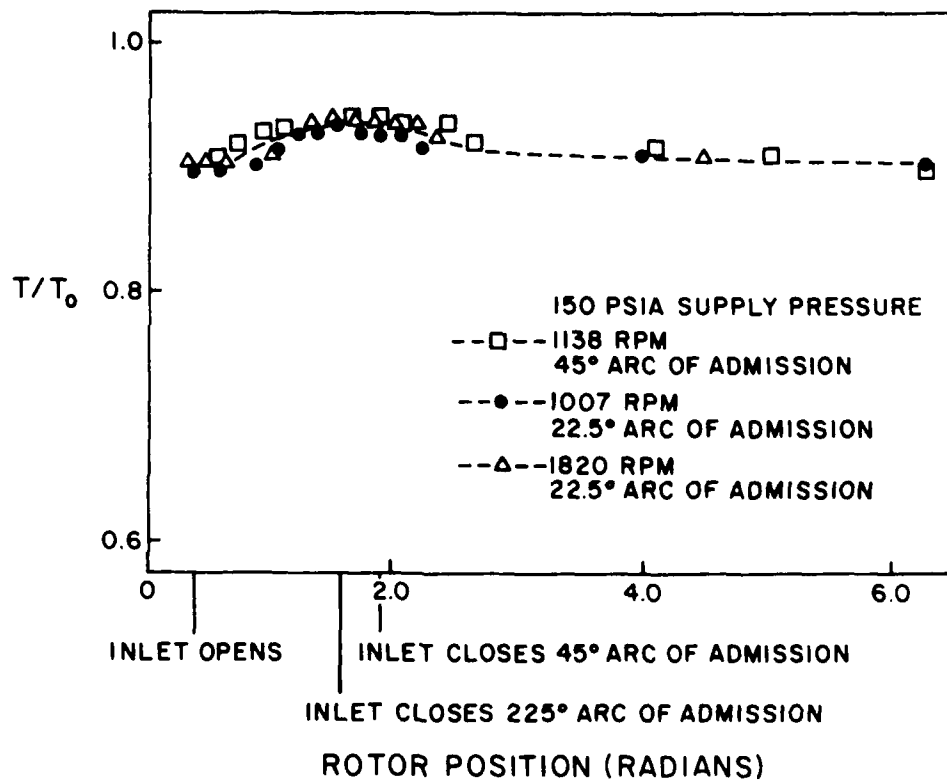


Figure 32. Rotor Surface Temperature Data

TABLE 2

Expander Heat Loss Data

Supply Pressure (psia)	Arc of Admission (Degrees)	Speed (RPM)	Heat Loss ($\frac{\text{BTU}}{\text{hr}}$)
150	22.5	1007	3639
150	22.5	1194	605
150	22.5	1488	3219
115	22.5	1083	4942
115	22.5	1109	3186
115	22.5	1350	4024
115	22.5	1693	4486
150	45	840	6661
150	45	1138	6619
150	45	1369	7188
150	45	1479	4581
150	45	1539	6072
150	45	1906	6359
115	45	895	7481
115	45	1285	4081
115	45	1296	2801
115	45	1477	6028

(1.18 to 2.95 horsepower). This indicates that the heat loss was of the same order of magnitude as the power output. The variations observed in the expander heat loss are believed to be primarily due to the error sustained in measuring the inlet and exhaust enthalpy. An error of 25 BTU/lb_m in determining the inlet and exhaust enthalpy difference results in an error in the heat loss of the order of 4500 BTU/hr. This enthalpy difference of 25 BTU/lb_m is approximately 2% of the inlet enthalpy.

Estimates of the magnitude of the heat loss to the slip ring and pressure transducer cooling adapters were of the same order as the experimentally determined heat losses. This source of energy loss would be eliminated in an operational expander.

4.3 Comparisons with Theoretical Model

4.3.1 Mass Flow Rate. Computation of the mass flow rate depends on the determination of the internal expander clearances. The rotor-end plate and vane-end plate clearances were computed based on the initial cold clearances and the relative thermal expansion of the components.

The cold clearances were determined from micrometer measurements taken during assembly of the expander. The uncertainty in the determination of the cold clearances was estimated to be 0.001 inches.

The thermal expansions were computed using the measured component temperatures. Although the thermal expansions of the components varied with the supply and exhaust temperatures, the variations were small relative to the accuracy of the cold clearance measurements. The rotor-end plate clearance, under operating conditions, was calculated to be 0.003 inches. The vane-end plate clearance was calculated to be 0.005 inches. The larger clearance between the vanes and the end plates was

due to the small coefficient of the thermal expansion of the vanes 2.7×10^{-6} in/in $^{\circ}$ F, compared to 5.6×10^{-6} in/in $^{\circ}$ F for the rotor.

The computed rotor-end plate and vane-end plate clearances were used in the leakage model to compute the leakage flow rate. The vane-end plate clearance was adjusted from 0.005 inches to 0.006 inches due to wear of the carbon vanes and end plates. It also permitted better agreement to be obtained with the experimentally determined leakage flow rates. Adjustment of the clearance by 0.001 inches was felt to be justifiable since the change was within the limits of the cold clearance measurements.

In computing the theoretical leakage flow rates, all leakage paths except those between the end plate and the rotor and the end plate and the vanes were neglected. Figure 33a shows a comparison between the analytically and experimentally determined leakage flow rates for a 22.5 $^{\circ}$ arc of admission and 150 psia supply pressure. The predicted leakage flow rates were 16% below the measured values. It is believed the error is due to the assumption that there was no leakage between the vane tip and the stator. Clearances between the vane and the stator may have occurred as a result of the vane being pushed into its slot by high pressure supply steam. Clearances between the vane and stator may also have occurred due to vane chatter resulting from the stator being rough, or "out of round". It is possible that any vane-stator clearance would result in more leakage from the regions exposed to supply pressure to those control volumes in which the closed expansion process was occurring.

Since vane-stator clearances, resulting from vane chatter, are a function of time and rotor position, a reasonable determination of the

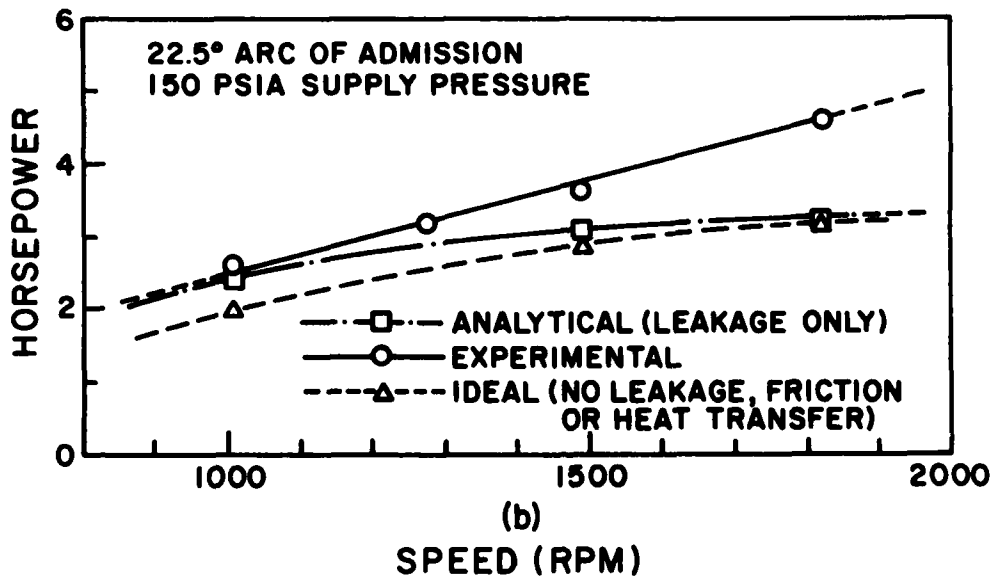
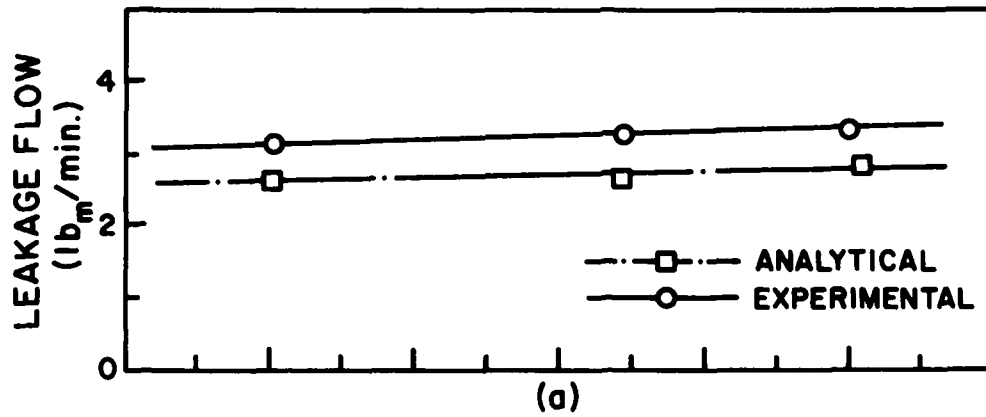


Figure 33a. Leakage Flow Rate Versus Speed

Figure 33b. Horsepower Versus Speed

vane stator clearance was not possible and no attempts were made to include leakage between the vane and stator.

4.3.2 Power Output. The analytically determined leakage flow rates were input into the thermodynamic model to determine the effect of leakage on the expander power output.

Figure 33b shows the experimentally determined indicated power output, the predicted power output with leakage affects included, and the ideal power output. The ideal power output was computed assuming no leakage, heat transfer or friction.

The analytical power output, computed considering only leakage effects, is 7.7% below the measured indicated power at 1007 RPM. This difference increases to 30.4% at 1820 RPM. The difference between the predicted power output and the measured indicated power output is apparently the result of the leakage model not predicting the correct amount of leakage. As previously discussed, the leakage was computed assuming a perfect seal between the vane and the stator. Leakage between the vane and the stator would result in more leakage from those regions at supply pressure to the control volumes undergoing the closed expansion process. Leakage of this nature would result in increased expander power output.

The effect of heat transfer on power was analytically computed by using the theoretically determined heat transfer rates in the thermodynamic model. The theoretical indicated power was computed in the presence of both leakage and heat transfer for a 22.5° arc of admission and 150 psia supply pressure. Heat transfer reduced the theoretical power output by 14%, from 2.40 horsepower to 2.06 horsepower, at 1007 RPM.

At 1820 RPM, heat transfer reduced the power by 13.5%, from 3.25 to 2.81 horsepower.

Comparison between the analytical (leakage and heat transfer included) and experimental indicated power outputs for a 22.5° arc of admission and 150 psia supply pressure shows an error of 20.7% at 1007 RPM and 39% at 1820 RPM. It is felt that the error is predominately the result of the inability to accurately determine the effects of leakage on the expander power output.

Figure 34 shows a comparison between the analytical and experimental frictional power loss for a supply pressure of 150 psia and an arc of admission of 22.5°.

The theoretical and experimental curves are identical within the accuracy of the plot. Good agreement was also obtained for the 45° arc of admission and 150 psia supply steam. At 1479 RPM, and a 45° arc of admission, the experimental frictional power loss was 1.69 horsepower while the theoretical value was 1.71 horsepower. At 1913 RPM, and a 45° arc of admission, the experimental value was 2.26 horsepower and the theoretical value 2.25 horsepower.

The coefficient of friction used in the model, for all surfaces, was 0.075. This value was obtained by inputting the measured steam pressures into the friction model and adjusting the coefficient of friction until the predictions matched the experimental data. The theoretical frictional power loss was computed using the coefficient of friction of 0.075 and the steam pressures computed by the thermodynamic model, with leakage effects included. A test of the validity of the friction model was that a single coefficient of friction allowed accurate

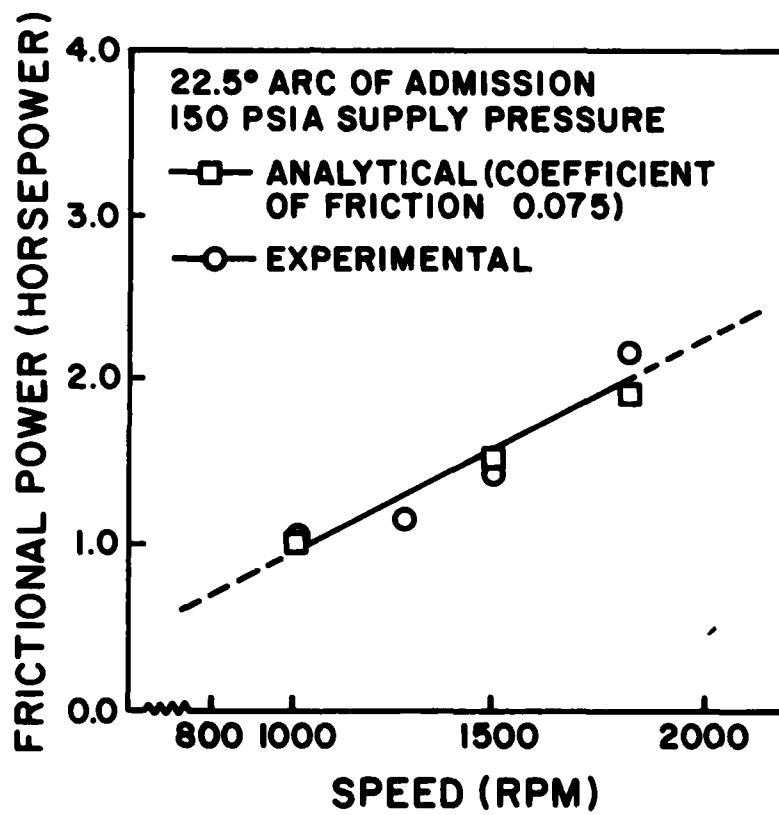


Figure 34. Frictional Power Loss Versus Speed

prediction of the frictional power loss at all speeds and supply conditions except for the 115 psia supply pressure and 22.5° arc of admission case. However, the trends in the power output and efficiency data for this latter case appear to indicate an actual variation in the coefficient of friction.

4.3.3 Temperature Profiles and Heat Transfer Coefficient. A comparison of the experimental and theoretical stator temperature profiles is given in Figure 35. The maximum error is 13%. This error was considered to be reasonably good due to the complex geometry and lack of information regarding the heat transfer coefficient between the steam and the stator.

The experimental and theoretical end plate temperature profiles are compared in Figure 36. The maximum error is 8%.

The measured rotor surface temperature was used as a boundary condition in computing the heat transfer to the rotor. The computed rotor heat transfer was used in conjunction with the measured surface temperature and inlet steam temperature to estimate the heat transfer coefficient between the steam and the rotor. The values obtained are only approximate since at any instant in time the steam temperature is not accurately known. However, at the inlet the steam was assumed to be at the supply temperature. Under this assumption, the computed heat transfer coefficient, at a speed of 1007 RPM, ranged from 610 BTU/hrft²·F when the rotor was initially exposed to the supply steam, to approximately 14,000 BTU/hrft²·F, just before the inlet was closed. The variation in the heat transfer coefficient apparently resulted from the turbulence and steam impingement on the rotor surface. The measured rotor surface

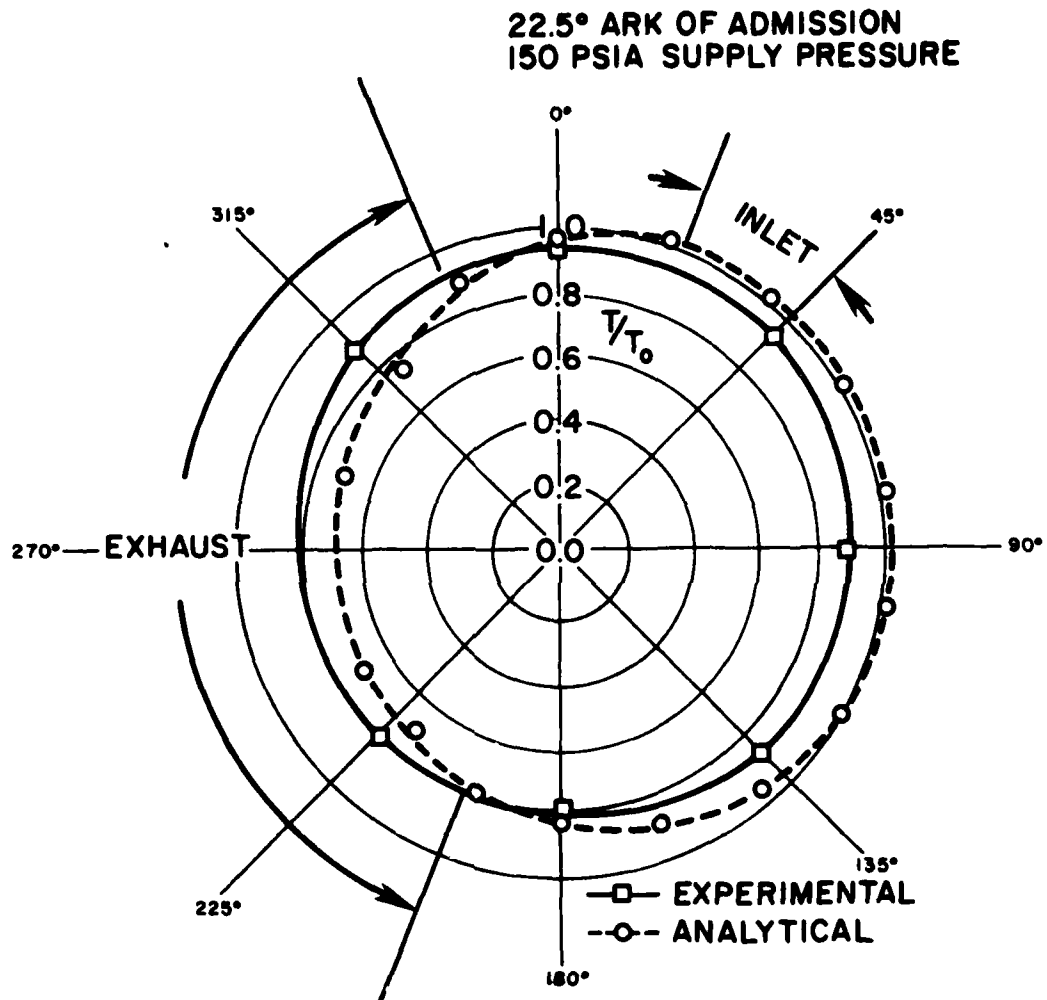


Figure 35. Experimental and Analytical Stator Temperature Profiles 22.5° Arc of Admission

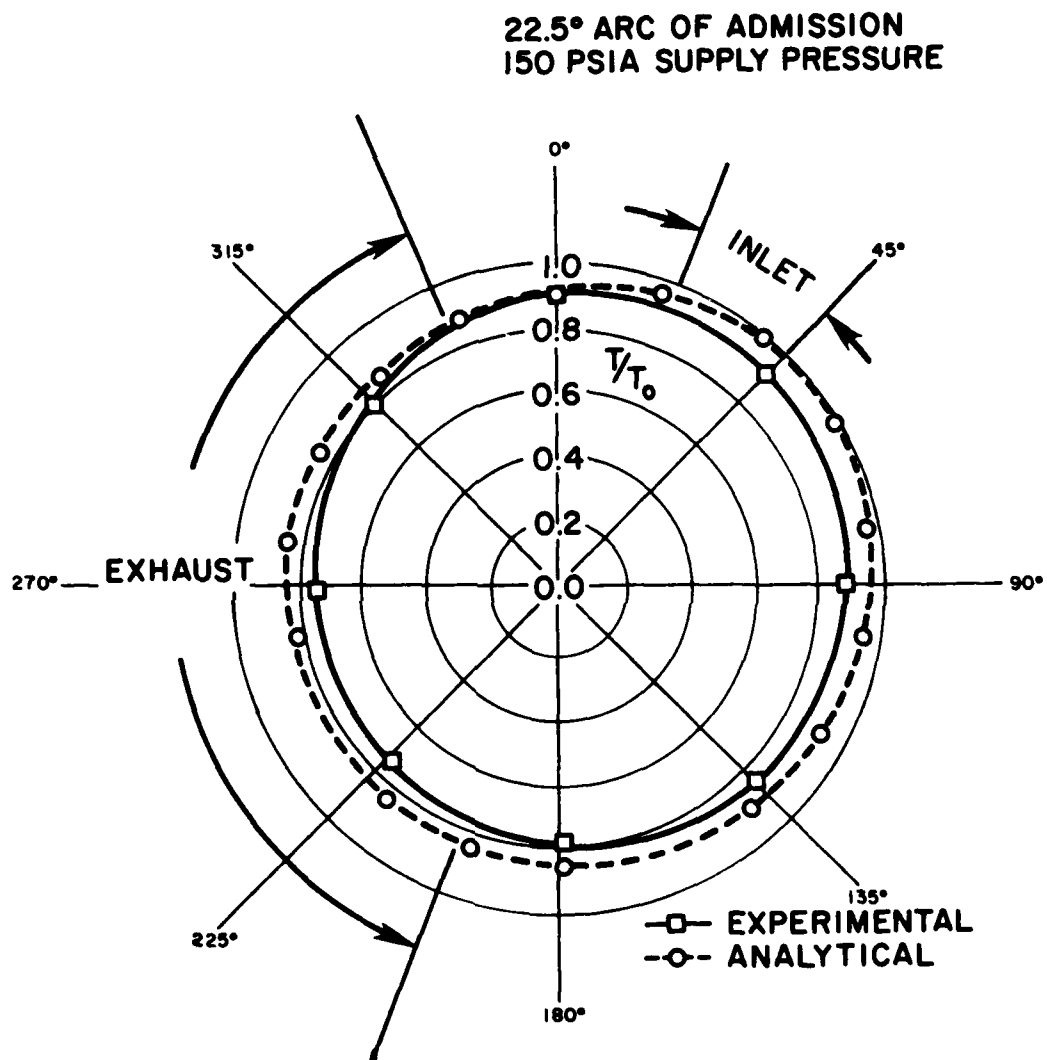


Figure 36. Experimental and Analytical End Plate Temperature Profiles

temperatures used in computing the rotor heat transfer were obtained at the circumferential center of the control volumes. When the rotor surface of a particular control volume is first exposed to the inlet port, the center of the control volume is restricted from seeing the high temperature steam by the small rotor-stator clearance which exists midway between the inlet and exhaust ports. Since the center of the control volume would not be exposed to direct impingement by the supply steam and the turbulence created by the filling process, the calculated heat transfer coefficient would be expected to be low near inlet opening. However, when the center of the control volume becomes exposed to the incoming steam, impingement of the steam on the center of the rotor coupled with turbulence created by the filling process, would cause the heat transfer coefficient to be quite high.

The heat transfer coefficients at the exhaust ranged from 420 BTU/hr ft²°F when the exhaust opened to a maximum of 2800 BTU/hr ft²°F as the exhaust closing was approached. The increase in the heat transfer coefficient during the exhaust process was probably due to an increase in the turbulence of the steam as it was forced out of the control volume by the reduction in the volume of the control volume.

These heat transfer coefficients are only approximate values; however they do provide a starting point for computation of the rotor heat transfer without knowledge of the rotor surface temperature. It should be pointed out that any computation of the instantaneous heat transfer in the expander using the working fluid temperature and a heat transfer coefficient is only a rough approximation. This is due, not only to the uncertainty of the heat transfer coefficient but also to an uncertainty in the knowledge of the instantaneous steam temperature.

Figure 37 illustrates the variation in the ratio of the rotor surface temperature to the steam saturation temperature as a function of rotor position. The data indicate that during a small portion of each revolution, primarily during the filling process, the rotor surface temperature is below the steam saturation temperature. This condition would permit condensation of some steam during filling of the control volume.

An order of magnitude analysis of the degree of condensation can be made by assuming that the amount of steam that could be condensed during the filling process can be approximately written as

$$\Delta m_c = \frac{\bar{h} A_{RS} (T_{SAT} - T_{ROTOR}) \Delta t}{h_{fg}} , \quad (4.1)$$

where \bar{h} is an average convective heat transfer coefficient and h_{fg} is the latent heat of vaporization of the steam. The convective heat transfer coefficient for the condensation process is

$$\bar{h} = k/\delta , \quad (4.2)$$

where k is the thermal conductivity of liquid water and δ is the thickness of the condensed liquid film.

From geometric considerations, the amount of liquid condensed during the filling process can be approximately written as

$$\Delta m_c = \rho_w \delta (R_f \Delta \theta Z) , \quad (4.3)$$

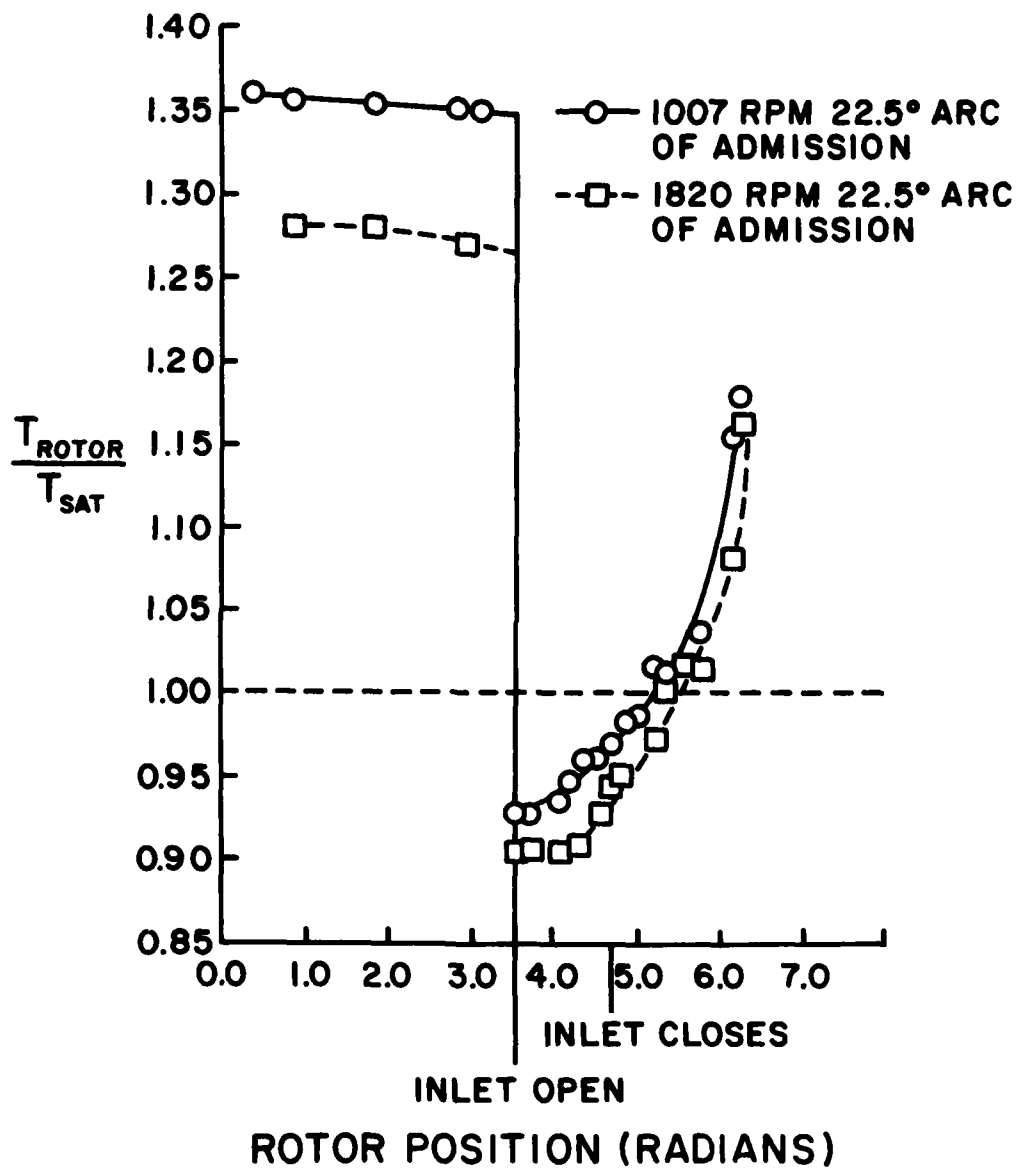


Figure 37. Ratio of Rotor Surface Temperature to Steam Saturation Temperature Data

where $(R_1 \Delta \theta Z)$ is the rotor surface area of one control volume. Equating Equations (4.1) and (4.3) and using Equation (4.2) gives

$$\frac{\bar{h}(R_1 \Delta \theta Z)(T_{SAT} - T_{ROTOR})\Delta t}{h_{fg}} = \rho_{\omega} \frac{k}{\bar{h}} (R_1 \Delta \theta Z) \quad (4.4)$$

Solving Equation (4.4) for \bar{h} and substitution of \bar{h} into Equation (4.1) permits an estimate of the amount of steam condensed in each control volume during the filling process. The approximate mass flow rate of condensed steam is

$$\dot{m}_c = \frac{\bar{h} A_{RS} (T_{SAT} - T_{ROTOR})\Delta t}{h_{fg}} \times \frac{8 \text{ CONTROL VOLUMES}}{\text{REVOLUTION}} \times \frac{N \text{ REVOLUTIONS}}{\text{MINUTE}} \quad (4.5)$$

Based on this calculation, condensation rates of 0.279 lb_m/min at 1820 RPM and 0.207 lb_m/min at 1007 RPM have been calculated.

The heat transfer coefficients required to condense the steam are 25,789 BTU/hr ft²°F at 1820 RPM and 19,209 BTU/hr ft²°F at 1007 RPM. Lower heat transfer coefficients would result in less condensation, at a particular speed, due to insufficient time to condense the steam. The rotor heat transfer coefficients computed from the rotor heat transfer analysis, at 1007 RPM, have a minimum value at the inlet of 610 BTU/hr ft²°F and a maximum of 14,000 BTU/hr ft²°F. Since these values are less than that computed by Equation (4.4), the actual amount of steam condensed on the rotor would be less than the calculated values.

It is believed that condensation on the stator and the end plates would be less than on the rotor since the surfaces of these components do not see the relatively cold exhaust steam as long as the rotor surface

does. No stator or end plate surface temperatures were measured. The measured end plate and stator temperatures at 0.065 inches below the surface are slightly less than the supply temperature at the inlet. However, the temperature at the surface of these components would be higher due to convection from the supply steam and frictional heat generation at the surface.

Since the predicted condensation rates are less than 10% of the difference between the measured flow rate and the ideal flow rate, it can be concluded that the difference was primarily due to leakage. It can also be concluded that the difference between the predicted power output (computed with leakage affects only) and the experimentally determined indicated power shown in Figure 33b is not due to condensation and re-evaporation. The estimated condensation rate is not of sufficient magnitude to cause the difference.

CHAPTER V

SUMMARY AND CONCLUSIONS

5.1 Summary

A commercially available air expander modified to operate on steam was tested using 150 psia and 115 psia supply steam. The speed was varied from 840 to 1913 RPM. Under these operating conditions, the power output ranged from 0.5 horsepower to 2.85 horsepower. Mechanical efficiencies ranged from 65% to 40%. The experimentally determined adiabatic expansion efficiencies varied from 9.5% at the low speeds to 20% at the high speeds. Leakage flow rates, ranging from 2.40 lb_m/min to 3.90 lb_m/min, were obtained. The leakage flow increased with increased arc of admission and supply pressure. The total mass flow of the expander varied from 3.1 lb_m/min to 5.8 lb_m/min.

The expander was analytically modeled to permit the determination of the expander performance and operating component temperatures.

The models predicted the frictional power loss very well. The leakage flow rates were predicted with an error of 16%. The heat transfer models predicted the stator and end plate temperature profiles with an accuracy on the order of 10%. Indicated power predictions were computed with errors ranging from 20.7% at the low speeds to 39% at the high speeds.

5.2 Conclusions

1) The adiabatic expansion efficiency is severely reduced by friction and leakage. Figures 16 and 17 show that friction reduced the power output and hence, the efficiency of the expander by 40% - 50%. Leakage reduced the efficiency on the order of 55% - 60%. Analytically, it was determined that heat transfer reduced the efficiency approximately 10% - 20%.

2) Figures 18 through 21 show that the leakage flow varies only slightly with speed but the ideal flow increases with speed. Therefore, it can be seen from Equation (4.1) that the reduction in adiabatic expansion efficiency due to leakage is decreased at higher speeds.

3) The frictional power loss is proportional to speed. As the speed increases, friction tends to increasingly reduce the efficiency.

4) The frictional power loss can be predicted very well, as shown in Figure 34. However, the predictions are dependent on a knowledge of the coefficient of friction.

5) The magnitude of the leakage flow rates can be predicted reasonably well by the model. However, prediction of the correct amount of leakage depends on a knowledge of the leakage paths and the actual operating clearances. This information is difficult to obtain in practice.

6) The accuracy of the predicted power output is reduced by severe amounts of leakage as a result of a lack of information regarding the leakage paths.

The purpose of this study was not to develop an efficient vane expander, but to obtain an understanding of the phenomena occurring within the expander. However, the information gained provides a basis

for designing a vane expander with projected efficiencies 50% to 100% greater than those measured in the experimental version.

The frictional power loss can be reduced by decreasing the normal forces at the vane-rotor and vane-stator contact points. Supply of the steam through a port in the end plate or through the rotor, at the vane base, may prevent the vane from being pushed into the vane slot by incoming steam. This would permit a decrease in the spring force at the base of the vanes with a concomitant decrease in the vane-stator contact force.

Frictional power losses can also be decreased by reducing the friction coefficient. Injection of oil around the periphery of the stator would increase the probability of obtaining a hydrodynamic film between the vanes and the stator, resulting in a decrease in the coefficient of friction. An increase in the oil flow rate may result in a decrease of the friction coefficient, but it would also result in more contamination of the steam. There may also be other material combinations with lower coefficients of friction in the presence of steam and oil.

Leakage in the expander could be reduced by matching the coefficients of thermal expansion of the expander components. This would result in lower operating clearances than were obtained in the test expander. Elimination of the thin liner which is susceptible to distortion could reduce leakage between the vane and the stator.

Heat transfer from the expander could be significantly reduced by elimination of the pressure transducer and slip ring cooling adapters installed in the test expander. Total heat losses could probably be

reduced from the same order of magnitude as the shaft power to 10% or less of the shaft power.

BIBLIOGRAPHY

1. Wolgemuth, C. H. and Olson, D. R., "A Study of Breathing in Vane Type Expanders," Proceedings of the Sixth IECEC, Boston, Massachusetts, August 3-5, 1971, published by SAE.
2. Edwards, T. C. and McDonald, A. T., "Analysis of Mechanical Friction in Rotary Vane Machines," Purdue Compressor Technology Conference Proceedings, July 25-27, 1972.
3. Peterson, C. R. and McGahan, W. A., "Thermodynamic and Aerodynamic Analysis Methods for Oil Flooded Sliding Vane Compressors," Purdue Compressor Technology Conference Proceedings, July 25-27, 1972.
4. Echard, J. E., "Multi-Vane Expander as Prime Mover in Low Temperature Solar or Waste Heat Applications," Record of the Tenth IECEC, Newark, Delaware, August 18-22, 1975, published by IEEE.
5. Syniuta, W. D. and Palmer, R. M., "Design Features and Initial Performance Data on an Automotive Steam Engine. Part II. Reciprocating Steam Expander-Design Features and Performance," 1974 SAE Transactions.
6. Bendersky, D., "A Special Thermocouple for Measuring Transient Temperatures," Mechanical Engineering, Vol. 75, 1953, p. 117.
7. Fox, L., Numerical Solution of Ordinary and Partial Differential Equations, Pergamon Press, New York, New York, 1962, p. 33-34, 289-291.
8. Bech, W. D., Stein, R. A. and Eibling, J. A., "Design for Minimum Friction in Rotary-Vane Refrigeration Compressors," ASHRAE Transactions, Vol. 72, Part 1, 1966, p. 190-197.
9. Blackburn, J. F., Reethof, G., Shearer, J. L., Fluid Power Control, The MIT Press, 1960, p. 102-103.
10. Holman, J. P., Heat Transfer, Second Edition, McGraw Hill Book Company, New York, New York, 1968, p. 134-139.
11. Schmidt, F. W., Numerical Solutions in Heat Transfer and Fluid Mechanics, Copyright 1968 (unpublished), p. 5-7-5-12.
12. Karplus, W. J., "An Electric Circuit Theory Approach to Finite Difference Stability," AIEE Transactions, 77, Part 1, 1958, p. 210.

13. Schneider, P. J., Conduction Heat Transfer, Addison Wesley Publishing Company Incorporated, 1955, p. 153, 298.
14. Keenan, J. H. and Keyes, F. G., Thermodynamic Properties of Steam, John Wiley and Sons, 1967.
15. Schnachel, H. C., "Formulations for the Thermodynamic Properties of Steam and Water," ASME Transactions, 80, 1958, p. 959-966.
16. Steltz, W. G. and Silvestri, G. J., "The Formation of Steam Properties for Digital Computer Application," ASME Transactions, 80, 1958, p. 967-973.
17. Selby, M. S. and Gerling, B., Standard Mathematical Tables, 14th Edition, The Chemical Rubber Company, 1965, p. 365.

APPENDIX A

EQUATIONS USED IN THERMODYNAMIC MODEL

The ordinary differential equations, used in the thermodynamic model, for the pressure, mass and in the super-heated region, temperature of the working fluid were the same as those given by Wolgemuth and Olson in Reference 1. They will be listed here in dimensionless form.

Conservation of mass for the control volume shown in Figure 38 (volume between adjacent vanes plus the volume of the pressurization ports and the volume of the trailing vane slot underneath the vane) shows that

$$\dot{M}^* = \dot{m}_1^* - \dot{m}_2^* \quad (\text{A.1})$$

where the subscript (1) indicates "in" and the subscript (2) indicates "out". The superscript (*) indicates a dimensionless variable. The dimensionless variables are defined in terms of the dimensional variables in Table 3. For the inlet and exhaust ports

$$\dot{m}_{1 \text{ or } 2}^* = \frac{BA^*}{(v/v_o)} \sqrt{\frac{\Delta h_c}{h_o}} \quad (\text{A.2})$$

where B, the breathing number is defined as

$$B = \frac{60 C_D A_{MAX} 223.8 \sqrt{h_o}}{2\pi N Z R_o^2} \quad (\text{A.3})$$

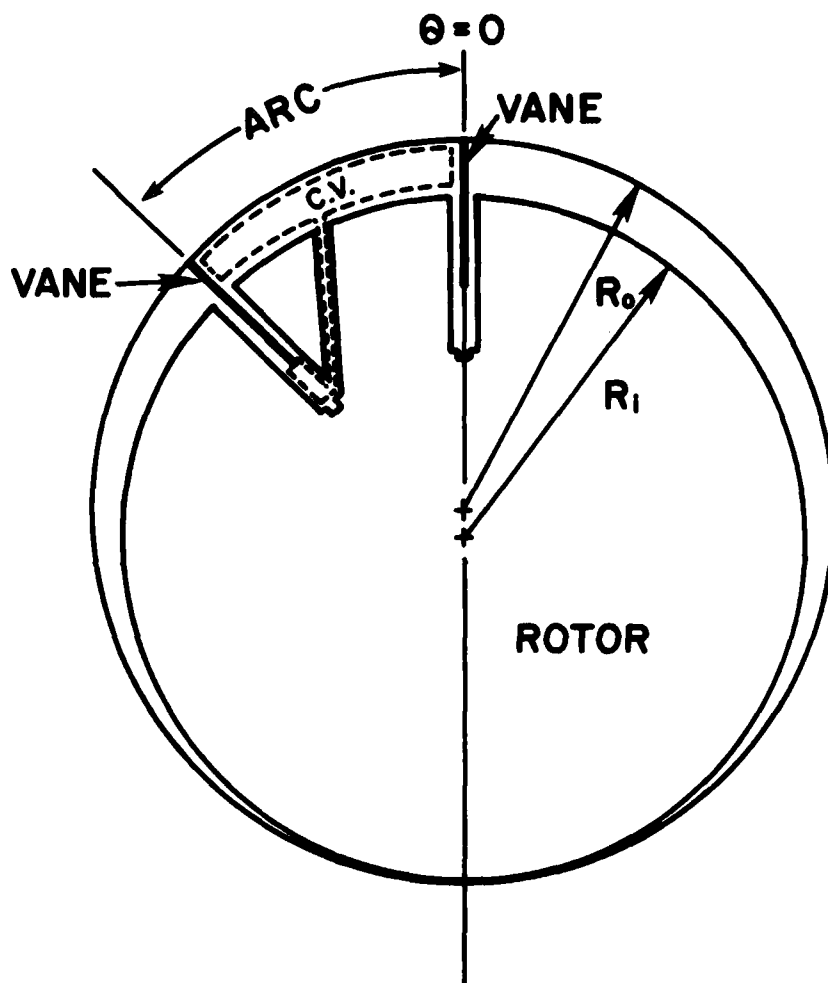


Figure 38. Schematic Diagram Showing Control Volume

TABLE 3

Definitions of Non-Dimensional Variables

$$\theta = \frac{2\pi N}{60} t$$

$$V^* = \frac{V}{(R_o^2 Z)}$$

$$P^* = \frac{P}{P_o}$$

$$T^* = \frac{T}{T_o}$$

$$M^* = \frac{M}{Z R_o^2 / v_o} = \frac{V}{v} \frac{v_o}{Z R_o^2} = V^* \left(\frac{v_o}{v} \right)$$

$$\dot{m}^* = \left(\frac{60 v_o}{2\pi N Z R_o^2} \right) \dot{m}$$

$$R^* = \frac{R_1}{R_o}$$

$$A^* = \frac{A}{A_{MAX}}$$

$$\dot{Q}^* = \frac{v_o 60}{Z R_o^2 2\pi N h_o} \dot{Q}$$

$$W^* = \frac{W}{P_o Z R_o^2}$$

and

$$A_{MAX} = \frac{2\pi R_o Z_{PORT}}{\text{NUMBER OF VANES}} \quad (A.3a)$$

The variation of A^* with time is shown in Figure 39 for the exhaust port, and for the inlet port when the arc of admission is greater than the arc (angle between adjacent vanes). Figure 40 shows the variation in A^* for the inlet port when the arc of admission is less than arc.

For the superheated region, the differential equation for the dimensionless pressure is

$$\dot{P}^* = \frac{\dot{Q}^* + [\dot{m}_1^* - \dot{m}_2^* \frac{h}{h_o} - \dot{M}^* \frac{h}{h_o}] - \left(\frac{AD}{h_o}\right) M^* \left(\frac{\partial h}{\partial T}\right)_P}{M^* \left[\left(\frac{\partial h}{\partial P}\right)_T + AB \left(\frac{\partial h}{\partial T}\right)_P - v_o \frac{v^*}{M^*} \left(\frac{144 \times 14.6959}{778}\right) \right]} \frac{P_o}{14.6959 h_o} \quad (A.4)$$

where

$$AD = \frac{\dot{V}^* - \dot{M}^* \left(\frac{v}{v_o}\right)}{\frac{0.0160185}{v_o} M^* \left(\frac{4.55504}{P} + \left(\frac{\partial b'}{\partial T}\right)_P\right)} \quad (A.5)$$

and

$$AB = \frac{\frac{4.55504T}{P^2} - \left(\frac{\partial b'}{\partial P}\right)_T}{\frac{4.55504}{P} + \left(\frac{\partial b'}{\partial T}\right)_P} \quad (A.6)$$

Based on the Keenan and Keyes [14] equation of state for steam

$$v = 0.0160185(4.55504 T/P + b') \quad (A.7)$$

the dimensionless temperature in the superheated region is computed by integrating

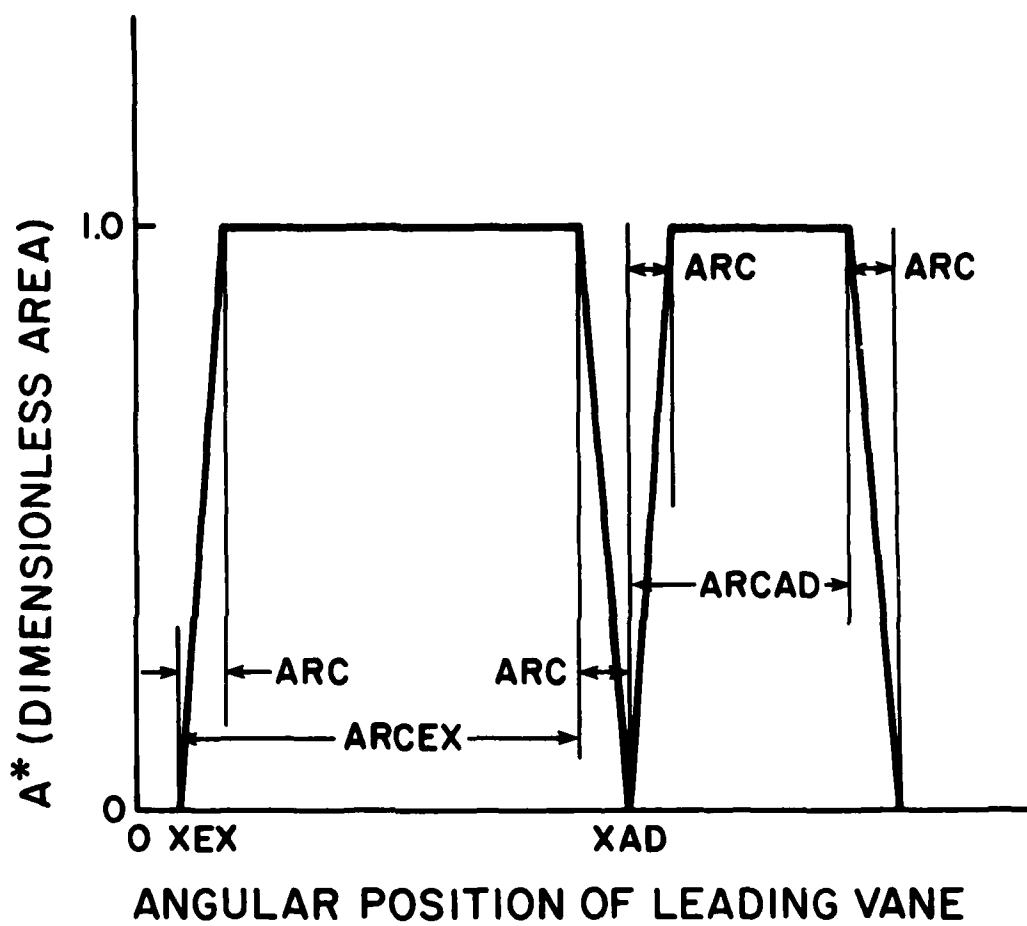


Figure 39. Variation of Exhaust and Intake Area for Arc of Admission and Arc of Exhaust Greater than Arc

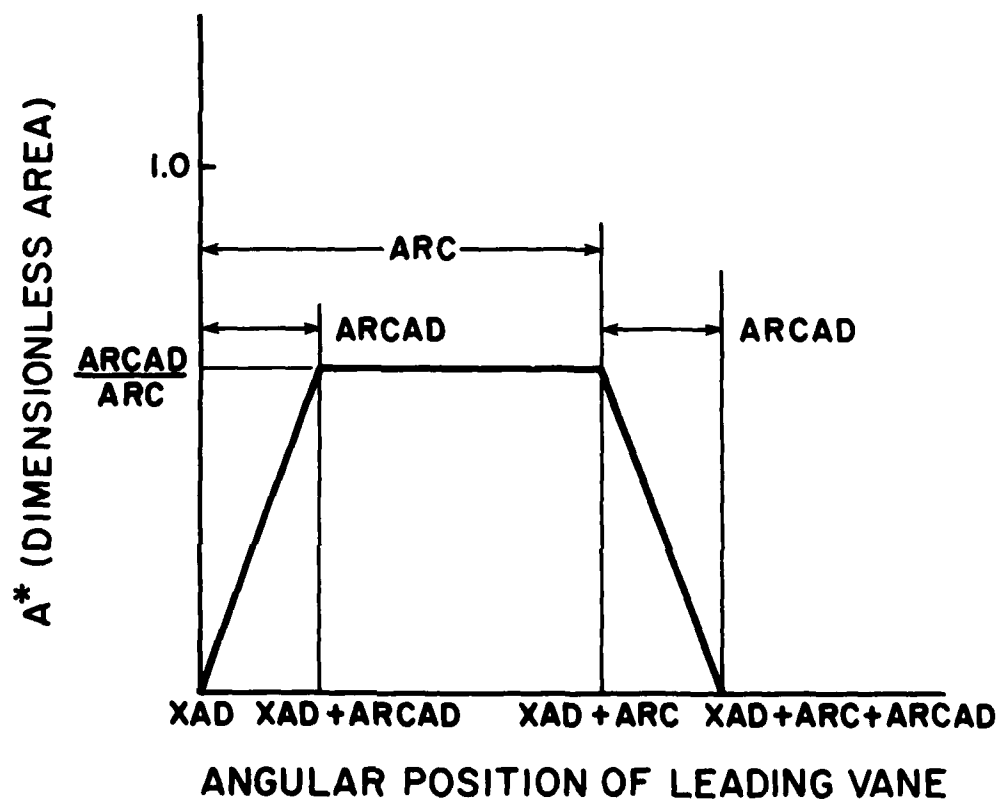


Figure 40. Variation of Intake Area for Arc of Admission less than Arc

$$\dot{T}^* = 1.8 \frac{AD}{T_o} + \frac{P_o}{T_o} (AB) \left(\frac{1.8}{146959} \right) \dot{P}^* \quad (A.8)$$

In the two-phase region, the \dot{P}^* equation is

$$\dot{P}^* = \frac{[\dot{Q}^* + \dot{m}_1^* - \dot{m}_2^* \frac{h}{h_o} - M^* \frac{h}{h_o} - \frac{h_{fg}}{v_{fg} h_o} (v_o \dot{V}^* - vM^*)]}{M^* [AC - v_o \frac{V^*}{M^*} \frac{144}{778}] \frac{P_o}{h_o}} \quad (A.9)$$

where

$$AC = (1 - x) \frac{d_{hf}}{dP} + x \frac{d_{hg}}{dP} - \frac{h_{fg}}{U_{fg}} \left[(1 - x) \frac{dU_f}{dP} + x \frac{dU_g}{dP} \right] \quad (A.10)$$

Since P and T are not independent in the two-phase region, an expression for \dot{T}^* is not needed in that region.

The differential equation for the volume of the control volume employed in Reference 1 was modified to account for the changing volume in the trailing vane slot.

For the vane slot and pressurization ports in Figure 41, the volume is

$$V_{SL} = SW \cdot Z \cdot (SD - LV + HR) + VH + VOP \quad (A.11)$$

where

$$HR = -R_1 + e \cos(\theta - ARC) + R_o \left[1 - \frac{e^2}{R_o^2} \sin^2(\theta - ARC) \right]^{1/2} \quad (A.12)$$

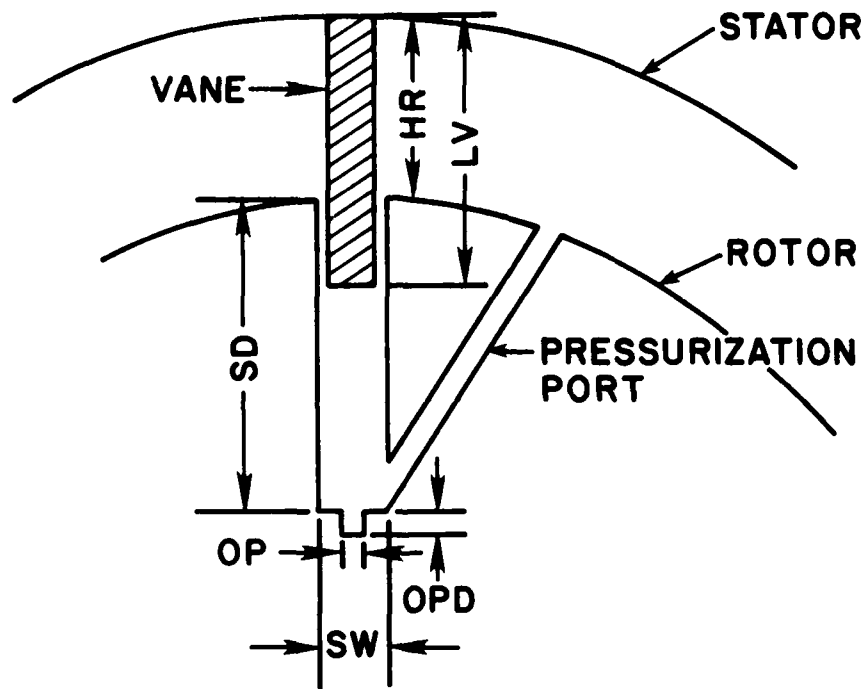


Figure 41. Schematic of Vane Slot and Pressure Balancing or Pressurization Port

is the angular position of the leading vane, VH is the volume of the pressurization ports and VOP is the volume of the groove at the base of the vane slot. Since

$$V_{SL}^* = V_{SL} / ZR_o^2, \quad (A.13)$$

then

$$\dot{V}_{SL}^* = \frac{dV^*}{d\theta} = \frac{dV^*}{dV} \frac{dV}{d\theta} = \frac{SW}{R_o^2} \frac{dHR}{d\theta}, \quad (A.14)$$

or

$$\dot{V}_{SL}^* = \frac{SW}{R_o^2} \left[-e \sin(\theta - ARC) - \frac{e^2}{R_o} \sin(\theta - ARC) \cos(\theta - ARC) \left[1 - \frac{e^2}{R_o^2} \sin^2(\theta - ARC) \right]^{-1/2} \right]. \quad (A.15)$$

Therefore, the differential equation for the dimensionless volume becomes

$$\begin{aligned} \dot{V}^* = & (1 - R')^2 \cos^2 \theta + (1 - R') \cos \theta \sqrt{1 - (1 - R')^2 \sin^2 \theta} - (1 - R')^2 \\ & \cos^2(\theta - ARC) - (1 - R') \cos(\theta - ARC) \sqrt{1 - (1 - R')^2 \sin^2(\theta - ARC)} \\ & + \dot{V}_{SL}^*, \end{aligned} \quad (A.16)$$

where $R' = R_1 / R_o$.

The dimensionless volume of the control volume at the position when $\theta = 0$ (the initial volume) is

$$\begin{aligned}
 VI^* = \frac{1}{R_o^2} & \left[\left(\frac{R_o^2 - R_1^2}{2} \right) \text{ARC} + \frac{e^2}{4} \sin(2 \text{ARC}) + \frac{R_o}{2} e \sin \text{ARC} \left(1 - \frac{e^2}{R_o^2} \sin^2 \right. \right. \\
 & \left. \left. \text{ARC} \right)^{1/2} + \frac{R_o^2}{2} \sin^{-1} \frac{e}{R_o} \sin \text{ARC} + \text{SW}(\text{SD} - \text{LV} + \text{HR}) \right]_{\theta = \frac{7\pi}{4}} \\
 & + (\text{OP})(\text{OPD}) \quad . \quad \quad \quad (\text{A.17})
 \end{aligned}$$

The differential equation for the dimensionless power is

$$\dot{W}^* = P^* \dot{V}^* \quad . \quad \quad \quad (\text{A.18})$$

In the superheated region, Equations (A.1), (A.4), (A.8), (A.16) and (A.18) were integrated on the digital computer using the IBM 360 Scientific Subroutine Package (360A-CM-03x) version III subroutine DHPCG. Subroutine DHPCG uses the modified Hamming's Predictor Corrector method [7].

In the two phase region, Equations (A.1), (A.9), (A.16), and (A.18) were integrated on the digital computer using subroutine DHPCG.

The solution of the equations was started at $\theta = 0$ with initial guesses for working fluid properties in the control volume and the dimensionless work initialized at $W^* = 0$. The equations were integrated through one revolution and the final values of the properties used as initial values for the next revolution. The process continued until the initial and final property values were the same.

In the two phase region, the steam thermodynamic properties and their derivatives were read into the computer as tabular data. The properties and their derivatives were obtained from Reference 14. A

three point interpolation scheme gave good values of the properties and their derivatives from the tabular data.

In the superheated region, the steam thermodynamic properties were obtained from PSU IBM 360 computer subroutines based on References 14, 15, and 16. The partial derivatives of "b'" and the enthalpy which appear in Equations (A.4) through (A.7) were evaluated from analytic expressions resulting from differentiating the expressions for the enthalpy and "b'" given in Reference 15 and 16.

APPENDIX B

DERIVATION OF EXPRESSIONS FOR TANGENTIAL AND NORMAL ACCELERATIONS

The tangential acceleration of the vane center of gravity may be written as:

$$A_{CG\ t} = A_{p\ t} + A_{CG/p\ t} + A_{CORIOLIS\ t} \quad (B.1)$$

The magnitude of the tangential acceleration of a point $P(A_{p\ t})$ on a frame moving with the rotor at a radius coinciding with the radius of the vane center of gravity is in general

$$A_{p\ t} = r \alpha'_{ROTOR} \quad (B.2)$$

However, at steady state, the speed of the rotor is constant and the angular acceleration (α'_{ROTOR}) is zero. It has been assumed that the acceleration of the vane relative to the moving frame, in the tangential direction, $A_{CG/p\ t}$ is zero. Therefore, Equation (B.1) reduces to

$$A_{CG\ t} = A_{CORIOLIS\ t} = 2\vec{\Omega} \times \vec{V}_{CG/P} \quad (B.3)$$

Figure 3.1 indicates that the distance HR describes the position of the blade tip relative to the rotor. From Reference 1

$$HR = -R_1 + e \cos \theta + R_0 \left(1 - \frac{e^2}{R_0^2} \sin^2 \theta\right)^{1/2} \quad (\text{B.4})$$

where R_1 is the radius of the rotor, R_0 is the radius of the stator and $e = R_0 - R_1$ is the eccentricity. Therefore,

$$V_{CG/P} = \frac{dHR}{dt} = \frac{dHR}{d\theta} \frac{d\theta}{dt} \quad (\text{B.5})$$

or

$$V_{CG/P} = \left| 2\pi N \left[-e \sin \theta - \frac{e^2}{R_0} \sin \theta \cos \theta \left(1 - \frac{e^2}{R_0^2} \sin^2 \theta\right)^{-1/2} \right] \right|. \quad (\text{B.6})$$

The velocity $V_{CG/P}$ is in the radial direction. Hence, the resulting expression for the magnitude of the tangential acceleration of the vane is:

$$A_{CG t} = \left| 2(2\pi N)^2 \left[-e \sin \theta - \frac{e^2}{R_0} \sin \theta \cos \theta \left(1 - \frac{e^2}{R_0^2} \sin^2 \theta\right)^{-1/2} \right] \right|. \quad (\text{B.7})$$

The direction of $A_{CG t}$ is found by rotating the vector $V_{CG/P}$ 90° in the sense of rotation of the rotor.

The normal acceleration of the vane is

$$A_{CG n} = A_{p n} + A_{CG/p n} \quad (\text{B.8})$$

The magnitude of the normal acceleration ($A_{p n}$) of a point, on a frame moving with the rotor, at a radius corresponding to the radius of the vane center of gravity is

$$A_{p n} = r\omega^2 . \quad (B.9)$$

This acceleration is always directed toward the center of the rotor. The magnitude of the acceleration of the vane relative to the moving frame ($A_{CG/p n}$) is obtained by differentiating Equation (B.6) with respect to time. Therefore,

$$A_{CG/p n} = \left| (2\pi N)^2 \left[-e \cos \theta - \frac{e^2}{R_o} \cos 2\theta \left(1 - \frac{e^2}{R_o^2} \sin^2 \theta \right)^{-1/2} - \frac{1}{4} \frac{e^4}{R_o^3} \sin^2 2\theta \left(1 - \frac{e^2}{R_o^2} \sin^2 \theta \right)^{-3/2} \right] \right| . \quad (B.10)$$

Vector addition of the quantities in Equation (B.9) and (B.10) gives the normal acceleration of the vane.

APPENDIX C

DERIVATION OF FINITE DIFFERENCE EXPRESSIONS

The transformation of the three dimensional Laplacian

$$\nabla^2 T = \frac{\partial^2 T}{\partial r^2} + \frac{1}{r} \frac{\partial T}{\partial r} + \frac{1}{r^2} \frac{\partial^2 T}{\partial \theta^2} + \frac{\partial^2 T}{\partial z^2} \quad (C.1)$$

into finite difference form was accomplished by the method of Taylor's Series expansion [11,13].

For interior nodes, as shown in Figure 42, the following Taylor's Series expansions were written about the point i,j,k

$$T_{i-1,j,k} = T_{i,j,k} - \Delta\theta \left. \frac{\partial T}{\partial \theta} \right|_{i,j,k} + \frac{\Delta\theta^2}{2!} \left. \frac{\partial^2 T}{\partial \theta^2} \right|_{i,j,k} - \frac{\Delta\theta^3}{3!} \left. \frac{\partial^3 T}{\partial \theta^3} \right|_{i,j,k} + \dots \quad (C.2)$$

$$T_{i+1,j,k} = T_{i,j,k} + \Delta\theta \left. \frac{\partial T}{\partial \theta} \right|_{i,j,k} + \frac{\Delta\theta^2}{2!} \left. \frac{\partial^2 T}{\partial \theta^2} \right|_{i,j,k} + \frac{\Delta\theta^3}{3!} \left. \frac{\partial^3 T}{\partial \theta^3} \right|_{i,j,k} + \dots \quad (C.3)$$

$$T_{i,j+1,k} = T_{i,j,k} + \Delta r \left. \frac{\partial T}{\partial r} \right|_{i,j,k} + \frac{\Delta r^2}{2!} \left. \frac{\partial^2 T}{\partial r^2} \right|_{i,j,k} + \frac{\Delta r^3}{3!} \left. \frac{\partial^3 T}{\partial r^3} \right|_{i,j,k} + \dots \quad (C.4)$$

$$T_{i,j-1,k} = T_{i,j,k} - \Delta r \left. \frac{\partial T}{\partial r} \right|_{i,j,k} + \frac{\Delta r^2}{2!} \left. \frac{\partial^2 T}{\partial r^2} \right|_{i,j,k} - \frac{\Delta r^3}{3!} \left. \frac{\partial^3 T}{\partial r^3} \right|_{i,j,k} + \dots \quad (C.5)$$

$$T_{i,j,k-1} = T_{i,j,k} - \Delta z \left. \frac{\partial T}{\partial z} \right|_{i,j,k} + \frac{\Delta z^2}{2!} \left. \frac{\partial^2 T}{\partial z^2} \right|_{i,j,k} - \frac{\Delta z^3}{3!} \left. \frac{\partial^3 T}{\partial z^3} \right|_{i,j,k} + \dots \quad (C.6)$$

$$T_{i,j,k+1} = T_{i,j,k} + \Delta z \left. \frac{\partial T}{\partial z} \right|_{i,j,k} + \frac{\Delta z^2}{2!} \left. \frac{\partial^2 T}{\partial z^2} \right|_{i,j,k} + \frac{\Delta z^3}{3!} \left. \frac{\partial^3 T}{\partial z^3} \right|_{i,j,k} + \dots \quad (C.7)$$

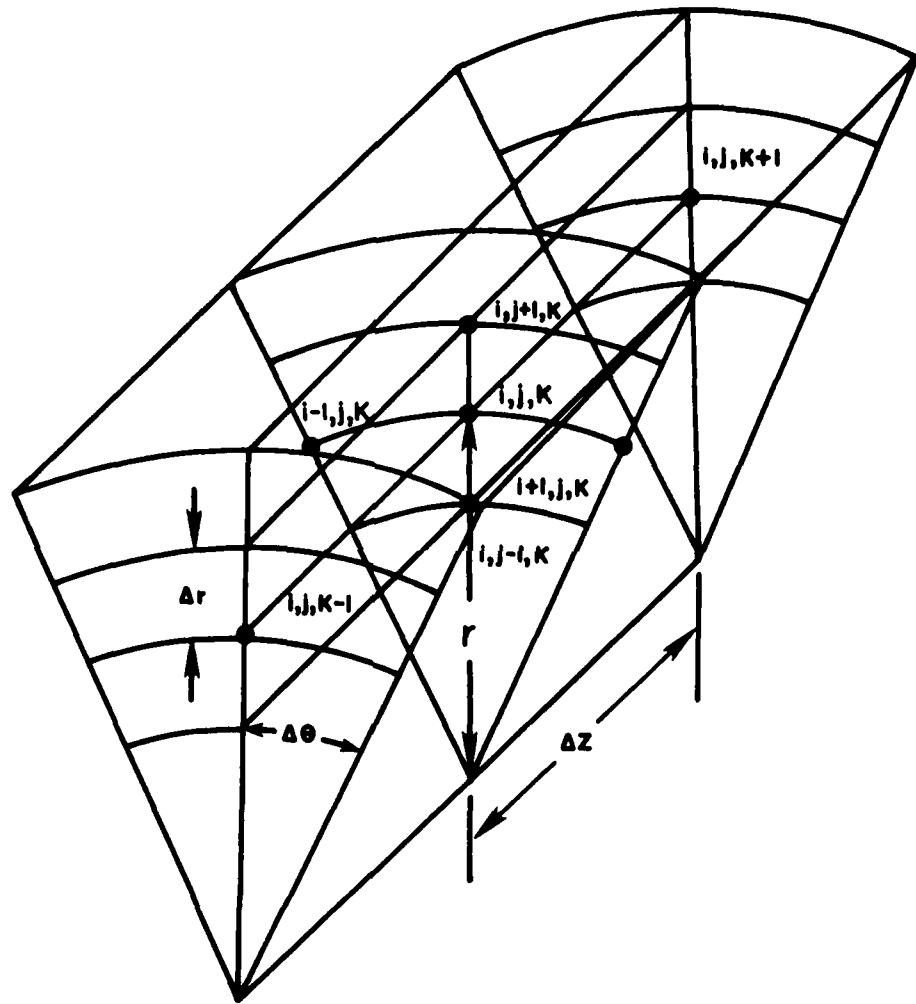


Figure 42. Interior Finite Difference Node

It is necessary to add Equations (C.2) through (C.7) in a way that will permit the attainment of a finite difference approximation to Equation (C.1). Therefore, Equations (C.2) through (C.7) were multiplied by the coefficients A,B,C,D,E, and F, respectively. The following constraints were applied to determine the coefficients:

$$\begin{aligned} \Sigma \text{ coefficients of } \frac{\partial T}{\partial \theta} &= 0 \\ \Sigma \text{ coefficients of } \frac{\partial^2 T}{\partial \theta^2} &= \frac{1}{r^2} \\ \Sigma \text{ coefficients of } \frac{\partial^2 T}{\partial r^2} &= 1 \\ \Sigma \text{ coefficients of } \frac{\partial T}{\partial r} &= \frac{1}{r} \\ \Sigma \text{ coefficients of } \frac{\partial T}{\partial z} &= 0 \\ \Sigma \text{ coefficients of } \frac{\partial^2 T}{\partial z^2} &= 1 \quad . \end{aligned} \tag{C.8}$$

The coefficients determined by application of those constraints are:

$$\begin{aligned} A &= C = 1/(r\Delta\theta)^2 \\ B &= \frac{2r + \Delta r}{2r\Delta r^2} \\ D &= \frac{2r - \Delta r}{2r\Delta r^2} \\ E &= F = 1/\Delta z^2 \quad . \end{aligned} \tag{C.9}$$

Multiplication of Equations (C.2) through (C.7) by the constants A through F, respectively, permits the attainment of the following approximation for Equation (C.1):

$$\begin{aligned} \nabla^2 T = & \frac{1}{(r\Delta\theta)^2} T_{i-1,j,k} + \frac{2r + \Delta r}{2r\Delta r^2} T_{i,j,k} + \frac{1}{(r\Delta\theta)^2} T_{i+1,j,k} \\ & + \frac{2r - \Delta r}{2r\Delta r^2} T_{i,j-1,k} + \frac{1}{\Delta z^2} T_{i,j,k+1} + \frac{1}{\Delta z^2} T_{i,j,k-1} \\ & - \left(\frac{2}{(r\Delta\theta)^2} + \frac{2r + \Delta r}{2r\Delta r^2} + \frac{2r - \Delta r}{2r\Delta r^2} + \frac{2}{\Delta z^2} \right) T_{i,j,k} \end{aligned} \quad (C.10)$$

For grid points on a boundary as shown in Figure 43, where heat generation and convection are present, Equation (C.1) was approximated by using the fictitious node $T_{i,j-1,k}$. The boundary condition on the surface was $-\frac{k\partial T}{\partial r} = \bar{h}(T_\infty - T_w) + \dot{q}_{gen}''$. (C.11)

The derivative on the left hand side of Equation (C.11) was approximated using a central difference scheme. Therefore,

$$\frac{T_{i,j-1,k} - T_{i,j+1,k}}{2\Delta r} = \frac{\bar{h}}{k} (T_\infty - T_{i,j,k}) + \frac{\dot{q}_{gen}''}{k} \quad (C.12)$$

or

$$T_{i,j-1,k} = \frac{2\Delta r \bar{h}}{k} (T_\infty - T_{i,j,k}) + \dot{q}_{gen}'' \frac{2\Delta r}{k} + T_{i,j+1,k}$$

substitution of Equation (C.12) into Equation (C.10) gives

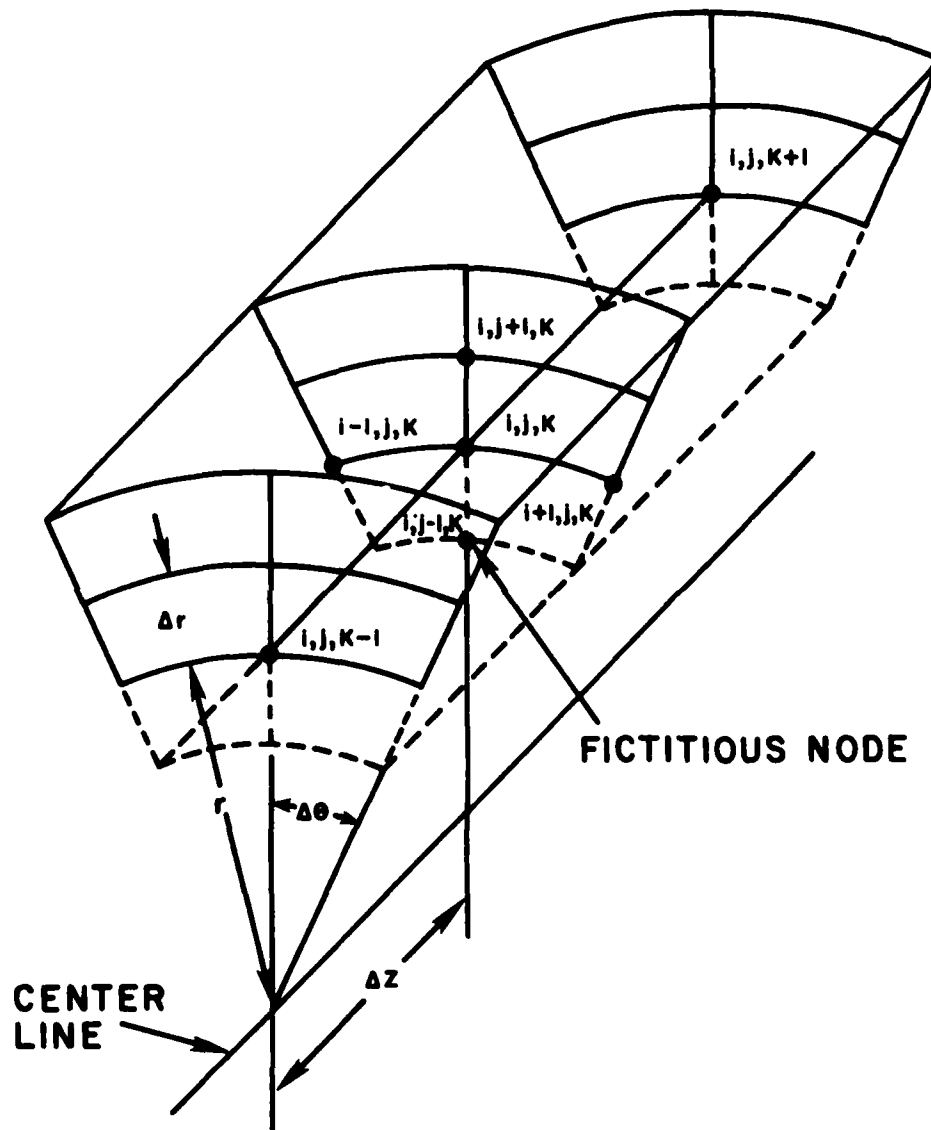


Figure 43. Boundary Finite Difference Node

$$\begin{aligned}
\nabla^2 T = & \frac{1}{(r\Delta\theta)^2} T_{i-1,j,k} + \frac{2r + \Delta r}{2r\Delta r^2} T_{i,j+1,k} + \frac{1}{(r\Delta\theta)^2} T_{i+1,j,k} \\
& + \frac{1}{\Delta z^2} T_{i,j,k-1} + \frac{1}{\Delta z^2} T_{i,j,k+1} + \frac{2r - \Delta r}{2r\Delta r^2} T_{i,j+1,k} \\
& + \left(\frac{2r - \Delta r}{2r\Delta r} \right) \frac{h}{k} T_\infty + \frac{2r - \Delta r}{2r\Delta r} \frac{\dot{q}_{gen}''}{k} \\
& - \left(\frac{2}{(r\Delta\theta)^2} + \frac{2r + \Delta r}{2r\Delta r^2} + \frac{2r - \Delta r}{2r\Delta r^2} + \frac{2}{\Delta z^2} + \left(\frac{2r - \Delta r}{r\Delta r} \right) \frac{\bar{h}}{k} \right) T_{i,j,k} \quad (C.13)
\end{aligned}$$

The fictitious node technique as described above was applied to all the boundaries.

In the steady state analysis, Equation (C.1) is equal to zero. Therefore, the temperature at each node can be determined by using Equations like (C.10) and (C.13). For example, using Equation (C.10) the expression for $T_{i,j,k}$ is

$$\begin{aligned}
T_{i,j,k} = & \left[\frac{1}{(r\Delta\theta)^2} T_{i-1,j,k} + \frac{2r + \Delta r}{2r\Delta r^2} T_{i,j+1,k} + \frac{1}{(r\Delta\theta)^2} T_{i+1,j,k} \right. \\
& \left. + \frac{2r - \Delta r}{2r\Delta r^2} T_{i,j-1,k} + \frac{1}{\Delta z^2} T_{i,j,k+1} + \frac{1}{\Delta z^2} T_{i,j,k-1} \right] \div \\
& \left(\frac{2}{(r\Delta\theta)^2} + \frac{2r + \Delta r}{2r\Delta r^2} + \frac{2r - \Delta r}{2r\Delta r^2} + \frac{2}{\Delta z^2} \right) \quad (C.14)
\end{aligned}$$

Solving for $T_{i,j,k}$ at each node, results in a set of algebraic expressions for $T_{i,j,k}$ which must be solved simultaneously. This was accomplished using the Gauss-Seidel iterative method with the incorporation of Young's over relaxation factor [7].

For the transient analysis, the equation

$$\nabla^2 T = \frac{1}{\alpha} \frac{\partial T}{\partial t} \quad (\text{C.15})$$

was approximated by finite differences. For the explicit solution, a finite difference expression for $\frac{\partial T}{\partial t}$ was obtained using a forward difference. Therefore, the approximation was

$$\frac{\partial T}{\partial t} = \frac{T_{i,j,k}^{N+1} - T_{i,j,k}^N}{\Delta t} \quad (\text{C.16})$$

The superscripts (N+1) and (N) refer to time $(t + \Delta t)$ and time (t) , respectively.

The finite difference approximation of Equation (C.15), for an interior node is:

$$\begin{aligned} \frac{T_{i,j,k}^{N+1} - T_{i,j,k}^N}{\alpha \Delta t} &= \frac{1}{(r\Delta\theta)^2} T_{i-1,j,k}^N + \frac{2r + \Delta r}{2r\Delta r^2} T_{i,j,k+1}^N \\ &\quad + \frac{1}{(r\Delta\theta)^2} T_{i+1,j,k}^N \\ &\quad + \frac{2r - \Delta r}{2r\Delta r^2} T_{i,j-1,k}^N + \frac{1}{\Delta z^2} T_{i,j,k+1}^N + \frac{1}{\Delta z^2} T_{i,j,k-1}^N \\ &\quad - \left[\frac{2}{(r\Delta\theta)^2} + \frac{2r + \Delta r}{2r\Delta r^2} + \frac{2r - \Delta r}{2r\Delta r^2} + \frac{2}{\Delta z^2} \right] T_{i,j,k}^N \quad (\text{C.17}) \end{aligned}$$

The approximations to Equation (C.15) for each node can be solved for $T_{i,j,k}^{N+1}$. Since the values of $T_{i,j,k}^N$ are all known, iteration is not required to solve the set of algebraic equations.

APPENDIX D

DERIVATION OF FRICTIONAL HEAT FLUX EQUATIONS

The total rate of frictional heat generated at the interface of two semi-infinite solids in sliding contact is

$$\dot{q}_{\text{TOTAL}}'' = \dot{q}_1'' + \dot{q}_2'' \quad , \quad (\text{D.1})$$

where \dot{q}_1'' and \dot{q}_2'' are the heat transferred into body I and II, respectively.

The heat conduction equation for each body is

$$\frac{\partial^2 T}{\partial z^2} = \frac{1}{\alpha} \frac{\partial T}{\partial t} \quad . \quad (\text{D.2})$$

The boundary conditions for each body are:

BODY I

$$z = 0 \quad - k_1 \frac{\partial T_1}{\partial z} = \dot{q}_1''$$

$$z = \infty \quad T_1 \neq \infty \quad (\text{D.3})$$

where $T_1 = t_1' - t_i'$.

BODY II

$$\begin{aligned} z = 0 & \quad k_2 \frac{\partial T}{\partial z} = \dot{q}_2'' \\ z = -\infty & \quad T_2 \neq \infty . \end{aligned} \quad (D.4)$$

The initial condition for each body is at

$$t = 0 \quad T = 0 . \quad (D.5)$$

Taking the Laplace transform of Equation (D.2) gives

$$\frac{\partial^2 \bar{T}}{\partial z^2} - \frac{s}{\alpha} \bar{T}(x,s) = 0 . \quad (D.6)$$

The boundary condition at $z = 0$ for solid I becomes

$$\frac{\partial \bar{T}}{\partial z}(0,s) = \frac{-\dot{q}_1''}{k_1 s} \quad (D.7)$$

when \dot{q}_1'' is assumed to be constant. The boundary condition at $z = \infty$ becomes

$$\bar{T}(\infty,s) \neq \infty . \quad (D.8)$$

The general solution to Equation (D.6) is

$$\bar{T}(x,s) = C_1 e^{\sqrt{s/\alpha} z} + C_2 e^{-\sqrt{s/\alpha} z} . \quad (D.9)$$

Applying boundary conditions (D.7) and (D.8) gives

$$\bar{T}(z,s) = \sqrt{\frac{\dot{q}_1''}{\left(\frac{1}{k_1}\right)^2 \alpha_1}} s^{-3/2} e^{-\sqrt{z^2/\alpha_1} \sqrt{s}} \quad (D.10)$$

From Reference 17 the inverse transform of Equation (D.10) is

$$T(z,\theta) = \sqrt{\frac{\dot{q}_1''}{\left(\frac{1}{k_1}\right)^2 \alpha_1}} \left[2\sqrt{\frac{t}{\pi}} e^{-(z^2/\alpha_1)/4t} - \left(\frac{z}{\alpha_1}\right) \operatorname{erfc} \frac{\sqrt{z^2/\alpha_1}}{2\sqrt{t}} \right] \quad (D.11)$$

Similarly for body II

$$T(z,\theta) = \sqrt{\frac{\dot{q}_2''}{\left(\frac{1}{k_2}\right)^2 \alpha_2}} \left[2\sqrt{\frac{t}{\pi}} e^{-(z^2/\alpha_1)/4t} - \left(\frac{z}{\alpha_2}\right) \operatorname{erfc} \frac{\sqrt{z^2/\alpha_2}}{2\sqrt{t}} \right] \quad (D.12)$$

Assuming no contact resistance

$$T_1(0,t) = T_2(0,t) \quad (D.13)$$

Therefore, by equating Equations (D.11) and (D.12), it is found that

$$\dot{q}_1'' = \dot{q}_2'' \frac{k_1}{k_2} \sqrt{\frac{\alpha_2}{\alpha_1}} \quad (D.14)$$

Combining Equations (D.1) and (D.14) gives

$$\dot{q}_2'' = \frac{\dot{q}_{\text{TOTAL}}''}{1 + \frac{k_1}{k_2} \sqrt{\frac{\alpha_2}{\alpha_1}}} \quad (D.15)$$

and

$$\dot{q}_1'' = \left[\frac{\dot{q}_{\text{TOTAL}}''}{1 + \frac{k_1}{k_2} \sqrt{\frac{\alpha_2}{\alpha_1}}} \right] \frac{k_1}{k_2} \sqrt{\frac{\alpha_2}{\alpha_1}} \quad (D.16)$$

DISTRIBUTION

**Commander (NSEA 09G32)
Naval Sea Systems Command
Department of the Navy
Washington, D. C. 20362**

Copies 1 and 2

**Commander (NSEA 0342)
Naval Sea Systems Command
Department of the Navy
Washington, D. C. 20362**

Copies 3 and 4

**Defense Documentation Center
5010 Duke Street
Cameron Station
Alexandria, VA 22314**

Copies 5 through 16